3D Numerical Modelling of Secondary Current in Shallow River Bends and Confluences

By

Rawaa Shaheed

A thesis submitted under supervisions of
Dr. Majid Mohammadian
in partial fulfilment of the requirements for the degree of

Masters of Applied Science in Civil Engineering

Department of Civil Engineering
University of Ottawa
Ottawa, Canada
May 2016

The M.A.Sc. in Civil Engineering is a joint program
with Carleton University administrated
by Ottawa-Carleton Institute for Civil Engineering

((وما توفيقي الا بالله عليه توكلت واليه انيب))

" and my success can only come from Allah. In Him I trust, and unto Him I return. " [Hud:88]

To…

The spirit of my parents …

My Lovely Husband…

Brother, Sisters…and all My Family…

With my Love…

Abstract

Secondary currents are one of the important features that characterize flow in river bends and confluences. Fluid particles follow a helical path instead of moving nearly parallel to the axis of the channel. The local imbalance between the vertically varying centrifugal force and the cross-stream pressure gradient results in generating the secondary flow and raising a typical motion of the helical flow. A number of studies, including experimental or mathematical, have been conducted to examine flow characteristics in curved open channels, river meanders, or confluences. In this research, the influence of secondary currents is studied on the elevation of water surface and the hydraulic structures in channel bends and confluences by employing a 3D OpenFOAM numerical model.

The research implements the 3D OpenFOAM numerical model to simulate the horizontal distribution of the flow in curved rivers. In addition, the progress in unraveling and understanding the bend dynamics is considered. The finite volume method in (OpenFOAM) software is used to simulate and examine the behavior of secondary current in channel bends and confluences. Thereafter, a comparison between the experimental data and a numerical model is conducted. Two sets of experimental data are used; the data provided by Rozovskii (1961) for sharply curved channel, and the dataset provided by Shumate (1998) for confluent channel.

Two solvers in (OpenFOAM) software were selected to solve the problem regarding the experiment; InterFoam and PisoFoam. The InterFoam is a transient solver for incompressible flow that is used with open channel flow and Free Surface Model. The PisoFoam is a transient solver for incompressible flow that is used with closed channel flow and Rigid-Lid Model. Various turbulence models (i.e. Standard k-ε, Realizable k-ε, LRR, and LES) are applied in the numerical model to assess the accuracy of turbulence models in predicting the behaviour of the flow in channel bends and confluences. The accuracies of various turbulence models are examined and discussed.

Acknowledgements

I would like to extend my sincere thanks and gratitude to my supervisor Dr. Majid Mohammadian for his continuous support and generosity during the duration of the research.

I would also like to thank Mr. Hossein Kheirkhah Gildeh for his guidance and help with the OpenFOAM during the research.

My thanks and appreciation to the General Commission for Irrigation and Reclamation Projects, one of the formations of the Ministry of Water Resources in Iraq for their support and assistance.

Finally, I would like to thank my lovely husband, family, and friends for their love and encouragement.

Table of Contents

List of Figures

List of Tables

List of Symbols and Acronyms

B	Channel width (m)
g	Acceleration of gravity (m/s^2)
h	Flow depth (m)
H	Bottom elevation (m)
n	Manning's roughness coefficient
P	Pressure (N/m^2)
Q	Flow discharge (m^3/s)
Q_m	Main channel discharge (m^3/s)
Q_b	Branch channel discharge (m^3/s)
q_1	Flow discharge per unit width in the x direction (m^3/s)
q_2	Flow discharge per unit width in the y directions (m^3/s)
r	Radius of curvature for the outer bank (m)
ri	Radius of curvature for the inner bank (m)
t	Time (sec)
U	Depth averaged velocity magnitude (m/s)
U	Mean flow velocity (m/s)
U_i	Depth averaged velocity in *i*-direction (m/s)
$\hat{u}_1$	Velocities at the water surface in excess of mean velocity in the x-direction (m/s)
$\hat{u}_2$	Velocities at the water surface in excess of mean velocity in the y-direction (m/s)
$u_i(z)$	Vertical distribution of *i*-component velocity (m/s)
$\overline{u_i u_j}$	Reynolds stress tensor

$u,\ v, w$	Velocity in the *x*, *y*, *z* direction, respectively (m/s)
x, *y*, *z*	Coordinates
μ	viscosity (N.s/m^2)
v	Kinematic eddy viscosity (m^2/s)
ρ	Water density (kg/m^3)
ρ	Mass density (kg/m^3)
ρ_w	Density of water (kg/m^3)
ρ_a	Density of the air (kg/m^3)
τ_{ij}	Vertically averaged total turbulent shear stress in the ij-direction (N/m^2)
τ_{bi}	Bed shear stress (N/m^2)
z_m	Mean flow depth (m)

Acronyms

RAS	Reynolds-Averaged Simulation
LES	Large Eddy Simulation
ADV	Acoustic Doppler Velocimeter
CFD	Computational Fluid Dynamics
RANS	Reynolds-Averaged Navier-Stokes
ADCP	Acoustic Doppler Current Profile
DAM	Depth-Averaged Method
FSM	Free Surface Model
RLM	Rigid-Lid Model
FVM	Finite Volume Method
FDM	Finite Difference Method
FEM	Finite Element Method

VOF	Volume Of Fluid
ASM	Algebraic Stress Models
RSM	Reynolds Stress Models

CHAPTER ONE

INTRODUCTION

1.1. Background

The geometry of rivers has a great impact on river engineering problems. The influence of river bend and topography of curved rivers have a substantial role in the analysis of different aspects of these problems like navigability, the protection of bank, river regulation, and dispersion of heat and pollutants (Kalkwijk and De Vriend, 1980). The importance of investigating bends in rivers is raised from the fact that finding a straight stream with a length more than 10 channel width can be considered almost impossible as shown in Figure 1.1 (Ghamry and Steffler, 2005). There are many parameters that could be affected by channel curvature like secondary flow, super-elevation, redistribution of primary flow, bed scour in mobile boundaries, meanders migration, and bank erosion/shifting. Consequently, understanding and estimating these impacts in natural channels is essential for the design of river engineering works (Song et al., 2012).

Figure 1.1: Wabash river, an example of river bends from www.riverlorian.com.

The flow pattern in such channels is considered fairly complex because fluid particles follow helical paths instead of moving parallel to the axis of the channel. Thus, it could be considered that the helical flow is a combination of two flows, the main flow which is approximately parallel to the channel axis and the secondary circulation (Kalkwijk and DeVriend, 1980). The importance of studying the secondary or transverse flow comes from its partial influence on the large-scale bed topography of natural alluvial channel bends. The primary flow is affected by the transverse flow as well. In addition, it will be a good source for navigation and diffusion studies in natural channels (Blanckaert and De Vriend, 2004). In channel bends, secondary currents develop by skewing of cross-stream vorticity into a long stream direction. The skew that results due to the secondary circulation carries the surface water quickly in the outer bank direction and the bed water slowly towards the inner bank (Thorne et al., 1985). Rozovskii (1961) and De Vriend (1980) measurements have proved that the secondary flow moves toward the external bank near the upper part of the river and towards the internal bank in the lower part of the river. As a result, the shear force which is in the same direction of the local flow near to the lower part of the river (the bottom) turns slightly from the direction of the mean flow (Duan, 2004).

The importance of the secondary flow or transverse flow lies in the followings (Falcon 1984):

- It partially has the responsibility about the bed topography large-scale in natural alluvial channel curves,
- The possibility of dynamically interacting with the primary flow, and
- It is beneficial for diffusion and navigation studies in natural waterways.

1.2. Shallow River Bends

This study deals with three-dimensional simulation of rivers with the following characteristics:

- Small depth comparing with width,
- Small width comparing with the radius of curvature,
- The scale of the horizontal length for the bottom variation is of the same order of the width magnitude,
- The friction of the flow is controlled,

- The velocity longitudinal component controls the other ones, and
- Small Froude Number.

1.3. The Mechanism of Secondary Flow

For the purpose of the present research, $\boldsymbol{u}$ is the component of secondary-flow velocity which happens in planes perpendicular to the main direction of the motion (i.e. to the channel axis), while $\boldsymbol{v}$ is the stream-wise velocity component and $\boldsymbol{r}$ is the radius of curvature. Thus, the centrifugal acceleration because of the channel bend (the system of the coordinate shown is cylindrical) is (v^2/r). As shown in Figure 1.2, $\boldsymbol{v}$ varies from zero at the channel bed to a maximum value at or close the surface of water. As a result, the centrifugal force $\boldsymbol{s}$ reaches its maximum value near the surface of water and then decreases toward the bed (Falcon, 1984).

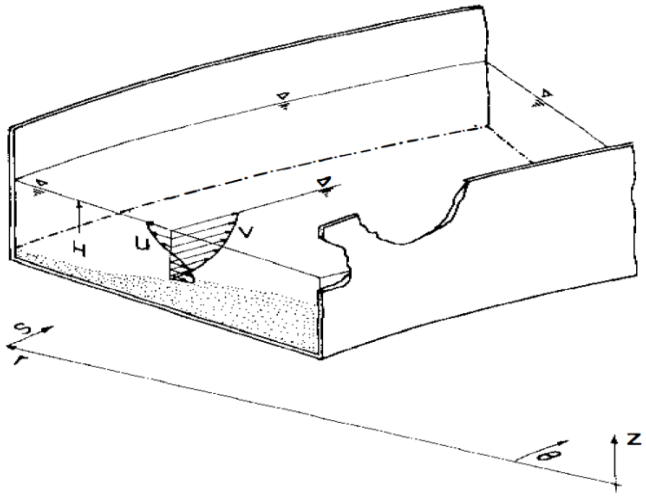

Figure 1.2: Illustrative sketch for curved channel flow (Falcon, 1984).

Several studies have shown that the secondary rotation in the plane normal to the direction of the mean flow is produced by the sheared and curved flows. The local imbalance between the centrifugal force that vary vertically and the cross-stream pressure gradient results in generating the secondary flow and producing the typical motion of helical flow (Figure 1.3). As a result of this imbalance situation, two flows exist; flow towards the inner bank of the curve in the lower part of the water column and an outer flow near the surface of water (Song et al., 2012).

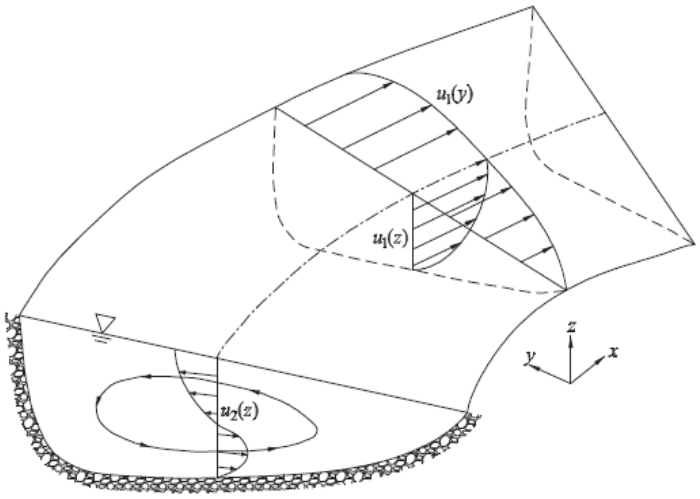

Figure 1.3: Definition sketch for curved channel flow (Song et al., 2012).

1.4. Flow in River Confluences

Confluence in rivers results from the junction of two separate channel flows producing a complex hydro- and morphodynamic environment. The main river tries to accommodate the water flow and sediment that coming from the tributary. This accommodation causes rapid changes in fluid motion, sediment transport, and channel morphology which occur at confluences of the rivers (Riley, 2013). As the tributary or the branch channel enters the main channel, a separation zone or recirculation zone is generated at the downstream of the confluence near the internal bank of the main channel. At the same time, there is a contracted flow region on the other side of the main channel near the external bank. The separation zone has a great impact on the features of the flow in the confluent rivers, which makes flow features being more complex and this is the reason behind the complexity of flow features (Thanh et al., 2010). The importance of confluent rivers lies on their effect on river engineering, sedimentology or geomorphology. The reasons behind this great importance are; the complexity of flow interactions, the irregularity in sediment load, and bed sediment size (Birjukova et al., 2014).

1.5. Secondary Flow in Confluent Channel

The flow direction changes as the flow of the tributary enters the main river. This change causes a surface radial flow to be induced by the centrifugal force, and opposite to the deflection and a bottom inward current. In contrast, the secondary current of the main channel flow rotates in the opposite direction of the secondary flow in the branch channel as illustrated in Figure 1.4. Due to the joining of the flows of the branch and main channels in this case, a shearing action to the main flow is set up by the tributary channel, and then two surface flows are evolved. The influences of comparative magnitudes of consolidated flows and the profile of the non-uniform vertical velocity are the reason behind the skewing of shear plane rather than vertical. The new merged flow has features of the three-dimensionality induced by the non-uniform vertical velocity profile. Subsequently, a clockwise rotating secondary vortex could be found at the downstream of the main channel close to the internal bank, and looking downstream (Barkdoll, 2003). At the other bank (external bank) of the main channel downstream, another secondary vortex appears and rotates against the secondary flow of the branch channel. At last, the secondary currents of the two channels fade gradually towards the direction of the river, and this takes place mainly because of the fluid viscosity.

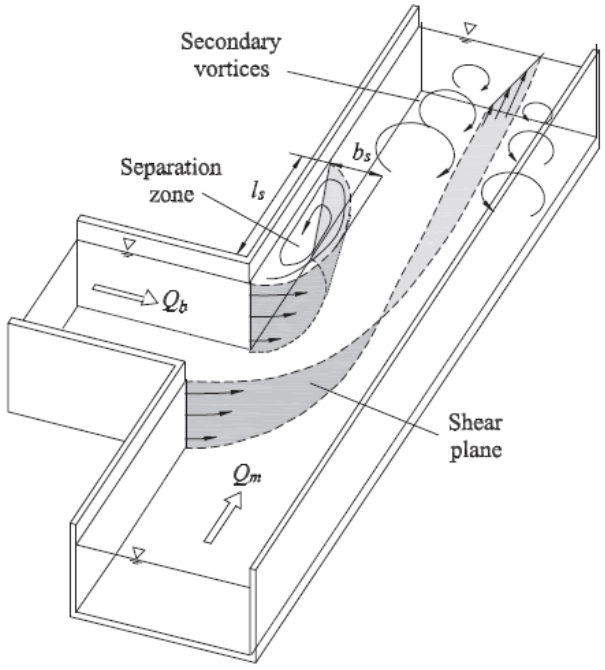

Figure 1.4 : The structure of secondary flow in confluent channel (Weber et al., 2001).

1.6. Research Objectives

Due to the necessity to get satisfying predictions in river curves, 3D numerical models might be considered useful for this purpose. These models depend on the three-dimensional flow features consolidated with the complex spiral flow motion in the river curve. Nevertheless, the large amount of computational time and possible numerical instability are important matters that most of the 3D models suffer from (Song et al., 2012). In this study, the effects of the secondary currents will be examined on the hydraulic structures and water surface elevation in curved channels and confluences by employing a 3D OpenFOAM numerical model (which will be explained later).

Thus, the present research aims at achieving the following objectives:

- Assess the numerical model performance in the simulation of highly curved channels and confluences.
- Choose the suitable numerical model to simulate the behaviour of the flow in the river bends and confluences.
- Achieve the required components of the model by analysing the governing equations in the mathematical model.
- Examine and compare a number of turbulence models within the numerical model and find the most accurate ones and optimal parameters.
- Solve the model equations after finding out the best steady numerical schemes.
- Compare the numerical results with comprehensive experimental and numerical data that have been obtained by other researchers, taking into account the focus on velocity and water depth.

1.7. Research Novelty

A number of studies including experimental or mathematical ones have been conducted to examine the flow characteristics in curved open channels, river meanders or confluences. However, understanding the dynamics of meanders is still incomplete, in particular with respect to how the variation in channel characteristics controls the flow dynamics.

The research will implement the 3D OpenFOAM numerical model to simulate the horizontal

distribution of flow in curved rivers. In addition, the progress in unravelling and understanding the bend dynamics will be considered. Furthermore, in this research several turbulence models have been studied and evaluated to determine the best numerical models that could predict the secondary current properties in the river bends and confluences with higher level of accuracy.

1.8. Structure of the Thesis

This research includes five chapters as detailed in below:

Chapter 1 presents the Introduction.

Chapter 2 deals with the literature review. This chapter focuses on the concept of the secondary flows in river bends and confluences and the main factors that affect the secondary flow through reviewing the previous studies that have been conducted in this field. Also, this chapter takes into account the experimental and numerical studies on this topic. Furthermore, the chapter is devoted to review different turbulence models that have been developed to simulate secondary flows such as (i) Standard k-ε; (ii) Realizable k-ε; (iii) Launder-Reece-Rodi RSTM (iv) k -equation large eddy simulation approach.

Chapter 3 presents the mathematical and numerical model. This chapter focuses on the mathematical and numerical modelling and the theoretical concepts for these studies. The chapter is devoted to improve the model by using OpenFOAM toolbox and illustrates the methodology used to achieve this goal.

Chapter 4 deals with results and discussions. The summary of the main results is illustrated in this chapter and a discussion for the main outcomes of the research is provided.

Chapter 5 presents the conclusion and suggestions for future research. This chapter includes the conclusions of the research and proposes recommendations for subsequent studies.

CHAPTER TWO

LITERATURE REVIEW

2.1. Introduction

Rivers are considered as one of the most important water resources that exist on the surface of the earth. In addition to their role in providing a place of living for human beings through the ages, they are the best places for rejoicing, agriculture and livestock development. During the time, changes and variations play a big role in affecting the rivers. For instance, erosion in walls and beds and scour at other parts are examples of such changes that could be undesirable for people, especially for those settling at riverbanks (see e.g. Figure 2.1), and may cause irreparable damages to people and facilities in general. Therefore, and due to the importance of this issue, it is necessary to take some critical measures and required actions to control and direct rivers in order to minimize the above mentioned damages, and thus to make the best use of rivers as an indispensable natural resource. In order to achieve this goal, the first step has been taken towards investigating flow patterns and measuring three-dimensional velocities in river routes (Vaghefi et al., 2015).

Figure 2.1: Charley river at Yukon, Alaska. (Wim, 2010).

2.2. River Bends

Meandering is considered one of the common cases in most rivers. Rivers tend to change their morphology in order to keep equilibrium with the ever-changing conditions imposed on the stream (Cameron and Bauer, 2014). The meandering of curved rivers is defined as "the ratio between the length of the river measured along its thalweg (line of maximum depth) or along its centreline, and the valley length between the upstream and downstream sections" (Rust, 1978), as shown in Figure 2.2.

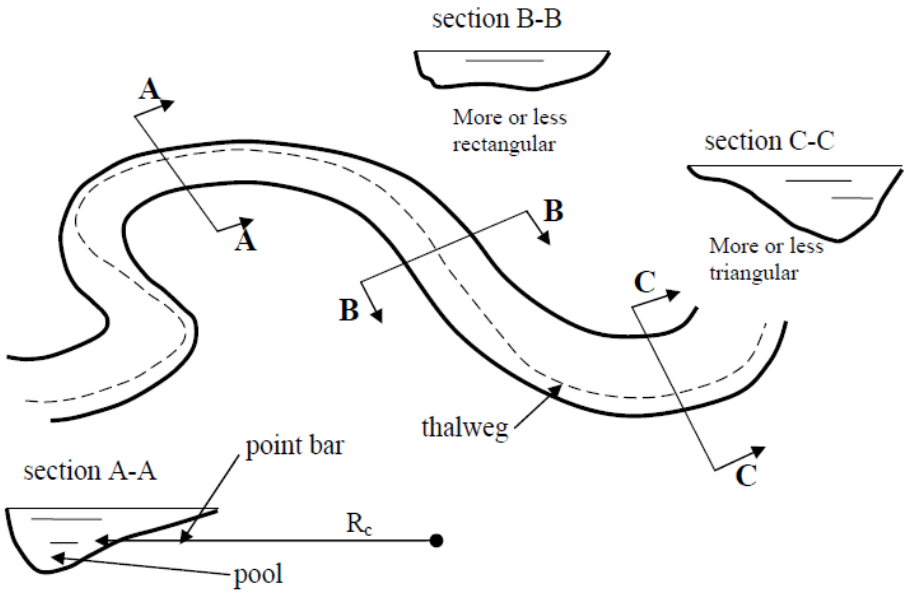

Figure 2.2: Typical meandering river cross-sections (Alessandra, 2008).

Also meandering ratio or sinuosity index is "a means of quantifying how much a river or stream meanders (how much its course deviates from the shortest possible path)" (Nayak, 2010). It is calculated as the stream length divided by the valley length. The river is considered "straight" when the sinuosity ratio is less than 1.05 and is considered "meandering" when having sinuosity ratio greater than 1.05. Shallowness and deepness of meandering channel could be identified through the ratio of the average channel width (b) to its depth (h). In shallow channels, the ratio of (b/h) is greater than 5 (Rozovskii, 1961). Otherwise, it is considered deep channel (Nayak, 2010).

Bank erosion and accretion are the main phenomena of meandering in rivers. The main reason behind these phenomena is variation in velocity of water in river bends. Also, the distribution of shear stress on the cross sectional and longitudinal profiles of the river is affected by this velocity pattern (Cameron and Bauer, 2014) as shown in Figure 2.3. Accordingly, rivers transfer their location and develop over time in order to accommodate the uneven distribution of shear stress and the pattern of erosion and sedimentation in the meandering of rivers (Cameron and Bauer, 2014).

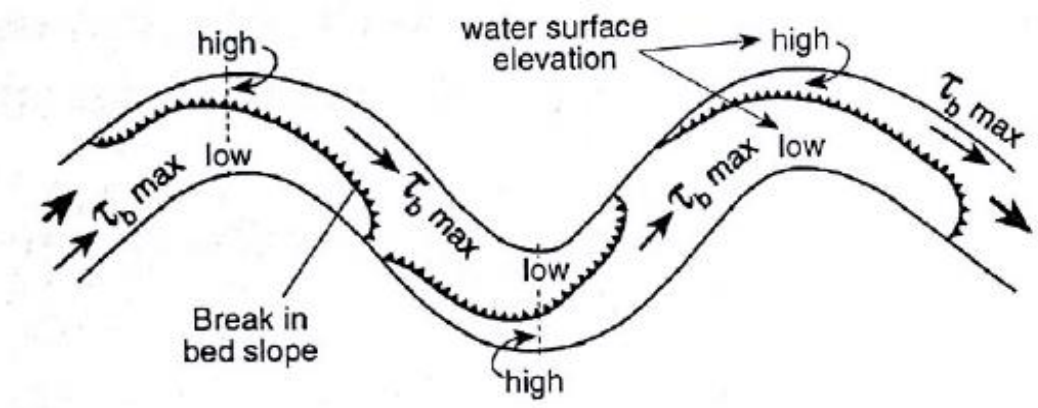

Figure 2.3: The distribution of shear stress along a meandering river (Knighton, 1998).

Generally, river bends could be considered one of the most complex geometries that characterize the rivers, in addition to the other characteristics like the expansions and contractions of the channel, changeable bed and the bank roughness. These features might be the base reason behind creating the distribution of the unbalanced turbulent stress along the cross-sectional plane that causing the secondary flows formation. The most important factor that has the main role in morphological changes of river meander is the ratio of curvature radius to river width, which is commonly known as relative curvature (Esfahani and Keshavarzi, 2010). Based on the relative curvature of the bends, bends could be characterised as sharp, moderate or mild curvature. Sharp curvature is the one with relative curvature values smaller than 3, while the relative curvature for moderate or mild curvature is larger than 3 as shown in Figure 2.4 and Figure 2.5, respectively (Leschziner and Rodi, 1979).

Figure 2.4: The sharp meandering river (Dey, 2014).

According to previous studies, there is a difference in the hydrodynamic between each of them (e.g. Hickin, 1978).

Figure 2.5: The moderate meandering river (Dey, 2014).

Many experimental and theoretical works have been done by geomorphologists over the years to understand the dynamics of river bends. In 1988, some experiments have been conducted by Odgaard and Bergs using mild curve ($Rc/B = 5.4$) with 180-degree bend. They proved

that changing in the curvature of the river bend affects the components of the velocity, bed topography and the structure of the flow (Odgaard and Bergs, 1988). In 1990, Ikeda et al. developed a three-dimensional mathematical model to simulate fully developed flow in mildly curved open channels (Ikeda et al., 1990). A laboratory experiments were performed by Jung and Yoon in 2000. They conducted the experiments in a mild 180-degree curved bend using different bed materials. They concluded that extreme streamwise velocity in the upper part of the curve is skewed inwards, and the bed materials effect does not change it (Esfahani and Keshavarzi, 2010). The downstream velocity vertical profiles and secondary current were presented through a model developed by Blankaert in 2001. The model is affected by several factors such as Froude number, curvature ratio, normalized transversal velocity gradient, and Chezzy coefficient. Consequently, good agreement was reached between the model and experimental data of a strongly curved flow (Blanckaert, 2001). Also in 2001, some experiments have been conducted in a sharp curved open channel by Blankaert and Graf. They concluded that Rozovskii model overpredicts the strength of secondary circulation and velocity distribution for this kind of bend (Blanckaert and Graf, 2001).

In 2003, Giri et al. used three sequential bends in a mild meandering flume for the experiments. The bends were with and without the training structures of river in order to examinethe impact of these structures on the pattern of the flow. For the case without river training structures, they found that water flow is approximately uniform along the center of the river and there is a graduate acceleration or deceleration near the two banks. In the other case of bends with river training structures, they found that in the external bank of second bend, there is dead area generated all over the bank. This situation might occur because of existence of training structures inside the previous bend (Giri et al., 2003).

Turbulent structures in strongly open channel bends have been investigated by Blankaert and De Vriend in 2004 and 2005 (Blankaert and De Vriend, 2004; Blankaert and De Vriend, 2005). Three physical models of multi-bend meandering rivers were designed by Esfahani in 2009, and Esfahani and Keshavarzi in 2009 as well, to examine the structure of the flow inside the inner part of mild and strongly curved bend and outside meandering rivers (Esfahani, 2009; Esfahani and Keshavarzi, 2009). Also in 2009, a new equation for super elevation in sharp curved open channels is presented by Akhtari et al. (2009).

Consequently, in order to predict the distribution of bed shear stress in the bends of rivers and open channels, it is essential to study the influence of secondary flow and the distribution of velocity on flow pattern. Therefore, a lot of studies have been carried out on the structures of secondary flow and the distribution of shear stress at bend routes.

2.3. Secondary Flow in River Bends

The characteristics of flow could be considered more complicated in channel bends than those in straight ones (Lien et al., 1999). The particles of the fluid follow a spiral path instead of moving more or less parallel to the axis of the channel (Kalkwijk and De Vriend, 1980). In addition to the turbulence and the 3D nature of flow, several factors could be the reason behind this complexity such as bed topography and depth variations, which are generally under the influence of erosion, sediment transport, and sedimentation processes. In river bends, the centrifugal force affects the flow once it enters the bend. Based on the radius of the bend and the depth direction due to the velocity variation, this force could be different. As a result to the centrifugal force in river bends, the lateral gradient on water surface leads to the lateral pressure gradient at cross section. One of the most dominant features of the flow in curved open channels is secondary currents (Blanckaert and De Vriend, 2004). Secondary currents are defined as "currents that occur in a plane normal to the axis of primary flow" (Thorne et al., 1985). The imbalance between the gradient force of the transverse water surface and centrifugal force over the depth occurs due to the vertical variation of the primary flow velocity which causes the secondary flow as shown in Figure 2.6 (Lien et al., 1999).

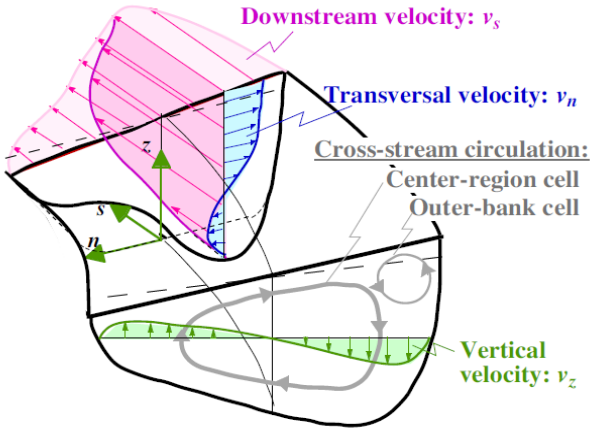

Figure 2.6: Definition sketch of flow in an open-channel bend (Graf and Blanckaert, 2002).

The secondary flow moves in a helical path towards the outer wall near the water surface and towards the inner wall near the bed. Normally in a straight river, the core of high velocity flow is located near the centre of the river. In the river bend and as the flow enters the bend, a decreasing in the water depth near the inner bank occurs due to the transverse inclination of the free water surface. Decreasing the flow depth in the inner bank of the river is associated with the increasing of the flow velocity at the same side. However, near the downstream of the river, the velocity structure will change because of the centrifugal force and the exchange of momentum between horizontal layers due to transverse circulation which result in transferring the higher velocity near the outer bank. Probably, the high velocity stays adjacent to the outer bank for a long distance in the downstream direction unless meanders occur again in the river causing another change in the velocity structure. Until now, extensive researches have been undertaken for better understanding of the flow in river curves and the scour pattern in meanders (Vaghefi et al., 2015).

2.4. Experimental and Numerical Studies

The existence of spiral flow pattern in channel bends was reported first by Thomson in 1876. The reason behind this spiral flow is the interactions between the secondary current and absence of regulation in velocity profile along the channel (Thomson, 1876). In 1943, an experiments include two 180-degree bends have been carried out by Mockmore. He measured longitudinal velocity profiles, and finally he reported that the flow close to the interior wall is more than that near the exterior wall. Furthermore, he found the flow pattern in the channel bends. He also proved that the distribution of velocity in the cross section would be in a way that the multiplication of tangential velocity and radius of curvature would result in a constant value (Mockmore, 1944). Flow in river bends has been studied by Shukry in 1949. He introduced a criterion for the secondary flow strength. The criterion includes the kinetic energy ratio of lateral flow to that of the main flow. Also, he concluded that in the curve of the river, the kinetic energy of the longitudinal orientation is larger than that of the lateral flow (Shukry, 1950). The relation that determined the specific length for when the secondary flow has the maximum strength was offered by Rozovskii in 1961. Accordingly, he concluded that for developing secondary flow, it should be a bend with a central angle of at least 100-degrees for shallow channels, and a central angle of 180-degrees for deep ones. Also he observed that

the favourable results for velocity profile could be obtained from the logarithmic distribution probability (Rozovskii, 1961). Shear stress and velocity distribution have been studied by Ippen and Drinker in 1962. A trapezoidal meandering bend with varying entrance conditions has been used in that study. They injected dye into the water and traced their paths. Thereafter, they observed that the dye chain would direct towards the inner bank in the bed of the channel, and towards the outer bank near the water surface. This phenomenon has been referred to as the effect of wall friction on flow field. Moreover, the relationship between radius of curvature and maximum shear stress has been determined as well (Ippen and Drinker, 1962).

The numerical simulation for turbulent flow in 180-degree sharp curve has been used by Leschziner and Rodi in 1979 using k-ε model. They supposed absence of hydraulic jump and flow separation. They observed that the higher velocity tends to be closer to the outer bank of the channel near the end of the bend (Leschziner and Rodi, 1979). Also in 1979, the effect of secondary flow on the distribution of bed shear stress was investigated by Nouh and Townsend. According to their results, the effect of the generated secondary flow remains after the bend exit and continues towards the downstream bend (Nouh and Townsend, 1979).

A field investigation was conducted by De Vriend and Geldof in 1983. The study that has been conducted in Dommel which is a river in Netherlands, included a numerical simulation of flow within a short period of time. The section included two sequential curves. Both of them were in 90-degree and in the same direction with a short straight connection between them. The results revealed that at the beginning of the bend, the maximum velocity is found near the inner bank of the river, while maximum velocity at the end of the bend tends to be oriented to the outer bank of the river (De Vriend and Geldof, 1983). A mathematical model was presented by Odgaard in 1986 to simulate bed changes in sinusoidal alluvial rivers. According to this model, there is a big interaction from the secondary flow component and the transverse bed slope towards the curvature changes. Therefore, a model was developed to provide an accurate prediction of flow and bed features in meandering alluvial channels (Odgaard, 1986). Bergs studied in 1990 the flow pattern and topographical changes in the bed of the channel by conducting an experimental study on a U-shaped flume with trapezoidal section and live bed. He concluded that the flow takes a spiral form when entering the bend and then it expands within a distance of 3 to 5 meters from the bend. Soon after, it completely

disappears at the end of the bend (Bergs, 1990).

In 1998, a 3D hydrodynamic model was developed for flow in bends by Jian and McCorquadale. This hydrodynamic model had the capability to model the changes for the free surface and bed topography (Jian and McCorquadale, 1998). The flow pattern was investigated by Lien et al. in 1999 through 90 and 180 degree-bends and using depth averaged two-dimensional model. The influence of the secondary flow was determined in the model using the calculation of distributed tensor of the stress. In addition to the spread stresses, a comparison between the important forces that exist in the flume was conducted. The results showed a difference between the secondary flows in 180-degree bend and 90-degree bend. The former is stronger than the latter (Lien et al., 1999). In 180-degree mild bend, the flow pattern and bed topography were studied by Jung and Yoon in 2000. Generally, they observed that in mild curves and with any kind of bed material, the higher velocity directed towards the interior bank at the first half of the entrance zone of the curve. However, while the higher velocity moving towards the end of the bend, its location will transmit gradually towards the exterior bank (Vaghefi et al., 2015). Also in 2000, a 3D flow pattern in open channels was studied by Wu et al. They considered sediment as bed and suspended loads in a curve with 180-degree. Secondary flow was predicted well by this model. The twist angle of velocity vector was specified as well, which was averaged. Their conclusion included that higher velocity tends to be near the outer bank while lower ones direct towards the inner bank. Consequently, the water depth is lesser near the inner bank than near the outer bank (Wu et al., 2000).

In 2002, an experimental and numerical analysis in meandering rivers was conducted by Shams et al. They concluded that there is resemblance in the results between the measured mean parameters of the flow and the numerical model. However, the turbulence parameters generated by the measurements are varying from those results (Shams et al., 2002). Using the Large Eddy Simulation Method (LES), the flow pattern in a mildly curved river bend was modelled by Booij in 2003. A comparison was made between the Reynolds stresses in the channel and the results of LES. The stresses could be used for studying the longitudinal momentum displacement. Also, it can be used to examine the impact of transporting the secondary flow momentum on longitudinal momentum (Booij, 2003a). The velocity

distribution in flume bends was studied by Blanckaert and Graf in 2004 in addition to the boundary shear stress, and features and form of bed topography in the bends. A semi 3D model was used and a central zone was considered as a cell, which can twist to determine bed topography in flume bends (Blanckaert and Graf, 2004).

Secondary flow, velocity distribution pattern, and boundary shear stress in open channels were examined by Yang in 2005. In this study, velocity distribution and shear stress were applied to laminar, steady, and turbulent flows. Also, the equations that govern the boundary shear stress and Reynolds stress distribution were stated (Yang, 2005). An experimental study on a local scour in 90-degree curved flume was carried out by Sui et al. in 2006. In this study, the influence of some parameters such as Froude number, the width and the slope of the protective wall, and the size of bed particle on the amount of scour near the bed was analysed (Sui et al., 2006). Experimental and numerical studies for flow pattern in the curve of 90-degree were done by Naji et al. in 2010. Their conclusion included that streamlines orient towards the inner wall of the channel in the level close to bed, while the orient towards the outer wall of the channel in the level close to the water surface (Naji Abhari et al., 2010). Also in 2010, Barbhuiya and Talukdar conducted an experimental study for flow of 3D pattern and scour in a bend of 90-degree. In this study, some elements were measured like velocity-time components, turbulent tension, and Reynolds shear stress in different vertical sections using Acoustic Doppler Velocimeter (ADV). According to the results, they indicated that the maximum measured velocity was 1.61 times the mean velocity. The maximum scour hole depth was found (Barbhuiya and Talukdar, 2010).

Two Computational Fluid Dynamics (CFD) codes (RANS and LES) were used by Stoesser et al. in 2010 to compute flow in meandering channel. Different turbulence closure approaches were employed to solve the Navier-Stokes equations. According to the comparison conducted in this study between the results that obtained from the two codes and the experimental data from the physical model, they indicated that the primary helical flow pattern in meander was predicted by both of the LES and RANS simulations, in addition to the happening of an outer-bank secondary cell (Stoesser et al., 2010). An experimental study for 3D flow pattern and erosion was conducted by Uddin and Rahman in 2012 using Acoustic Doppler Current Profile (ADCP) velocity meter in Jamuna river bend. The 3D velocity of the flow and shear stress

were measured in this study in the place close to the bed of the river. A model was presented to predict the erosion on the bend based on the flow processes. Finally, a comparison between the model and the real data recorded from the observations of the mentioned river was done (Uddin and Rahman, 2012). In 2014, a numerical study was carried out by Liaghat et al. for the hydraulic of flow in a U-shaped channel with changing width using SSIIM software. The study addressed the 3D flow velocity components, shear stress, and the strength of secondary and spiral flow (Liaghat et al., 2014). Also in 2014, Depth-Averaged Method (DAM) was used by Vaghefi et al. in 180-degree sharp bend to study and analyse the distribution of shear stress near the channel's bed. The results indicated that the maximum shear stress occurs at the beginning of the bend in the 40-degree cross section close to the interior wall of the channel (Vaghefi et al., 2014).

2.5. The Strength of Secondary Flow

Many factors could influence the strength of secondary flow, the distribution of velocity, and bed shear stress distribution in river bends such as: radius/channel width ratio (R/B), channel width/flow depth ratio (B/H), and (H/R), which equal to[$(H/B) \times (B/R)$]. According to that, many studies were performed to examine these factors and determine the most influential one. The main parameter according to (Rozovskii, 1961; Engelund, 1974) that affects the circulation level which associated with the secondary flow in the bend is H/R.The decrease of R/B causes an increase in the circulation induced by the secondary flow, which comply with the results reported by Hickin based on field studies in 1978 (Hickin, 1978). According to Hickin and Nanson (1984), a decrease of R/B causes an increasein the rate of bend migration. However, at $R/B \approx 2$, a decrease in the bend migration rate starts after this point (Hickin and Nanson, 1984). The influences of R/B and $C_f^{-1}H/B$ (where C_f is the bed friction coefficient) on bend flow was studied by Blanckaert (2011) and Ottevanger et al. (2011). They used nonlinear one-dimensional (1D) analytical models in their study. Consequently, the performance of the models that used were comparatively good for both of the moderate and sharp bends (Blanckaert, 2011; Ottevanger et al., 2011). The flow in river bends and curved channels were studied using different types of numerical models. The main purpose of these models was to clarify the details of flow in bends and meandering channels (Zeng et al., 2008).

2.6. Hydrodynamic Modelling of Bend Flow

Basically, there are two categories of hydrodynamic models for flow in river bends: linear models, and nonlinear models. These models are mainly used to combine the impact of the secondary current in bends. Linear and nonlinear aspects of flow development and bed perturbations in evolving bends were studied by Seminara and Tubino in 1989. In this study, a methodical therapy for such cases was provided (Seminara and Tubino, 1989). A general mathematical framework was established by Camporeale et al. in 2007 to compare and provide hierarchy of meandering models. A description for the interrelationships among the physical processes, which occur in curved rivers, were also explained in this mathematical framework (Camporeale et al., 2007). In spite of the considerable advancement in unraveling and understanding the dynamics of meander that was let out by linear models, the negligence of high-curvature effects was one of the reasons that made them defective (Blanckaert and De Vriend, 2010; Seminara, 2006) in addition to the limited validity to weak curvatures (Yeh and Kennedy, 1993; Blanckaert and De Vriend, 2003). Due to the fundamental drawback of the linear approach, a number of nonlinear models (Jin and Steffler, 1993; Yeh and Kennedy, 1993) were suggested although they are difficult to code and more expensive to compute.

Blanckaert and De Vriend worked to improve the accuracy of the linear models. Their development to rectify the model was by inclusion of a correction factor to the linear prediction model for tight bends. The feedback between the velocity of the downstream and the secondary circulation is incorporated by this correction factor (Blanckaert and De Vriend, 2003). According to Johannesson and Parker (1989) and Blanckaert and Graf (2004), for a strong bend curvature where the maximum velocity occurs in the lower part of the water column, a boundary shear stress and the redistribution of downstream velocity will be presented. The dominant mechanism for this redistribution is the interaction between the secondary circulation and the advective transport of downstream momentum. Subsequently, they developed a nonlinear model through incorporating these terms into the formulation of linear model. Furthermore, due to the continuous variation of the radii of curvature in the streamwise direction of meandering bends, the accelerations of convective flow occur and cross-circulation changes from section to section (Termini and Piraino, 2011). The cross sectional flow according to their model was decomposed into two parts: the first part is the

cross-circulation, caused by channel curvature, and the second part is the convective component, which is established due to the variation of the channel curvature. Thus, the distribution of the radial velocity component is determined based on the summation of the convective and cross-circulation distribution components. However, the vertical average of the cross-circulation in the model provided by Dietrich and Smith (1983) and Yalin (1992) was a zero and a net of flux of mass is formed in the radial direction.

2.7. Modelling the Effects of Secondary Flows

The development of the secondary flow in the channel bends can be attributed to the local imbalance between the centrifugal forces and the transverse pressure forces, which is generated by the super-elevation of the water surface. The influence of secondary currents on bend flow can be predicted using mathematical and numerical models (Song et al., 2012). The effective stresses should be included in the depth-averaged calculations as Flokstra showed if the secondary flows were to be predicted (Flokstra, 1977). An equation was developed by Johannesson and Parker to predict the lateral distribution of the depth-averaged main flow velocity in curved rivers (Johannesson and Parker, 1989). They reported that the reason behind the considerable external redistribution of main flow velocity is the convective transfer of main flow momentum by the secondary flow. Also, they quantified the redistribution of primary momentum phenomenon due to the secondary flow in the case of uniform flow bends. A hybrid integral-differential formulation was derived by Yeh and Kennedy (1993) in constant radius open channels. And in order to formulate the secondary flow and the influences of curvature on the profile of the primary-flow velocity, they used the integrated equations for the flux of the moment of momentum (Yeh and Kennedy, 1993). They clarified the necessity of the consideration of moment formulation for elucidating the interaction between the secondary and main flows. The most popular methods that have been widely used for describing the bend flow in the problems of shallow water are:

- ***2D Vertically Averaged and Moment (VAM) model***

This method is based on combining the depth-averaged continuity and momentum equations with additional moment-of momentum equations. The latter is derived from the balance

among the momentum fluxes in terms of the convective, pressure gradient, and stress as follows (Ghamry and Steffler, 2005):

$$\frac{\partial h}{dt}+\frac{\partial q_j}{\partial x_j}=0 \tag{2. 1}$$

$$\frac{\partial q_j}{dt}+\frac{\partial}{\partial x_j}\left(\frac{q_i q_j}{h}\right)+gh\frac{\partial}{\partial x_j}(h+H)-\frac{1}{\rho}\frac{\partial \tau_{ij}}{\partial x_j}+\frac{1}{\rho}\tau_{bj}-\frac{1}{3}\frac{\partial}{\partial x_j}\left(h\hat{u}_i\hat{u}_j\right)=0 \tag{2. 2}$$

$$\frac{\partial \hat{u}_i}{dt}+\frac{\partial}{\partial x_j}\left(\frac{q_j\hat{u}_i}{h}\right)+\hat{u}_k\frac{\partial}{\partial x_k}\left(\frac{q_i}{h}\right)=\frac{2}{3}\left[\frac{4\tau_{ij}}{h\rho}\frac{\partial z_m}{\partial x_j}-\frac{4\tau_{iz}}{h\rho}+\frac{2}{h\rho}\tau_{bi}\right] \tag{2. 3}$$

where;

i= 1, 2, t= time; q_1, q_2= flow discharge per unit width in the x-, y- directions, respectively; g= acceleration of gravity; h= flow depth; H= bottom elevation; τ_{ij}= vertically averaged total turbulent shear stress in the ij-direction; τ_{bi}= bed shear stress; $\hat{u}_1, \hat{u}_2$= velocities at the water surface in excess of mean velocity in the x-, y-directions, respectively; and z_m= mean flow depth.

Two shortcomings can be indicated when using this method. Firstly, more computational efforts are required because the solution needs additional transport equations. Secondly, the friction factor impacts, curvature ratio, and the distribution of the transversal velocity are not discernible in the mathematical formulation (Blanckaert and De Vriend, 2003).

- ***The Depth-Stress Averaging Approach***

The Depth-Stress Averaging Approach adopts the average time in the 3D Navier–Stokes equations. Using the average depth in the equations result in vertically averaged and 3D Reynolds equations as shown in Equation (2. 4) (Ahmadi et al., 2009):

$$\begin{aligned}\frac{\partial}{dt}\int_H^{H+h} u_i(z)dz+\frac{\partial}{\partial x_j}\int_H^{H+h} u_i(z)u_j(z)dz+gh\frac{\partial(H+h)}{\partial x_i}\\ -\int_H^{H+h} v\frac{\partial^2 u_i(z)}{\partial x_j\partial x_j}dz+gn^2\frac{U_i\sqrt{U_jU_j}}{h^{1/3}}=0\end{aligned} \tag{2. 4}$$

where;

$u_i(z)$= vertical distribution of *i*-component velocity; v= kinematic eddy viscosity; n= Manning's roughness coefficient; and U_i= the depth averaged velocity in *i*-direction.

The main advantage of this approach is that it is not necessary to solve additional transport equations because the influence of the secondary flow can be activated with any vertical velocity profile given. As a result, difference between the vertically varying velocity and the velocity of the mean flow is integrable. In order to include the characteristics of the channel and flow variables, like the depth of the flow and the channel curvature, the equation in the above needs calibration parameters.

2.8. The Secondary Currents Velocity Profiles

To illustrate the velocity profiles of secondary currents, Figure 2.7 shows a comparison between the empirical and the theoretical profiles of transverse velocity and the experimental results provided by Rozovskii (1961) and Guymer (1998). The following points can be highlighted (Song et al., 2012):

- The classical formula developed by De Vriend (1976) has a robust mathematical background and been widely tested in the numerical simulation of bend flow. This formula considers the no-slip boundary condition at the bottom region and, unlike other theoretical profiles that overestimate the transverse velocity, it provides outputs with a good approximation to the observed data over the depth.
- The perpendicular component (due to the curvature of the main flow) and the parallel component (due to the curvature of the main flow) to the main flow direction were considered explicitly in the derivation procedure (De Vriend, 1976).
- Although the research by Seo and Jung (2010) is in need for additional verifications under various conditions, the provided performance curve appeared to be satisfactory (Seo and Jung, 2010).
- This study used the vertical distribution of transverse velocity proposed by De Vriend (1976) to reflect the effect of secondary flow in the mathematical and numerical models.

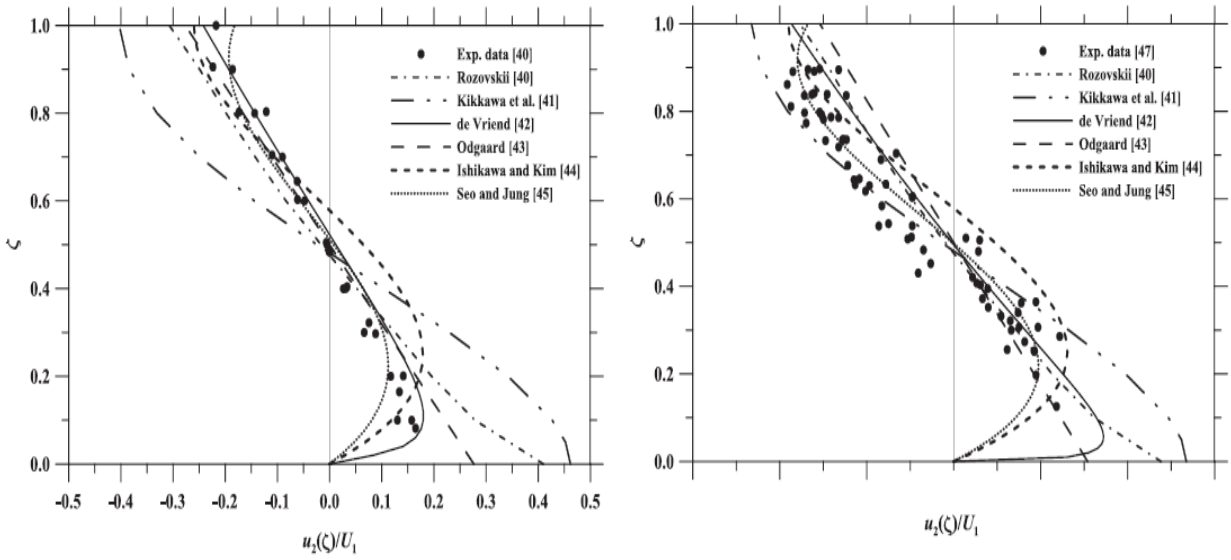

a- Rozovskii channel b- Guymer channel

Figure 2.7: Vertical distributions of transverse velocity (Song et al., 2012).

2.9. The Common Aspects of River Confluences

As mentioned previously in Chapter one, river confluences result from the convergence of two streams pour in one course downstream. Confluences could be asymmetrical or symmetrical (Y-shaped) according to the planform geometry as shown in Figure 2.8. The asymmetrical case occurs when tributaries join to the main channel laterally (Ludeña, 2015), while the symmetrical ones occur when two joined channels form a new channel downstream (Mosley, 1976).

Several parameters characterize the river confluences like the angle of junction, symbolized by α, and the discharge ratio between the tributary and main channel discharges (Q_r) and momentum flux ratios (M_r), as shown below:

$$Q_r = \frac{Q_t}{Q_m} \tag{2. 5}$$

$$M_r = \frac{\rho Q_t U_t}{\rho Q_m U_m} \quad (2.6)$$

where Q is the flow discharge, U is the mean flow velocity, and ρ is the water density. The sub-indexes t, and m indicate to the tributary and the main channel, respectively.

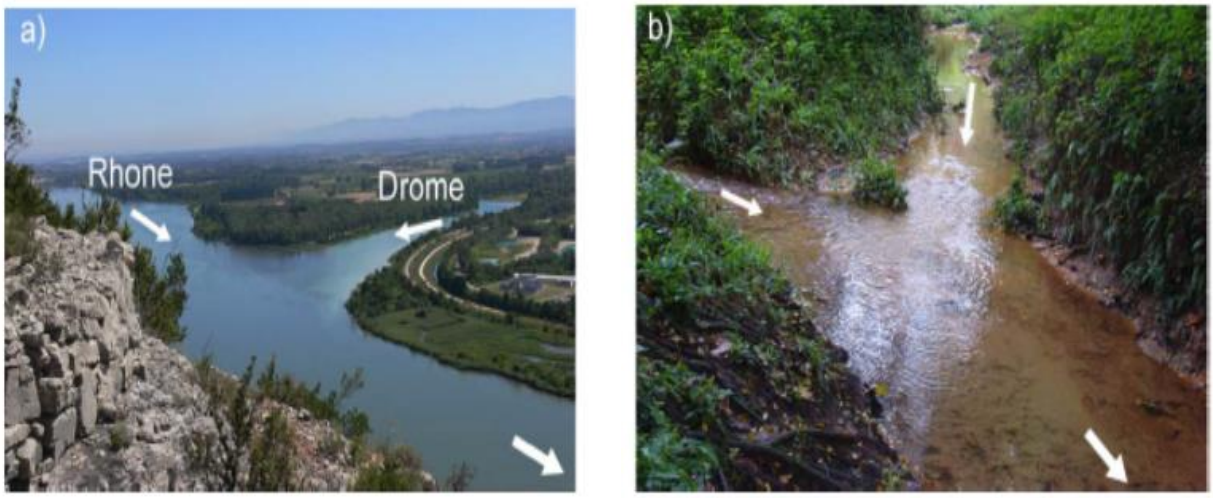

a) Asymmetric confluence b) Symmetrical (Y-shaped) confluence

Figure 2.8: Types of river confluences (Ludeña, 2015).

2.10. Secondary Flow in Confluent Channel

Commonly, confluent river bends could be found in curved river systems as a type of junction configuration (Davis, 1903; Flint, 1980). In an attempt to understand the features of the flow in confluent rivers, a lot of theoretical (Ramamurthy et al., 1988; Hsu et al., 1998), experimental (Gurram et al., 1997; Weber et al., 2001), and numerical studies (Ramamurthy et al., 2007; Shakibainia et al., 2010) have been conducted. However, investigations on the mechanism of secondary currents, the effects of these secondary currents, and the bed morphology patterns in confluent rivers are still limited (Riley, 2013; Song et al., 2012). One of the commonly known investigators in flow phenomenon of the confluent rivers was conducted by Taylor, who returns to him the pioneering achievement in this field. Based on Taylor study in 1944, the momentum analysis that resulted in a predictive equation for the depth ratio of the confluent channel was performed (Taylor, 1944). Using a rectangular open

channel, a laboratory experiment was carried out by Webber and Greated in 1966 to characterize the bulk flow variables at the intersections of the channels (Webber and Greated, 1966). The characteristics of six main regions in confluent rivers were specified and described by Best in 1987 as described below (Figure 2.9) (Best, 1987):

- Stagnation zone: It lies in the area of the confluence at the upstream corner. This zone is followed by the deflection of the flow in the two connected channels, and it is accompanied with a reduction in the flow velocity and shear stress, and an increase in the pressure and flow depth.
- Flow deflection zone: This zone is located immediately after the stagnation zone, where the deflection of the flow of the main channel occurs towards its external bank due to the incoming tributary flow.
- Flow separation zone: This zone exists at the corner of downstream junction due to the changing in direction of the flow of the tributary. The separation of the flow from the internal bank of the main channel could be accompanied with this zone in addition to the low pressures and flow recirculation.
- Acceleration zone: This zone lies in the region confined between the separation zone and the external bank of the main channel at the downstream of the junction. It is called acceleration zone due to the high velocity of the flow, which could reach the maximum at this area in addition to the increasing in the shear stress.
- Shear layers: These layers could be found in two regions in the main channel due to the high velocity gradients. The first one is located in the region confined between the recirculation zone and the surrounding flow, while the second one is located in the buffer zone between the two flows of the tributary and main channel.
- Flow recovery zone: This zone occurs after the ending of the confluence hydrodynamics impact on the flow. The two flows from the tributary and the main channel come together towards the downstream of the main channel.

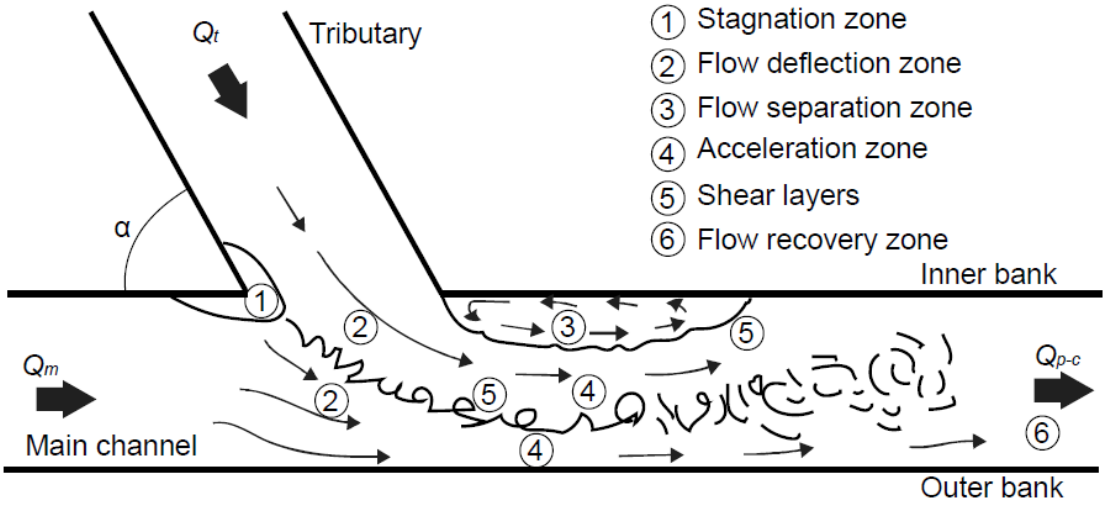

Figure 2.9: The hydrodynamics of confluent channels (Ludeña, 2015).

Many studies have been done to study the structure of the flow and mixing patterns in river confluences. Some of these studies were conducted in natural confluences such as Rhoads and Kenworthy (1995), and De Serres et al. (1999). Others were carried out in either a laboratory fixed-bed confluence such as Weber et al. (2001) study, or in a laboratory movable-bed confluence like the experiment conducted by Leite Ribeiro et al. (2012). The numerical simulation also has had a role in studying the flow of the confluences like the studies of Lane et al. (1999), and Bradbrook et al. (2001).

The hydrodynamics of the confluences are affected significantly by the so-called bed discordance, which could be defined as the difference in levels between the bed of the main channel and the bed of tributary.

In the discordant confluences, the upper part of the flow in the main channel, which is close to the surface, deviates towards the exterior bank due to the inflow of the tributary. On the other hand, the lower part of the flow, which is close to the bed, is not affected because of the bed discordance between the two channels (Biron et al., 1996; Leite Ribeiro et al., 2012).

Secondary currents appear at the downstream of the confluence on the form of two helical flow cells rotating against each other. They are produced by converging flows and separated

by a shear layer as reported by Mosley (1976). Many studies paid a great attention in studying these secondary currents in river confluences. Some of them were carried out in the field such as (Rhoads and Kenworthy, 1995, 1998; Rhoads, 1996; Rhoads and Sukhodolov, 2001; Riley et al., 2015) and others in the laboratory such as (Mosley, 1976; Weber et al., 2001). Whereas (Bradbrook et al., 1998) have conducted their investigation on the secondary currents by the means of numerical models.

According to Rhoads and Kenworthy (1995), there is a similarity between the flow structures of the river confluences and river bends because of the existence of the helical cells at the downstream of the confluence, which are produced by the curvature in the flow deviation area. The secondary currents in the asymmetrical confluences are more sophisticated (Rhoads and Kenworthy, 1995; Rhoads and Sukhodolov, 2001) than those in the symmetrical confluences (Rhoads and Sukhodolov, 2001) because the curvature adopted by the tributary inflow in the asymmetrical confluences is greater than those in the symmetrical confluences, which leads to more helical cells on the tributary side of the shear layer.

The momentum flux ratio affects the secondary currents. Noting that, these secondary currents on the tributary side are larger than that on the main channel side (Rhoads and Kenworthy, 1995; Rhoads, 1996; Riley et al., 2015).

Bed discordance enhances the secondary flow, in addition to the planform curvature and junction angle (Lane et al., 1999; Bradbrook et al., 2001; Riley et al., 2015). The secondary currents are generated in absence of planform curvature for specific combinations of depth and velocity ratio according to the numerical study of Bradbrook et al. (1998). The reason behind the absence of secondary flow cells in a natural confluence in the Río Paraná (Argentina) returns to the high form roughness and the high width to depth ratio as the attribution of Parsons et al. (2007).

Two-dimensional approaches have been used in different studies to examine the numerical simulation of river confluences, for either research purposes or for case studies (Ludeña, 2015). Due to the good agreement that have been obtained from the comparison between the numerical results and field or experimental measurements, the simulation of the confluence hydrodynamics by using three-dimensional models was recommended by Lane et al. (1999),

especially if the two-dimensional numerical model does not execute any alteration for the influence of the secondary current on the flow structure.

At present, the simulation of confluence hydrodynamics by using three-dimensional models could be considered more common (Bradbrook et al., 2001; Shakibainia et al., 2010). Using the unsteady turbulence models for these simulations were recommended by Parsons (2003) in order to fully capture the flow structures due to the presence of shear layers.

CHAPTER THREE

MATHEMATICAL AND NUMERICAL MODEL

3.1. Introduction

The experimental investigation and theoretical calculation are considered the major methods to predict the fluid flow processes. Although the actual measurement and experimental investigations is the best approach to get accurate information about physical processes, it could be too expensive. The use of the scaled models and conditions is the other choice to predict the results to a full scale. However, this choice is not totally error-free.

Physical processes could be represented by a mathematical model which will be consequently the basis of the theoretical predictions. The mathematical models of fluid dynamic problems mainly contain a set of partial differential equations. Using the classic mathematical techniques to solve these equations and predict many cases of practical interest might end up with a questionable accuracy. The use of sophisticated computers and implementing numerical methods would enhance the level of accuracy besides other advantageous such as: low cost, speed, complete and detailed information, capability in simulating both realistic and ideal conditions. On the other hand, the disadvantages of using the numerical calculation would be: difficulties in finding a suitable mathematical model, geometric complexities, strong nonlinearity, longer and again being more expensive to solve.

Mathematical model is considered the beginning point to any numerical method, which is consisting of boundary conditions and a group of partial differential equations. The behaviour of any flow, as described by conservation laws, depends largely on the general governing equations. Developing a solving method designed for that specific group of equations might be the best approach to get a simplification in the mathematical model (Mangani, 2010).

Thereafter, a suitable ***Discretization Method***, which is an approximation to the set of differential equations by an algebraic equation system for the variables at a number of discrete points in time and space, is necessary to be implemented. The most popular discretization methods are: Finite Volume Method (FVM), Finite Difference Method (FDM), and Finite

Element Method (FEM). The calculation of the variables is done at discrete locations, which are defined by the ***Numerical Grid***. The numerical grid is a discrete representation of the flow domain in space and time through the use of a finite number of subdomains such as elements, control volumes, etc. After that, a ***Finite Approximation*** technique has to be selected considering the choice of the discretization method and the numerical grid. It is worth to note that the accuracy of the solution would be affected by the choice of the discretization method, development, coding, debugging and the speed of the solution method. As soon as the discretization techniques build this large system of non-linear algebraic equations, it should be solved using a ***Solution Method***. The successive linearization for the equations is used in these methods and the iterative techniques are always used to solve the resulting linear systems. Generally, there are two levels of iterations. First, the inner iteration is used to solve the linear equation. Second, the outer iteration is used to solve the non-linearity and coupling of the equations. Finally, it is necessary to determine a suitable Convergence Criterion. It is essential to set stopping conditions for the inner and outer cycles to get an accurate solution to an effective manner. In order to determine whether the method is suitable or not, there are certain properties that should be available in the numerical methods. The most important properties are:

1. ***Consistency***: The discretization must be exact as the spacing between the grids tends to zero. In other words, the difference between exact and discredited equation, must approach zero as $\Delta t \rightarrow 0$ and $\Delta x \rightarrow 0$.
2. ***Stabili***ty: The errors of the numerical solution process should be decreasing over the iteration procedure. The methods that do not diverge are stable methods.
3. ***Convergence***: The discretized equation solution should tend to the exact solution as the spacing of the grid approaches zero. Since it is a very difficult task to demonstrate this property, it is usually accepted to test grid-independence for a solution.
4. ***Conservation:*** The solution must respect conservation of physical quantities on both local and global scales. This property is important because it limits solution error. Even if on fine grids, non-conservative schemes can also lead to correct solutions, conservative ones are usually preferred.
5. ***Boundedness***: The solution should lie within proper bounds. Boundedness is difficult to guarantee and often unbounded schemes have stability and convergence problems

as well.

6. ***Realizability***: The model should provide physically realistic solutions for the phenomena.
7. ***Accuracy***: It is the property of well approximating the exact solution. In other words, it is limiting the modelling, discretization, and iteration errors.

3.2. Numerical Model

Basically, there are three principles that govern the fluid motion: conservation of mass, energy, and momentum. The continuity, energy and momentum equations are the results of these principles. It is not easy to follow the track of these essential principles when the situations become more complex. The basic equations are replaced by empirical approximations, and mathematical calculations with numerical models. The numerical models could come in different forms such as one, two, or three dimensions, and steady or unsteady flow conditions etc. The derivations of basic principles are the base of all the numerical models, which are required to make some forms of numerical approximation to solve these principles considering their limitations. The model should be used in a right manner according to what it was designed for or corresponds to the approximations that it was based upon, otherwise, gross errors might appear in the predictions of the model. Therefore, it is important to promote a basic awareness of how numerical models operate and how to draw attention to some of the more common limitations that are implicit to this operation (Toombes and Chanson, 2011).

3.2.1. Types of Numerical Models

Computational Fluid Dynamics (CFD) is defined as “a branch of fluid mechanics that uses numerical methods and algorithms to solve and analyze problems involving fluid flows” (Toombes and Chanson, 2011). CFD uses a numerical model of a high order accuracy to solve a complex flow situation such as multi-fluid, three-dimensional, and thermodynamic effects. All numerical models in real situation are considered CFD models even for a simple solution of a backwater equation.

In order to analyze the fluid motion, two methods can be generally considered. First, describe the flow pattern at all points of the field of the flow. Second, use finite or control-volume

analysis to examine the finite region. In general, the control volume approach is adopted by most of the numerical models due to conservation properties.

Due to the real flow complexity, solving the governing equations is considered impossible without using some simplifying assumptions, even when using complex models and fast computers. The classification of the hydraulic models could be done through the simplifications employed by the model. Number of fluid properties and dynamic assumptions are associated with each category even though there are always exceptions to the rule (Toombes and Chanson, 2011).

3.3. Open-Channel Flow

The open channel flow describes the flow with an open surface or free surface that is in touch with the atmosphere. It could be natural such as rivers, streams, floodplains, and estuaries or artificial like canals, flumes, spillways, culverts, and weirs drainage ditches. There is no free surface in closed channels since they are full with fluid. The pressure forces are driving the fluid in this kind of channels, while the fluid is driven by gravity force in open channels. The basic force balance is between gravity and friction.

The discharges and water depths can be predicted based on channel geometry. Typically, in such kind of problems, the fluid is water, the channel has a large size, and the flow is turbulent. The free surface is treated under constant pressure since it is commonly at atmospheric pressure. The open channel includes two side walls with a bottom, and satisfies the no-slip condition. Due to friction in open channel along the boundary, the velocity always varies across the channel sections. It is a complex profile, the maximum velocity usually occurs in the mid plane around 20% below the surface. The main reason behind that is the secondary currents that circulating from the boundaries towards the center causing a resistance at the air/water interface. However, the maximum velocity occurs near the surface in the wide and shallow channels with a velocity profile approximately logarithmic from the bottom to the surface (Herreras and Izarra, 2013).

3.4. Free Surface Flows Model

There are a lot of cases that could be described by the shallow water model such as flood in

rivers, tidal fluctuations, waves on shallow beaches, estuary and bay flows, etc. Basically, it is derived from 3D incompressible Navier-Stokes equations, by depth averaging of the continuum mass and momentum balances (Dabaghi et al., 2005).

3.4.1. The Free Surface Flows Numerical Simulation

Generally, the numerical methods in various cases assumed to be either incompressible, or compressible. Both of the incompressible Navier-Stokes equations or Euler compressible equations could be satisfied for the velocity and pressure over the entire domain. Methods that mix between an incompressible liquid and a compressible gas also have been considered. Navier-Stokes equations are appropriate for the incompressible liquid, while for the compressible gas the Euler's equations are more suitable. Free surface flows can be solved by using several numerical procedures, especially in describing the motion of the free surface accurately. When the liquid domain displacement in fluid-structure interactions is small, for instance, Lagrangian methods or Arbitrary-Lagrangian-Eulerian (ALE) methods are mostly used. Furthermore, in order to follow the liquid presence, an additional unknown in the whole cavity has been introduced by Eulerian methods. This additional unknown requires a supplementary equation to guarantee the well-posedness of the problem. The most commonly used Eulerian methods are pseudo-concentration methods, the level set methods, and the Volume Of Fluid (VOF) methods. The free boundary in the level set method is defined by a level line of a smooth function. This additional function generally satisfies a Hamilton- Jacobi equation. In addition, the free boundary is determined by a level set of a smooth function in the pseudo-concentration method. This additional function satisfies an advection equation. In the VOF methods, the fluid characteristic function follows the fluid domain. In the liquid, this function has value of one, zero in the gas, and jumps over the interface. It satisfies an advection equation. Despite rigorously conserving the fluid mass, it is difficult to compute the curvature due to the lack of regularity of the characteristic function. It is well-adapted to problems with changes in the topology of the domain, or cavity filling. Mixed VOF and level set methods conjugate the smoothness character of the level sets and the mass conservation (Caboussat, 2003).

It is worth to note that determining the boundary between the water and air or the moving free surface and defining the boundary conditions are considered as one of the main challenges.

Therefore, a compatible solution with a study that focused on a river reach should be provided. Within this context, using the rating curves and flow rates might be easier and more applicable than 3D velocity vectors or pressure field due to the difficulty of the latter in measuring and controlling (Faure et al., 2004).

There are several possibilities for the free surface problem (Faure et al., 2004):

- Find the free surface by using 1D or 2D shallow water equation solver.
- Use the free surface as top boundary to solve the Navier–Stokes equations. Due to fixed free surface, this method is only considered when having steady state calculations.
- Link the 2D shallow-water equation solver and the 3D Navier–Stokes equation solver as in Hervouet and Van Haren (1996). However, the implementation of this method is considered very expensive because of the data and mesh compatibility considerations. Also, it is time consuming since the mesh is regenerated frequently.
- Conduct simulation for the water and air flows together using a multi-fluid multiphase Navier–Stokes equations solver. In this case and due to incompressibility, the quantities of air and water in each cell could be defined by their mass fraction or volume fraction. The first two features of VOF method are implemented by this scheme. However, the boundary condition at the free surface is not needed because the multi-phase homogeneous model is used and the surface tension and wind effects are neglected. In this study, the last method was chosen for the sake of simplicity.

3.4.2. A Comparison between the Free Surface Model and Rigid-Lid Model

In order to know the difference between the Free Surface Model that is used in open channel flow and the Rigid Lid Model which is used in closed channel flow, one should first know how both of them are modeled. In the Free Surface Model, both air and water flows are considered in the simulation which allows for a deformed interface, while in the Rigid-Lid Model, only the water flow is considered as shown in Figure 3.1. The use of Rigid-Lid Model in the study of numerical modelling for curved channel flow has been proliferated in the past two decades. In 1998, Hodskinson and Ferguson used the Rigid-Lid Model to simulate the flow separation in highly curved channel. They obtained a good agreement with the measured

data of the flow velocity (Hodskinson and Ferguson, 1998). Through the use of curved channel, a study was conducted by Blanckaert et al. in 2009. This study included field measurements, laboratory experiments and numerical simulations, and it has been carried out by using a Rigid-Lid Model with a 3D LES (Large Eddy Simulation), and RANS (Reynolds Averaged Navier-Stokes) CFD codes. They concluded that the use of 3D LES model in the simulation of the flow hydrodynamics for the experiments was successful, and the simulation of the flow hydrodynamics by using 3D RANS code was successful in the case of a mobile bed, while it was frequently worse in the case of a horizontal bed (Blanckaert et al., 2009). According to the study of Booij in 2003 that was performed using shallow curved free surface flows, the main features of major and secondary flows could be produced by the RANS computations, while shear stresses and other flow aspects could be reproduced correctly by the 3D LES (Booij, 2003b).

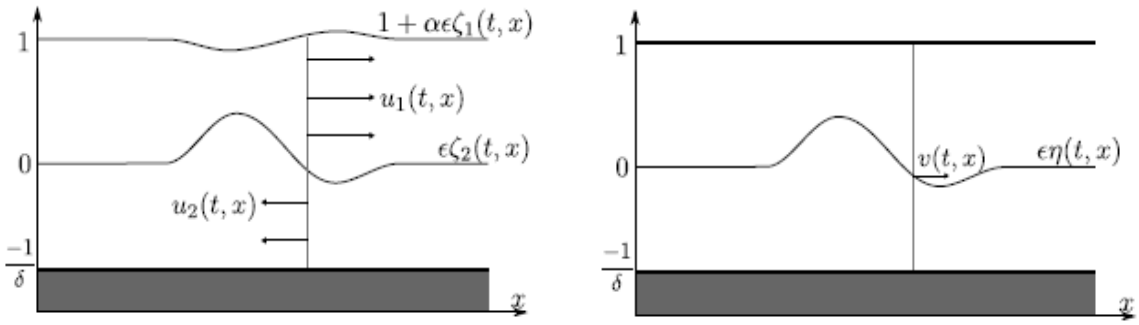

a- Free Surface Model. b- Rigid-Lid Model.

Figure 3.1: The domain in the two different models (Duchêne, 2014).

3.5. Hydrodynamic Modelling of Curvature Flow

Typically, three components for the sinuosity models are accompanied by a secondary current: (1) sinuosity planform and migration, (2) sinuosity morphology, and (3) sinuosity hydrodynamics. In fact, the interaction between the hydrodynamics with the morphology and sediment transport is the main drive for the latter. Therefore, the three components are intrinsically coupled (Blanckaert and De Vriend, 2010). As the flow enters into the channel curve, an interaction between the forces, centrifugal acceleration, the slope of transverse water

surface, and bed shear stress occurs and produces a cross circulation as a result (Howard and Chang, 1988). In order to include the effect of the secondary flow, the hydrodynamic modelling of curvature flow could be mainly categorized into two categories; the linear model, and nonlinear model. Also, linear closure sub models are generally used. The first order disturbance process with the depth to curvature ratio, as a disturbance parameter, leads to these sub models. In spite of the significant progress of the linear models in understanding and revealing the dynamics of curvature, the omission of high curvature effects and validity limitation to weak curvatures make them flawed. The straight flow profile of longitudinal velocity in the vertical direction adoption is the main reason for the overestimation of the linear model, thereby ignoring the feedback mechanism. As a result, it could be concluded that the influences of the center region cell in a moderately to highly curved flow can only be modelled if the deformation of the velocity profiles at the downstream is taken in consideration. Also, the downstream velocity and the center-region cell feedback has to be considered as well. In spite of the difficulty in coding and expensive computation for nonlinear models, a number of nonlinear models have been suggested to overcome the linear approach's fundamental shortcomings. According to the previous studies, the linear model predictions for narrow curves have been amended by Blanckaert and De Vriend by including a correction factor. This factor includes the feedback between the velocity in the downstream and the secondary circulation. In the sharp bends, the downstream velocity and boundary shear stress should be modelled accurately in depth-integrated flow models. Thus, the so-called nonlinear model was developed including these terms into the linear model formulation. To satisfy the predictions in the river curves, 3D numerical models could be considered eligible for this. These models depend on the consolidation of the three-dimensional flow features with the complex spiral flow motion in the river bend. However, most of the 3D models suffer from the large amounts of computational time and possible numerical instability (Song et al., 2012). In this research, the secondary currents effect was examined on the hydraulic structures and water surface elevation in a curved channel by developing a 3D finite element model of the shallow water equations.

3.6. Mathematical Model

The conservation equations of mass, momentum and energy for incompressible flows will be described generally in this part. First, a derivation to the equations in the most general form should be done. The mathematical equations that exemplify the physical principles could be extracted by applying the suitable fundamental physical principle into an appropriate model of flow. The fluid flow has been modelled with infinitesimal control volume fixed in space and the fluid moving through it. As a result, the equations are proposed in a differential conservation form. It is important to recall the concept of the fundamental derivative in case of switching from one form to another (Anderson, 1995):

$$\frac{d}{dt} = \frac{\partial}{\partial t} + (\bar{U}.\nabla) \tag{3. 1}$$

Second, a suitable model for the fluid should be proposed; introduce the cases of interest in a simple way such as ideal gas and Newtonian fluid.

3.7. Navier Stokes Equations

The conservation of mass (continuity) and momentum laws are used to describe the flow based on the assumptions mentioned earlier. The Navier Stokes equations in the x, y and z directions and the continuity equation that describes the flow are shown in equations below.

Momentum in x-direction;

$$\frac{\partial}{\partial t}(\rho u) + \frac{\partial}{\partial x}(\rho uu) + \frac{\partial}{\partial y}(\rho vu) + \frac{\partial}{\partial z}(\rho wu) = -\frac{\partial P}{\partial x} + \mu\left(\frac{\partial^2 u}{\partial x^2} + \frac{\partial^2 u}{\partial y^2} + \frac{\partial^2 u}{\partial z^2}\right) \tag{3.2}$$

Momentum in y-direction;

$$\frac{\partial}{\partial t}(\rho v) + \frac{\partial}{\partial x}(\rho uv) + \frac{\partial}{\partial y}(\rho vv) + \frac{\partial}{\partial z}(\rho wv) = -\frac{\partial P}{\partial y} + \mu\left(\frac{\partial^2 v}{\partial x^2} + \frac{\partial^2 v}{\partial y^2} + \frac{\partial^2 v}{\partial z^2}\right) \tag{3. 3}$$

Momentum in z-direction;

$$\frac{\partial}{\partial t}(\rho w) + \frac{\partial}{\partial x}(\rho uw) + \frac{\partial}{\partial y}(\rho vw) + \frac{\partial}{\partial z}(\rho ww) = -\frac{\partial P}{\partial z} + \mu\left(\frac{\partial^2 w}{\partial x^2} + \frac{\partial^2 w}{\partial y^2} + \frac{\partial^2 w}{\partial z^2}\right) \tag{3.4}$$

Continuity;

$$\frac{\partial}{\partial x}(\rho u) + \frac{\partial}{\partial y}(\rho v) + \frac{\partial}{\partial z}(\rho w) = 0 \tag{3.5}$$

The fluid elements for the conservation law are shown in Figure 3.2. In which:

- *y*-axis of the Cartesian coordinate system is aligned in the vertical direction.
- *u*, *v*, and *w* are the velocity components in the *x*, *y*, and *z* directions respectively
- ρ is the mass density; μ is the viscosity.
- *t* is the time.
- *P* is the pressure, and
- *g* is the gravitational acceleration.

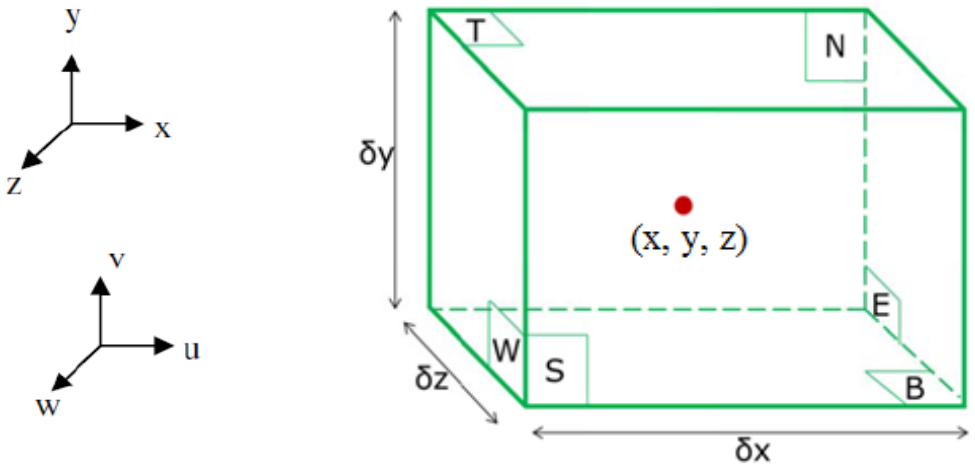

Figure 3.2: The element of fluid for conservation law (reproduced from Gildeh, 2013).

The fluid properties were assumed to be constant. However, the density changes with temperature in a proportional rate (Cable, 2009).

The continuity equation simply states that the mass is conserved or that the net accumulation of mass in the control volume is zero in the steady flow. The net mass flow is represented in each term in the continuity equation through a face perpendicular to one of the respective axis.

Equations (3.1) to (3.5) describe the flow distributions. Velocity can highly vary with time in the turbulent flow. Many models have been studied and developed in order to predict turbulent flow.

3.8. Discretization Approaches

The main purpose of derivation of the physical mathematical model is to manipulate it in an appropriate form for computer calculations. Equation discretization is the first step in this way. The discretization approach depends mainly on making a set of discrete algebraic equations as one equation for every node. The value in the node should be in relation with ones in the neighbour. Then, the numerical solution could be obtained from the simultaneous gratification of all the equations in the set. The following is a discussion and presentation for the most popular discretization techniques (Anderson, 1995).

3.8.1. Finite Volume Method (FVM)

This method depends on the integral form of the conservation equations. Basically, there are finite volumes, which come from dividing the same domain. The centroids of these volumes represent the calculation node. Boundaries between different volumes are defined by the grid and should not be relating to any metrics. In terms of nodal values, the variable values of the surface can be expressed by using interpolation. As long as surface integrals for volumes sharing the same face are equal for both of them, this method is conservative. The shortcoming of this method compared to FDM is that this method is more appropriate to the second order schemes, and is more difficult for 3D simulations due to the three levels of approximation introduced; interpolation, differentiation and integration. However, this method could be considered as the most commonly used approach in fluid mechanics due to the physical approach and the simplicity in understanding and implementing.

3.8.2. Finite Volume Method in OpenFOAM

OpenFOAM software, which is used in this thesis, is based on the FVM. The FVM is based on conservation equations in the integral form as mentioned earlier. The integration should be performed over a finite volume to get such equations. To clarify the ideas, the generic conservation equation for a transported scalar Φ is shown in (3.6):

$$\int_S \overrightarrow{J_\Phi}.\vec{n}dS = \int_S \rho\Phi(\vec{U}.\vec{n})dS - \int_S \Gamma_\Phi(\nabla\Phi.\vec{n})dS + \int_\Omega q_\Phi d\Omega \quad (3.\ 6)$$

Each control volume and also the entire domain could be applied by these equations. It is worth to highlight once again the main feature of FVM; the global conservation. The quadrature formulae should be used to approximate the three integrals in order to get an algebraic equation. A Typical bi-dimensional quadrilateral control volume is shown in Figure 3.3.

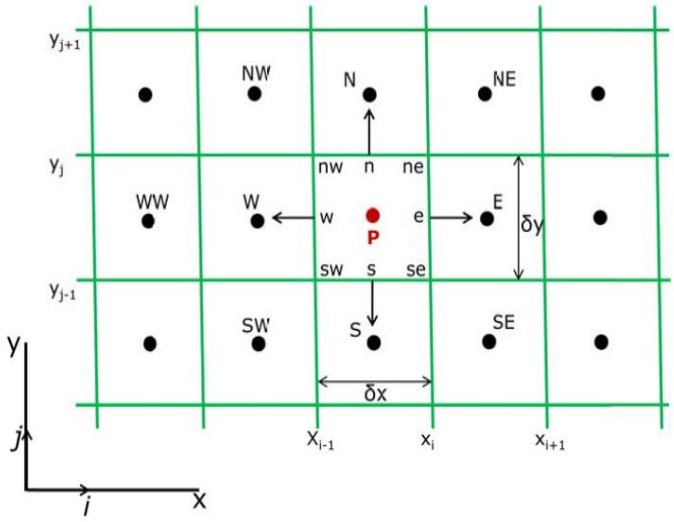

Figure 3.3: Typical bi-dimensional quadrilateral control volume (reproduced from Gildeh, 2013).

3.9. OpenFOAM

OpenFOAM (Open Source Field Operation And Manipulation) software is an open source CFD model. It has the feature of being open for changes and developments. New ideas can be contributed by users to help in extending software features. OpenFOAM can be used to create applications since it includes an open C++ library. Furthermore, it is used to define solutions for Continuum Mechanics problems based on Finite Volume Method (FVM), especially for CFD. There are two components of these applications in the OpenFOAM: solvers and utilities. The former is used to solve partial differential equations, while the latter is commonly used to manipulate data in different forms. The simplicity in creating and customizing solvers can be

considered the main advantage of the OpenFOAM. OpenFOAM classes have been used in writing the solver applications in order to facilitate the syntax to resemble the partial differential equations that is being used. In order to achieve this, there are some necessary properties for the programming language like template classes, inheritance, virtual functions and operator overloading. This could be found in few languages, one of these languages is C++. Due to the customizable nature of the software, it has become the popular choice for users who want to have a degree of control over the physics and calculation of a solution to a problem. The custom solvers and utilities for the users of OpenFOAM are often available to others. A lot of commercial and academic organizations use the OpenFOAM and many peer-reviewed papers used it as well (Lambert, 2012).

The Volume of Fluid method (VOF) is used in OpenFOAM for tracking the free surface movement (the air-water interface). The interFoam solve is used with free surface flow while the pisoFoam solver is used in the closed channel (no free surface). This method depends on determining the fraction of each fluid in every cell of the computational mesh (known as the volume fraction). The volume fraction equation's is:

$$\frac{\partial \alpha}{\partial t} + \nabla.(\alpha\, U) = 0 \tag{3. 7}$$

where U is the velocity field composed of u,v, and w and α are the water volume fraction and air volume fraction, respectively. The parameter α varies between 0 and 1. The case $\alpha = 1$ denotes a cell that is completely full of water and $\alpha = 0$ if it is full of air.

The density of the fluid inside each cell of the mesh could be determined by volume fraction, which is also known as the phase fractionα (the density that is used in solving Navier-Stokes equations). The density of the mixture is determined by:

$$\rho = \alpha\rho_w + (1 + \alpha)\rho_a \tag{3. 8}$$

where ρ_w is the density of water; and ρ_a is the density of the air.

The toolbox in OpenFOAM implements operator-based implicit and explicit second and fourth-order Finite Volume (FV) discretization in three-dimensional spaces and on curved surface, which could be considered the most important feature to help CFD programmers.

The dimensional check is one of the important advantages that is done by OpenFOAM. The dimensions of the physical quantities objects are referenced with the construction of these quantities, and only valid dimensional operations can be performed.

3.10. Model Preparation

The users of OpenFOAM can create new solvers and utilities with some pre-requisite information of the fundamental method, programming techniques and physics, which is considered one of the OpenFOAM strengths.

The pre-processing and post-processing environments have been supplied in OpenFOAM as shown in the Figure 3.4. The pre- and post-processing interface is the same as OpenFOAM utilities. Therefore, the consistent data handling across all environments is ensured. The OpenFOAM overall structure is shown in the Figure 3.5. This section aims at clarifying the usage of OpenFOAM existing applications for simulation of the flow in river bends.

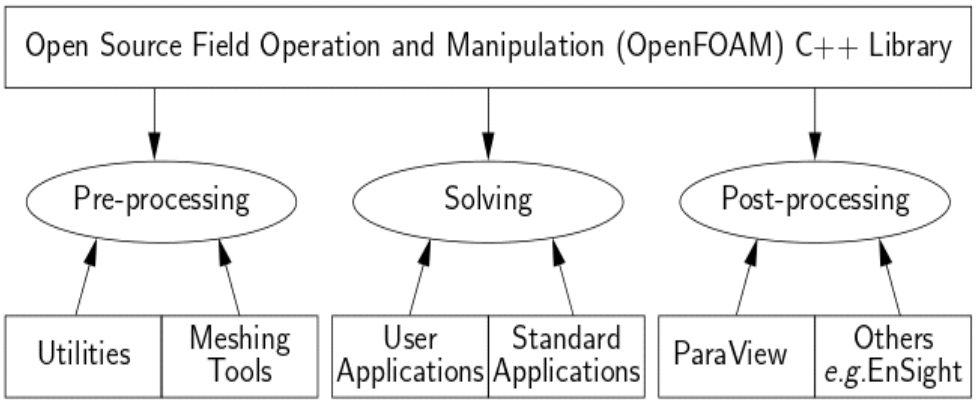

Figure 3.4: The structure of OpenFOAM (OpenFOAM programmers guide, 2015).

The case directory includes the following directories (Hjertager, 2009):

- Constant: controls mesh characteristics, material properties, and turbulence properties that correspond to each problem.
- System: defines number of iterations, time step size, and solution controls.
- 0: determines initial flow fields and boundary conditions.

The case structure is shown in the Figure 3.5.

As mentioned earlier, there are several different solvers within the OpenFOAM toolbox that are designed to solve various specific problems (Poungkrajorn, 2015). Two solvers have been selected to solve the problem regarding the experiment in this research:

InterFoam: is a transient solver for incompressible flow that is used with Free Surface Model.

PisoFoam: is a transient solver for incompressible flow that is used with Rigid-Lid Model.

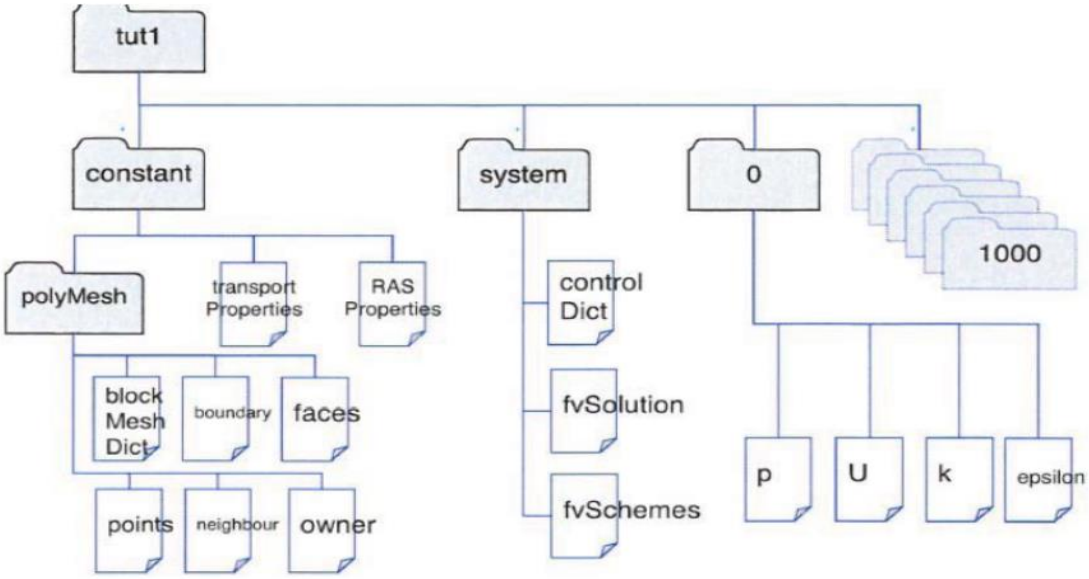

Figure 3.5: OpenFOAM case structure (Hjertager, 2009).

3.10.1. Implementation of the Solvers

3.10.1.1. InterFoam Solver

Free surface flows are characterized by a high interaction between air and water. Some of these characteristics can be reproduced by the interFoam solver of OpenFOAM, which is a multiphase solver.

3.10.1.2. PisoFoam Solver

PisoFoam is a transient solver for incompressible fluid flows and it works for both laminar

and turbulent conditions. PISO algorithm is the base of pisoFoam, which stands for Pressure Implicit with Splitting of Operators. Basically, pisoFoam is a process of pressure-velocity calculation that includes one predictor step and two corrector steps. Momentum equations are used in the predictor step for solving an intermediate pressure field, which is the concept of the SIMPLE algorithm. The correcting and ensuring the relevant parameters is done by two corrector steps in a way to satisfy the momentum and continuity equations (Versteeg and Malalasekera, 2007). Therefore, pisoFoam also could be considered as an extension of the SIMPLE algorithm by adding corrector steps in order to ensure the calculated values (Poungkrajorn, 2015).

3.11. Turbulence Modelling

Turbulent flow is one of the flow cases in fluid dynamics. It is characterized by a random motion of the fluid within a flow domain. On the other hand, laminar flow, non-turbulent or streamlines, is the flow where the fluid flows in parallel layers with no disruption between the layers. In order to indicate the type of the flow whether it is considered laminar or turbulent, Reynolds Number could be used (Cable, 2009).

Turbulent flow can be characterized by several characteristic features such as (Davidson, 2015):

- Irregularity: The turbulent flow is irregular, random and chaotic.
- Diffusivity: The diffusivity increases in the turbulent flow.
- Large Reynolds Number: Turbulent flow occurs at high Reynolds number.
- Three-Dimensional: The turbulent flow is always three-dimensional. Nevertheless, the flow can be treated as two-dimensional when the equations are time averaged.
- Dissipation: Turbulent flow is dissipative. In other words, the kinetic energy is transformed into internal energy in the small eddies.
- Continuum: The turbulent scales are small in the flow although they are much larger than the molecular scale. Also, the flow could be treated as a continuum.

The decomposition for the instantaneous variables such as the components of velocity and pressure into a mean value and fluctuating value is preferable when the flow is turbulent as shown in equation below (Davidson, 2015).

$$U_i = \overline{U}_i + u_i \tag{3. 9}$$

$$P = \bar{P} + p \tag{3. 10}$$

The reason behind the variables decomposition is that in measuring flow quantities the mean values are commonly more interesting than the time histories.

In addition, solving the Navier-Stokes equation numerically requires a very fine grid to solve all turbulent scales. The fine resolution in time is required as well because the turbulent flow is always unsteady.

The equation of continuity and Navier-Stokes equation can be written as shown below:

$$\frac{\partial p}{\partial t} + (\rho U_i) = 0 \tag{3. 11}$$

$$\frac{\partial p U_i}{\partial t} + \left(\rho U_i U_j\right)_j = -P_i + \left[\mu\left(U_{i,j} + U_{j,i} - \frac{2}{3}\sigma_{i,j}U_{k,k}\right)\right]_j \tag{3. 12}$$

where $(.)_{,j}$ indicates the derivation with respect to x_j.
In order to deal with the incompressible flow, the last term on the right hand side of Equation (3. 12) is neglected. So that the equation will be:

$$\frac{\partial p U_i}{\partial t} + \left(\rho U_i U_j\right)_j = -P_i + \left[\mu\left(U_{i,j} + U_{j,i}\right)\right]_j \tag{3. 13}$$

The following equations are obtained after time averaging of the continuity and Navier-Stokes equations.

$$\frac{\partial p}{\partial t} + (\rho \overline{U}_i)_{,i} = 0 \tag{3. 14}$$

$$\frac{\partial p \overline{U}_i}{\partial t} + \left(\rho \overline{U}_i \overline{U}_j\right)_j = -\bar{P}_i + \left[\mu\left(\overline{U}_{i,j} + \overline{U}_{j,i}\right) - \rho\overline{u_i u_j}\right]_j \tag{3. 15}$$

where $\overline{u_i u_j}$ is the Reynolds stress tensor. The above equations are called Reynolds-Averaged Navier Stokes (RANS) equations. Different turbulence models could be used to perform the estimation of Reynolds stress tensor as described below.

3.11.1. Various Turbulence Models

Turbulence models have been developed in different types by solving the Navier Stokes equations and Reynolds-Averaged Navier Stokes (RANS) based on modelling approach that reduces the computational efforts and resources using time averaging the flow quantities for a whole range of scales of turbulence that are being modeled (Cable, 2009). Several models, that are included in RANS turbulence models, have been developed in increasing order of complexity, ability to model the turbulence, and cost in terms of computational work (CPU time) Such as (Davidson, 2015):

- Algebraic (zero equation) models: mixing length (first order model);
- One equation models: k-model, μt-model, Spalart-Allmaras (first order model);
- Two equation models: k- ε, k- kl, k- $\omega 2$, low Re k- ε (first order model);
- Algebraic stress models: ASM (second order model); and
- Reynolds stress models: RSM (second order model).

A brief explanation for each group of the turbulence models is shown below:

I. Algebraic models: Turbulent viscosity or even often called eddy viscosity is computed by an algebraic equation. Eddy viscosity models are based on a turbulent (eddy) viscosity.

II. One-equation models: The turbulent quantity (commonly the turbulent kinetic energy), for this kind of models is obtained from a transport equation. In addition, an algebraic expression is solved for a second turbulent quantity, commonly a scale of turbulent length. Boussinesq assumption is usually used for calculating the turbulence viscosity.

III. Two-equation models: These models lie within the class of eddy viscosity models. In order to describe the transport of two scalars, two transport equations are derived; the turbulent kinetic energy k and its dissipation ε. Then, the assumption that relates the Reynolds stress tensor to the velocity gradients and an eddy viscosity is used to compute the Reynolds stress tensor. The eddy viscosity is gotten from the two transported scalars.

IV. Reynolds stress models: In this case, the derivation of the transport equation is used for the Reynolds tensor. In order to determine the length scale of the turbulence, one transport equation should be added, commonly the dissipation ε equation is used.

The $\boldsymbol{k-\varepsilon}$ model is widely used because of several features such as; the robustness and reasonable accuracy that it provided for a large number of turbulent flows (Cable, 2009).

3.11.1.1. Boussinesq Assumption

Boussinesq assumption could be described as the relationship between the Reynolds stresses and the velocity gradients via the turbulence viscosity. It is written as:

$$\left[\mu\left(\overline{U}_{i,j}+\overline{U}_{j,i}\right)-\rho\overline{u_i u_j}\right]_j=\left[(\mu+\mu t)\left(\overline{U}_{i,j}+\overline{U}_{j,i}\right)\right]_{,j} \tag{3. 16}$$

which gives:

$$\rho\overline{u_i u_j}=-\mu t\left(\overline{U}_{i,j}+\overline{U}_{j,i}\right)_{,j} \tag{3. 17}$$

or,

$$\rho\overline{u_i u_j}=-\mu t\left(\overline{U}_{i,j}+\overline{U}_{j,i}\right)+\frac{2}{3}\delta_{ij}\rho k \tag{3. 18}$$

where the last term is equal to zero in incompressible flows.

3.11.1.2. Algebraic Models

An expression for the turbulent viscosity is required in eddy viscosity models ($\mu t=\rho vt$). The dimension of vt is $[m^2/s]$. A scale of turbulent velocity multiplied with a scale of turbulent length gives the right dimension such that:

$$vt\propto u\,\ell \tag{3. 19}$$

where u and ℓ are the characteristic for the large turbulent scales.

This is considered reasonable since most of the transport by turbulent diffusion lies under the responsibility of these scales. The velocity gradient is used as a velocity scale in the algebraic turbulence model. Also, some of the physical length is used as the length scale. In boundary layer-type of flow, the dimension of vt is:

$$vt = \ell_{mix}^2 \left|\frac{\partial U}{\partial y}\right| \quad (3.\ 20)$$

where y is the coordinate normal to the wall; ℓmix is the length of mixing; and the model is named as the mixing length model. This model is hardly used anymore since it is an old one. The only problem in this model is that ℓmix is unknown and should be determined. More modern algebraic models are the Baldwin-Lomax model (Baldwin and Lomax, 1978) and the Cebeci-Smith model (Cebeci and Smith, 1974) which are commonly used in aerodynamics when the flow is computed around aeroplanes, airfoils and in other situations.

3.11.1.3. One Equation Models

The transport equation is mostly solved for the turbulent kinetic energy in one equation models. An algebraic expression is often used for the unknown turbulent length scale, which should always be given. For instance, the length scale can be taken as commensurate to the boundary layer thickness, the width of a jet or a wake. Due to the impossibility of this model in finding a common expression for an algebraic length scale, it is not appropriate to general flows, which is considered the main shortcoming for this type. Despite that, several suggestions were made where the scale of turbulent length is computed in a more common way.

3.11.1.4. Two-Equation Turbulence Models

Turbulent flows include two-equation models; the Standard *k-ε* model and the Modeled *k* Equation.

The ***k-ε*** model is one of the turbulence models that is used in Computational Fluid Dynamics (CFD). It is mainly used for developed and general turbulence. The model allows for the impact of transport of turbulence properties by convection, diffusion, and the production and destruction of turbulence. Since it is a two equation model, the description of turbulence is given by means of two transport equations (PDEs); the turbulent kinetic energy (k), and the rate of dissipation of turbulent kinetic energy (ε). The turbulent viscosity is isotropic and the main presumption of this model is considered according to Versteeg and Malalasekera (2007). Accordingly, the ratio between Reynolds stress and mean rate of deformation is the same at

all directions. Nevertheless, the inaccurate predictions makes this assumption failing in many complex flows (Tawekal, 2015).

The evaluation for the standard k-ε according to Versteeg and Malalasekera can be summarized as follows (2007)

- Advantages
    - It is considered the simplest turbulence model because there is no need to specify the initial and/or boundary conditions;
    - a very good performance was given by this model, especially in many industrially relevant flows;
    - The model is well established; and It is the most extensively certified turbulence model.
- Disadvantages
    - It could be considered expensive comparing with other turbulence models like mixing length model; and
    - The performance of the model could be considered poor in assortment of significant cases such as:
        - Unconfined flows;
        - Flows with large extra strains;
        - Rotating flows; and
        - Flows driven by anisotropy of normal Reynolds stresses.

Further details for all the turbulence models are provided in the Appendix A.

CHAPTER FOUR

RESULTS AND DISCUSSIONS

Part One: Curved Channel

4.1. Experimental Work

Several experimental studies have been conducted in curved open channels. However, there is little data available for strong curvatures (mean radius to width ratio of order 3 or below) including detailed and suitable data. One of the previous experimental studies on curved channels is the experimental study of Rozovskii (1961) who reported the velocity fields and water surface results in a 180-degree sharp curved channel. It can be considered suitable for the verification of the present model because its ratio of mean radius to width was 1.0 and such a strong curvature would induce intense secondary current effect.

4.2. Numerical Model Verification

To verify the employed model, it was applied in the channel shown in Figure 4.1. This channel consists of a straight approach channel (Rozovskii experimental data) with a length of (6 m), followed by a 180˚ bend with a mean radius of (0.8 m) and outlet sections of (3 m). The cross section was a (0.8 m) wide rectangle, and the entire channel was set on a horizontal bed (Song, et al., 2012).

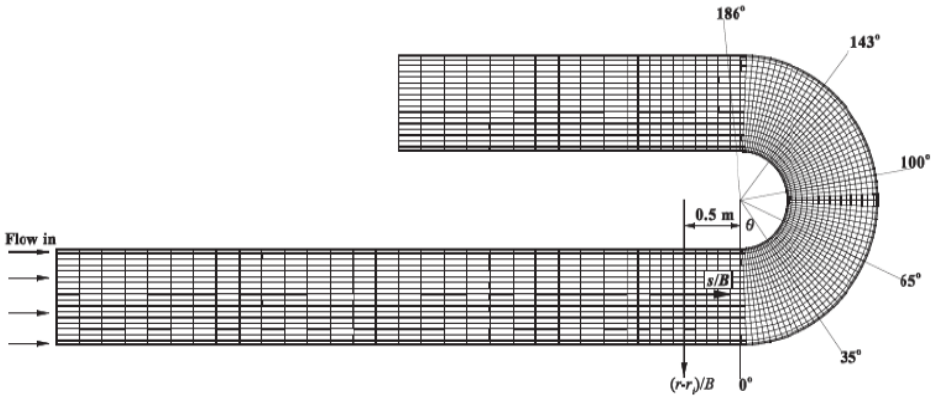

Figure 4.1: Rozovskii experimental data (Song et al., 2012).

Table 4-1: shows the characteristics of the channel and some hydraulic data obtained from Rozovskii experiment.

Table 4-1: The dimensions of the curved channel and flow conditions (developed from Rozovskii).

Variable	Symbol	Value
Upstream discharge	Q	0.0123 m^3/s
Downstream water depth	h	0.058 m
Channel width	B	0.8 m
Bend angle	θ	180º
Internal radius of curvature	r_i	0.4 m
Mean radius of curvature	r_c	0.8 m
Mean radius to width ratio	r_c/B	1.0
Che'zy factor	C	60
Mean velocity at downstream	U_∞	0.265 m/s
Tailwater Froude number	Fr_d	0.35

4.3. Computational Domain and Mesh Generation

The determination of computational domain dimensions was done based on Rozovskii experiment, and it consists of a straight approach channel with a length of (6 m), followed by a 180° bend with a mean radius of (0.8 m) and outlet sections of (3 m). The cross section is a (0.8 m) wide rectangle, and the entire channel was set on a horizontal bed. There are some differences between the computational domain and the experiment includes adding a drop at the end of the channel (0.05 m depth) to control the depth of water. The depth of the channel in the case of open channel flow (Free Surface Model-FSM) was used as (0.3 m); while in the case of closed channel flow (Rigid-Lid Model-RLM) was used as (0.058 m). Figure 4.2 shows the two domains.

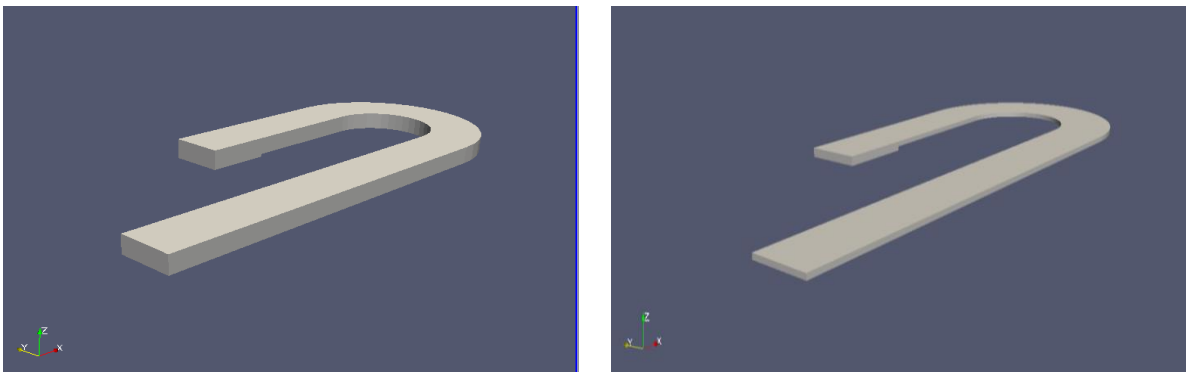

a- Free Surface Model. b- Rigid-Lid Model.

Figure 4.2: The computational domain for channel bend.

In order to capture the flow features and velocity characteristics in better accuracy, a refined mesh is used for all simulations as shown in Figure 4.3, taking in consideration that the mesh is increasing towards the walls of the channel to be finer in order to get more accurate results.

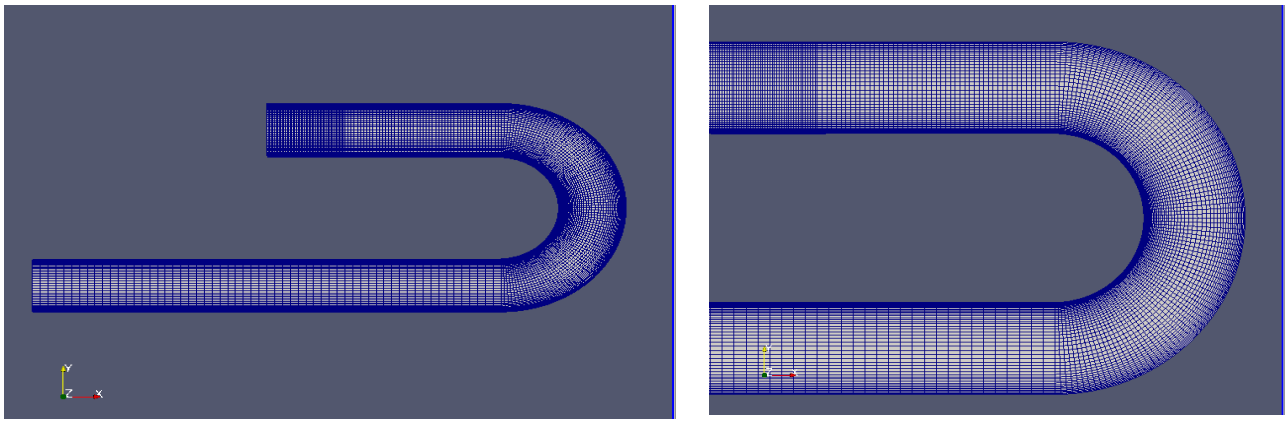

a- The mesh of the channel. b- The mesh of the bend.

Figure 4.3: The mesh of the channel bend.

4.4. Turbulence Models

Due to the complexity of the turbulence models in the case of turbulent flow, it is generally considered difficult to find a single turbulence model that could be applied to all situations of turbulence, according to the previous studies in this field. Therefore, the choice of the best suitable turbulence model is not an easy task, and there are some matters that should be taken into consideration in the selection process such as the physics encompassed in the flow, the level of accuracy, and the computational resources available.

Four turbulence models have been used in this study in order to assess the performance of each one for secondary current in river bends (more details can be found in the appendix):

RAS turbulence models

- *kEpsilon*: Standard *k-ε* model
- *realizableKE*: Realizable *k-ε* model
- *LRR*: Launder-Reece-Rodi RSTM

LES turbulence model

- *oneEqEddy*: *k* -equation eddy-viscosity model

4.5. The Numerical Simulations

The simulations in this study was done by using OpenFOAM (OPEN Field Operation And Manipulation) which is an open source CFD program written mainly in C++. A number of solvers come with this program, and each one of these solvers is designed for solving a specific fluid mechanics problem. Also, there are utilities to perform data manipulation.

Basically, OpenFOAM uses the Finite Volume Method, FVM, and it includes a lot of numerical schemes that are implemented both for time and space integration. Two solvers were used in this study, the first one is interFoam solver which has been used for incompressible and turbulent flows in open channel flow (Free Surface Model), and the other one is pisoFoam solver which has been used also for incompressible and turbulent flow but in closed channel cases (Rigid-Lid Model).

4.6. Initial and Boundary Conditions

In the domain of curved channel, there are four types of boundaries: the inlet and the outlet of the channel, the walls (including side walls and bottom), and the surface of the channel (atmosphere). There are one or more faces in each of these boundaries. It is necessary to determine the initial and boundary conditions for each type of these boundaries before running the simulation. A summary of the boundary conditions of each type of boundaries is presented below:

- Velocity:

  The inlet boundaries of the velocity have been chosen as a ***fixedValue*** condition, while the outlet boundaries of the velocity were set as a ***zeroGradient*** which means (the normal gradient of velocity is zero). The boundary conditions of the side walls and lower walls were specified as a ***fixedValue*** conditions with a uniform value of (0, 0, 0), which means that no-slip velocity condition is assumed at the walls and the velocity at the walls is zero. For the top of the channel (atmosphere), the boundary condition was determined as a ***zeroGradient*** when using the solver interFoam, and a ***symmetryPlane*** when using the solver pisoFoam.
- Pressure:

  The boundary conditions of the pressure were set as a ***zeroGradient*** except for the

atmosphere, where the pressure was specified as a ***totalPressure*** with zero value for the case of using the interFoam solver, and a ***symmetryPlane*** for the case of using the pisoFoam solver.

- Turbulent kinetic energy (***k***):

  According to Huai et al. (2010), $\boldsymbol{k=0.06u^2}$, where ***k***= Turbulent kinetic energy, and ***u*** = the mean velocity. The boundary conditions of the turbulent kinetic energy were determined as follows: ***fixedValue*** at the inlet with the value of ***k*** as calculated from the above equation, ***zeroGradient*** at outlet and the atmosphere, and finally the wallFunction (***kqRwallFunction***) has been used for the side and lower walls which provides a suitable condition for *k* fields for the case of Reynolds number flow. In the case of using the solver pisoFoam instead of interFoam, the only difference is that the boundary condition of the atmosphere changes to ***symmetryPlane*** instead of ***zeroGradient***.

- Rate of kinetic energy dissipation (***ε***):

  According to Huai et al. (2010), $\boldsymbol{\varepsilon=0.06u^3/D}$, where ***ε***= the rate of dissipation, ***u*** = the mean velocity, and ***D***= the depth of water. The boundary conditions of the rate of dissipation or epsilon were specified as follows: ***fixedValue*** at the inlet with the value of ***ε*** as calculated from the above equation, ***zeroGradient*** at the outlet and the atmosphere, and finally the wallFunction (***epsilonwallFunction***) has been used for the side and lower walls which provides a turbulence dissipation wall function condition for high Reynolds numbers in turbulent flow cases. In the case of using the solver pisoFoam instead of interFoam, the only difference is that the boundary condition of the atmosphere changes to be ***symmetryPlane*** instead of ***zeroGradient***.

- Turbulent viscosity:

  The boundary conditions of the turbulent viscosity have been chosen as a ***zeroGradient*** for the inlet, outlet, and atmosphere. One of the wallFunctions called (***nutWallFunction***) was chosen for the side and lower walls to determine the boundary condition of the turbulent viscosity with a zero uniform value. In the case of using the solver pisoFoam instead of interFoam, the only difference is that the boundary condition of the atmosphere changes to be ***symmetryPlane*** instead of ***zeroGradient***.

- Kinematic viscosity (SGS) for LES model:

  Same as the turbulent viscosity, all the boundary conditions were used as a ***zeroGradient*** except for the side and lower walls were also one of the wallFunctions was used called (***nutkWallFunction***) with a zero uniform value. In the case of using the solver pisoFoam instead of interFoam, the only difference is that the boundary condition of the atmosphere changes to be ***symmetryPlane*** instead of ***zeroGradient***.

- Reynolds stress (R) for LRR model:

  The boundary conditions for the Reynolds stress was determined as a ***fixedValue*** for the inlet with a zero uniform value, and ***zeroGradient*** for the outlet and the atmosphere, while the wallFunction (***kqRwallFunction)*** has been used for the side and lower walls with a zero uniform value. In the case of using the solver pisoFoam instead of interFoam, the only difference is that the boundary condition of the atmosphere changes to be ***symmetryPlane*** instead of ***zeroGradient***.

4.7. Results and Discussions

In order to understand the behaviour of the flow in channel bends, some turbulence models were studied in this research. An evaluation for each model will be done based on velocity parameters. The results of the velocities across dimensional channel width that obtained from these models will be compared with Rozovskii experimental data (Rozovskii 1961). In addition, three-dimensional velocity components will be studied to highlight the reasons behind the variation in these velocities. Finally, each model will be evaluated depending on the results obtained from simulation outputs to choose the best one for each case.

4.7.1. Free Surface Model

As mentioned previously, the Free Surface Model takes in consideration both the water and the air in the simulation of the channel. A horizontal section was taken on the depth (0.242m) from the top of the channel to examine the characteristics of water flow separately at channel curve. Thus, the total depth of the channel is ($D_t = 0.3\ m$), and the depth of flow after the steady state is ($D_f = 0.058\ m$), which is same as the depth of flow in the experiment (0.058m). Figures (4-4) through (4-7) below illustrate the distribution of the velocity and the depth of water for the channel at time zero and 300 seconds for standard *k*-ε, LRR, realizable

k-ε, and LES models.

For standard *k-ε* model shown in Figure 4.4, the initial condition of the simulation started with a depth of water equal to (0.01 m) as shown in part (a). At steady state, the depth of water reached approximately (0.058 m), which is the same depth of water in the experiment as shown in part (b). The velocity was calculated considering the air and depth of water (with a total depth of 0.3 m) as shown in parts (c) and (d) at time zero and 300 seconds at the steady state. Parts (e) and (f) demonstrate the velocity considering the depth of water only (0.058 m). The latter case was used in comparative analysis with experimental data.

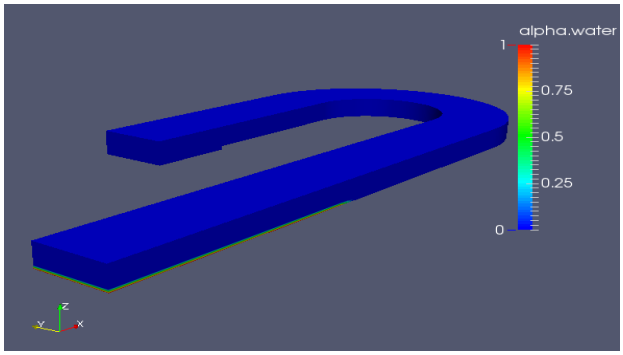

a- Alpha water at time=0 sec and D=0.3 m.

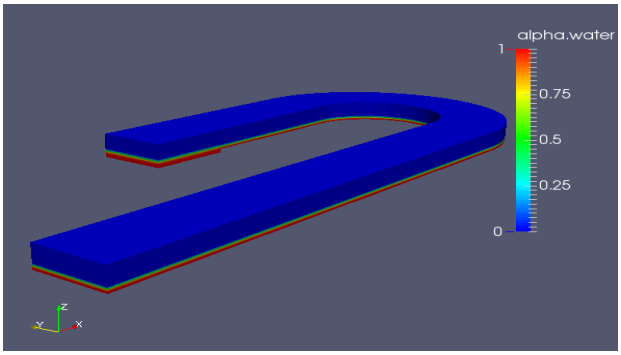

b- Alpha water at time=300 sec and D=0.3 m.

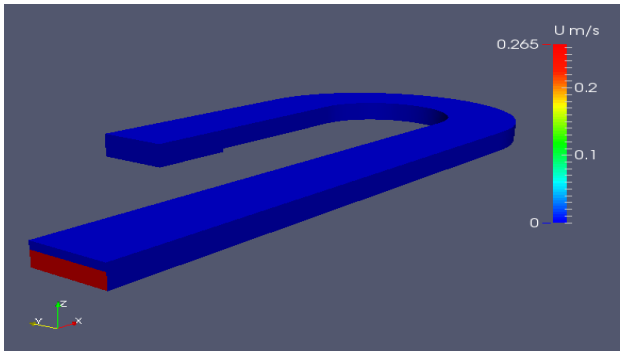

c- Velocity at time=0 sec and D=0.3 m.

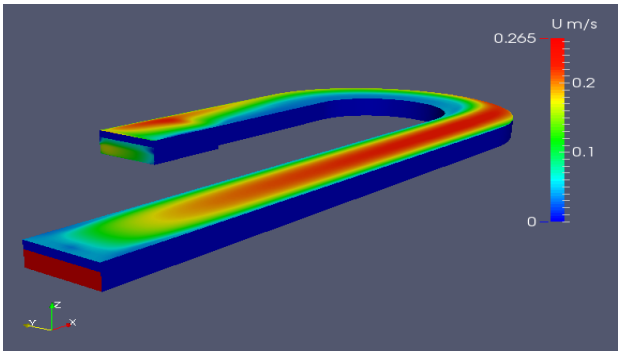

d- Velocity at time=300 sec and D=0.3 m.

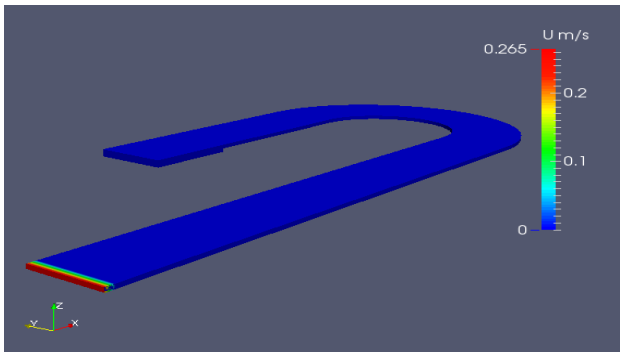

e- Velocity at time=0 sec and D=0.058 m.

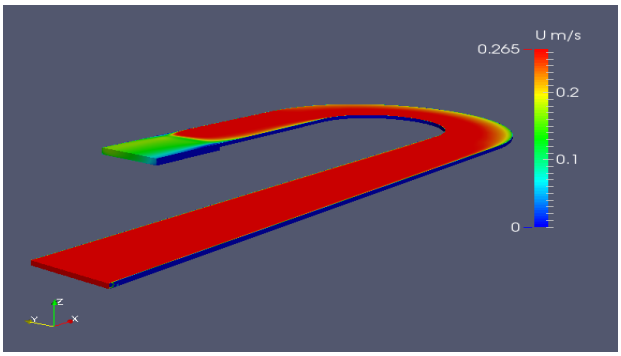

f- Velocity at time=300 sec and D=0.058 m.

Figure 4.4 : Standard *k-ε* model.

The flow velocity distribution in the standard *k-ε* model indicates that the maximum velocity tends to be near the inner bank at the beginning of the bend, and it turns gradually towards the outer bank near the bend exit.

Similar to the standard *k-ε* model, the initial condition of the depth of water for the LRR model is the same (0.01 m). The steady state was reached at time 300 seconds with a depth of water of (0.058 m) as shown in Figure 4.5. The velocity in this model increases in inner bank and

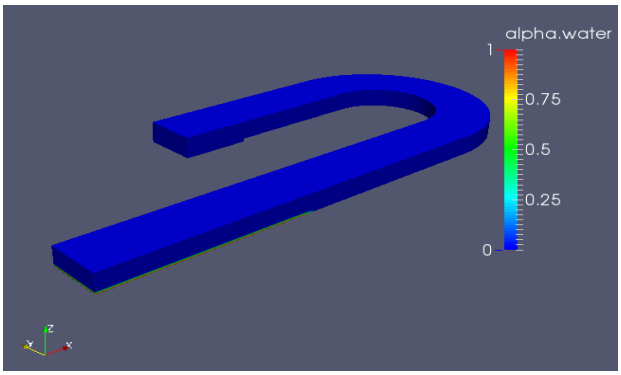

a- Alpha water at time=0 sec and D=0.3 m.

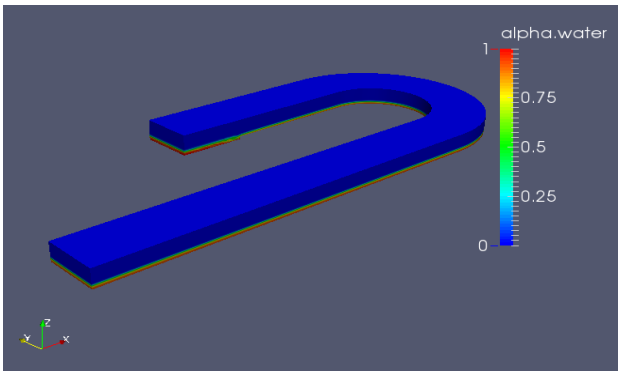

b- Alpha water at time=300 sec and D=0.3 m.

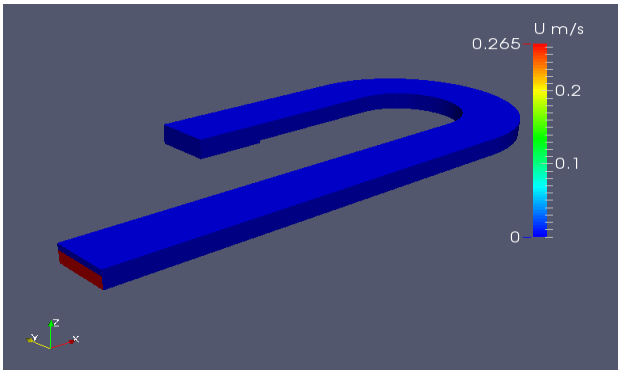

c- Velocity at time=0 sec and D=0.3 m.

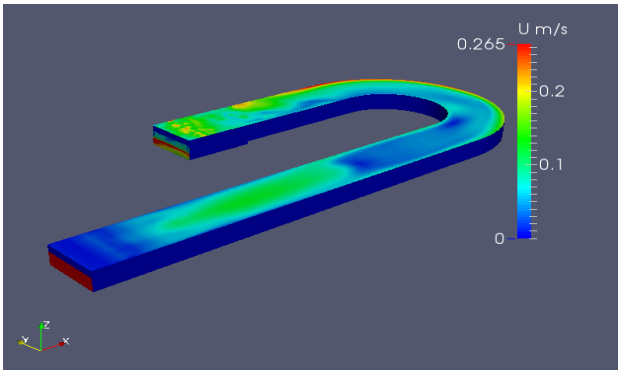

d- Velocity at time=300 sec and D=0.3 m.

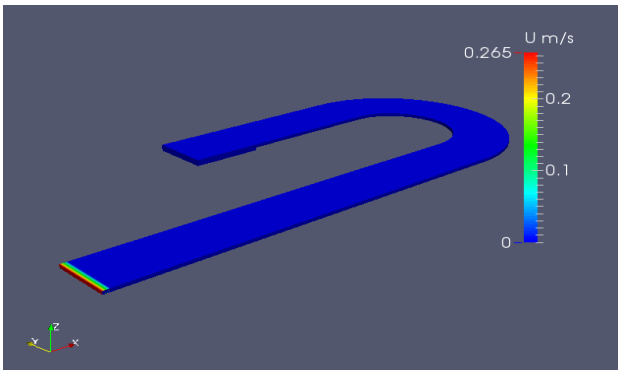

e- Velocity at time=0 sec and D=0.058 m.

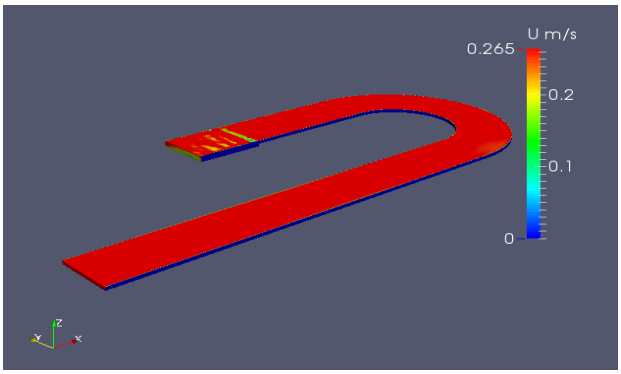

f- Velocity at time=300 sec and D=0.058 m.

Figure 4.5: LRR model.

decreases at the outer bank. The distribution of the velocity is shown in parts (d) and (f) of the figure.

The same initial conditions mentioned above were used for the realizable *k-ε* and LES models as well. The steady state was reached at time 300 seconds. The distribution of velocity at steady state for these models is the same as the previous models as shown in Figure 4.6 and Figure 4.7.

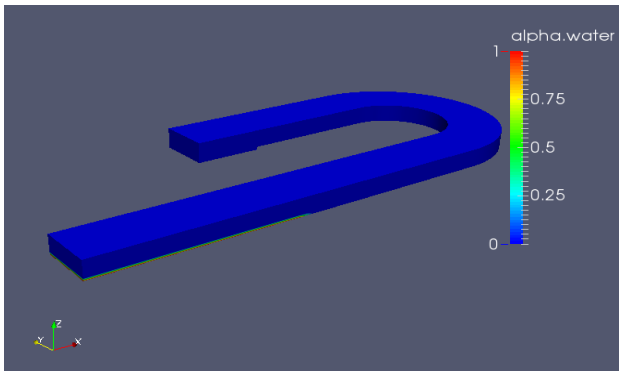

a- Alpha water at time=0 sec and D=0.3 m.

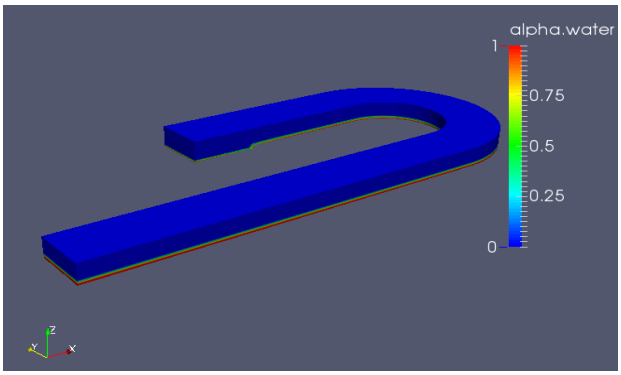

c- Alpha water at time=300 sec and D=0.3m.

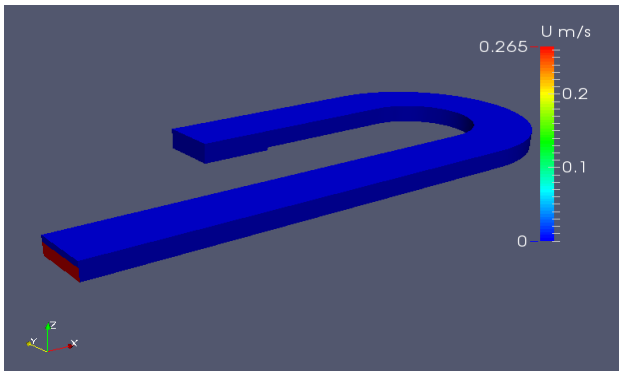

d- Velocity at time=0 sec and D=0.3 m.

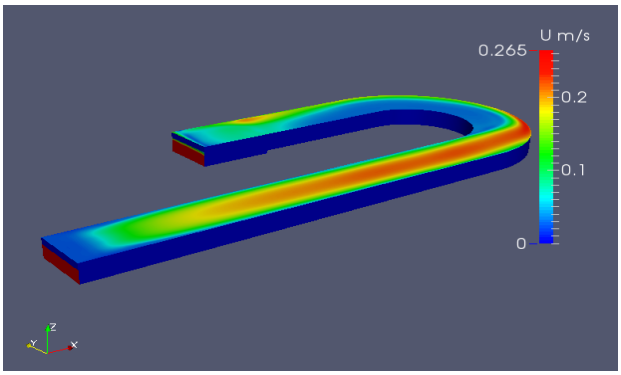

f- Velocity at time=300 sec and D=0.3 m.

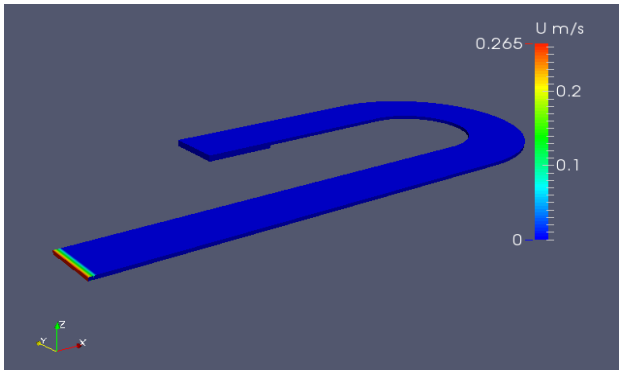

g- Velocity at time=0 sec and D=0.058 m.

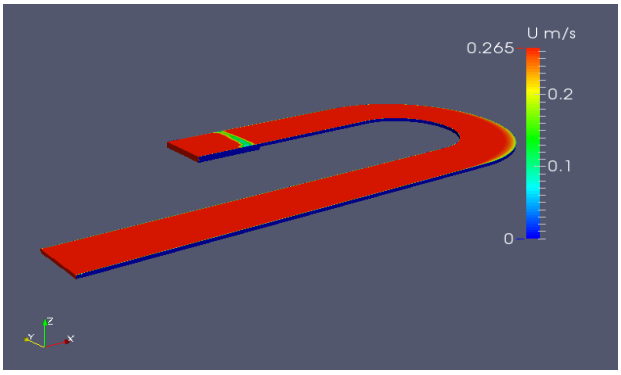

i- Velocity at time=300 sec and D=0.058 m.

Figure 4.6: Realizable *k-ε* model.

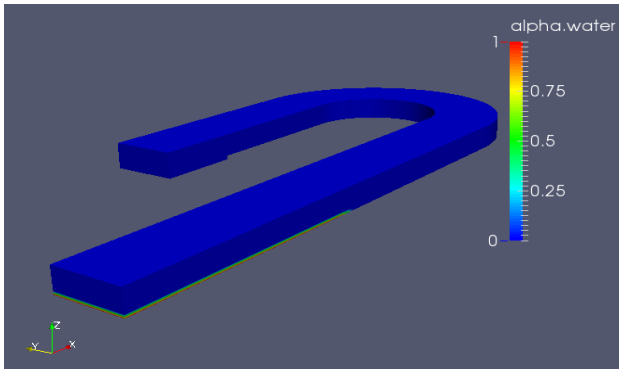

a- Alpha water at time=0 sec and D=0.3 m.

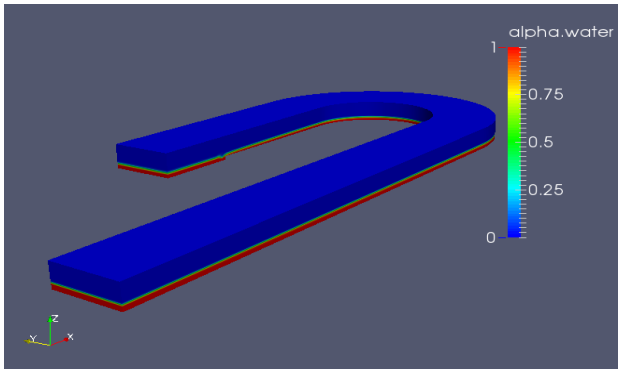

b- Alpha water at time=300 sec and D=0.3 m.

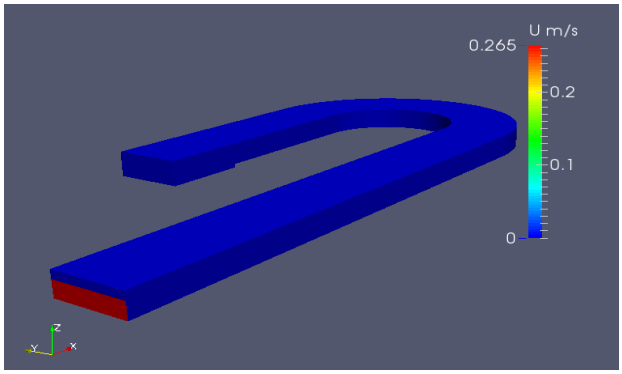

c- Velocity at time=0 sec and D=0.3 m.

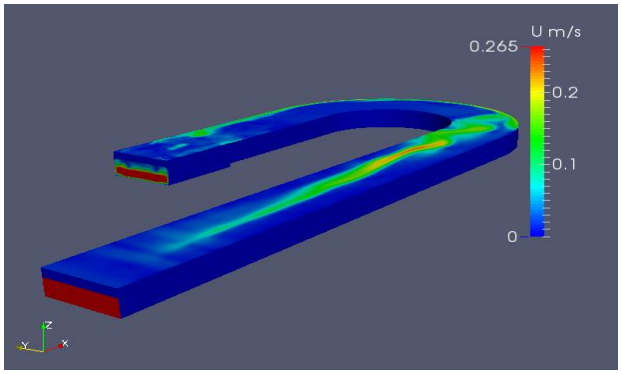

d- Velocity at time=300 sec and D=0.058 m.

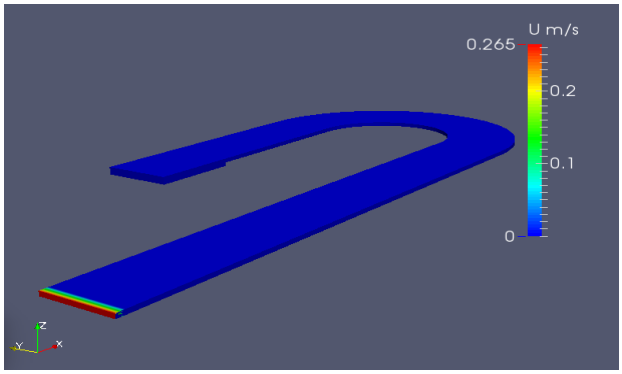

e- Velocity at time=0 sec and D=0.058 m.

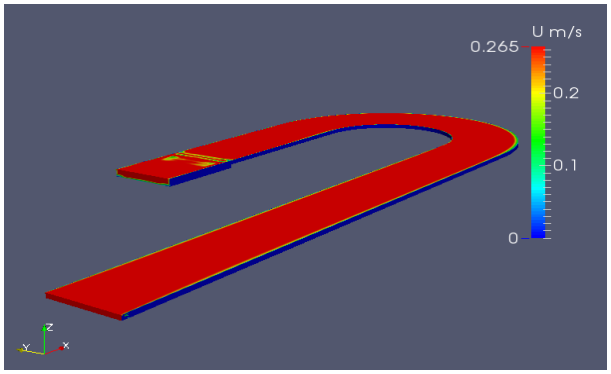

f- Velocity at time=300 sec and D=0.058 m.

Figure 4.7 : LES model.

Further examination for velocity distribution of the flow in channel bend was done by taking several sections along the bend. In the experiment, sections at (0°, 35°, 65°, 100°, 143°, and 186°) were taken in the bend as shown in Figure 4.8. The velocity distribution at these sections was addressed for all numerical models to compare the outputs of the simulations with the experiment data.

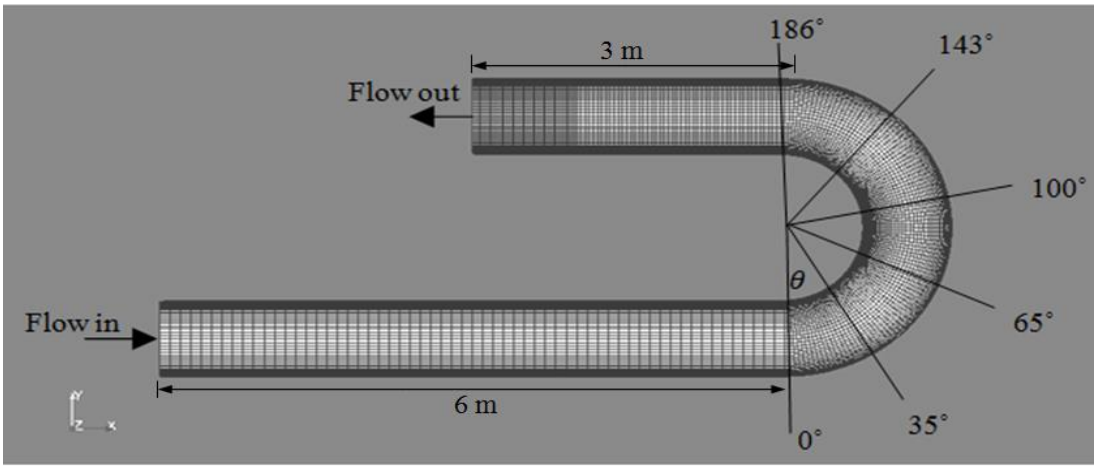

Figure 4.8 : Sections at the bend.

Figure 4.9 indicates the depth averaged velocity across the width of the channel. Velocity was calculated using Equation (4.1):

$$\boldsymbol{U} = \sqrt{\boldsymbol{u}^2 + \boldsymbol{v}^2 + \boldsymbol{w}^2} \qquad (4.1)$$

where;

$\boldsymbol{U}$ = the depth averaged velocity magnitude.

$\boldsymbol{u},\ \boldsymbol{v}, \boldsymbol{w} =$ Longitudinal, vertical, and lateral velocity averaged over depth.

Note that the vertical axis in the Figure 4.9 represents the depth averaged velocity, and is non-dimensionalized by $\boldsymbol{U}_{\infty}$, which is the downstream mean velocity. The horizontal axis represents the radial distance, non-dimensionalized by the channel width, $(\boldsymbol{r} - \boldsymbol{ri})/\boldsymbol{B}$ = the radial distance; where $\boldsymbol{B}$ is the channel width, $\boldsymbol{r}$ and $\boldsymbol{ri}$ are the radius of curvature for the outer and inner bank, respectively.

For the case of Free Surface Model as shown in Figure 4.9, the following points can be highlighted:

- The velocity of the flow for all the models approximately showed the same results; the velocity is increasing near the inner bank of the channel and decreasing towards the outer bank at sections (0˚, 35˚, 65˚, 100˚, and 143˚). However, the LRR model demonstrated different results at sections (65˚, 100˚, and 143˚).

- The sudden change in channel from straight to curvature giving rise to another changing in water level from horizontal to transverse slope, and this is the reason behind the velocity distribution in the two banks in addition to the effect of secondary flows.

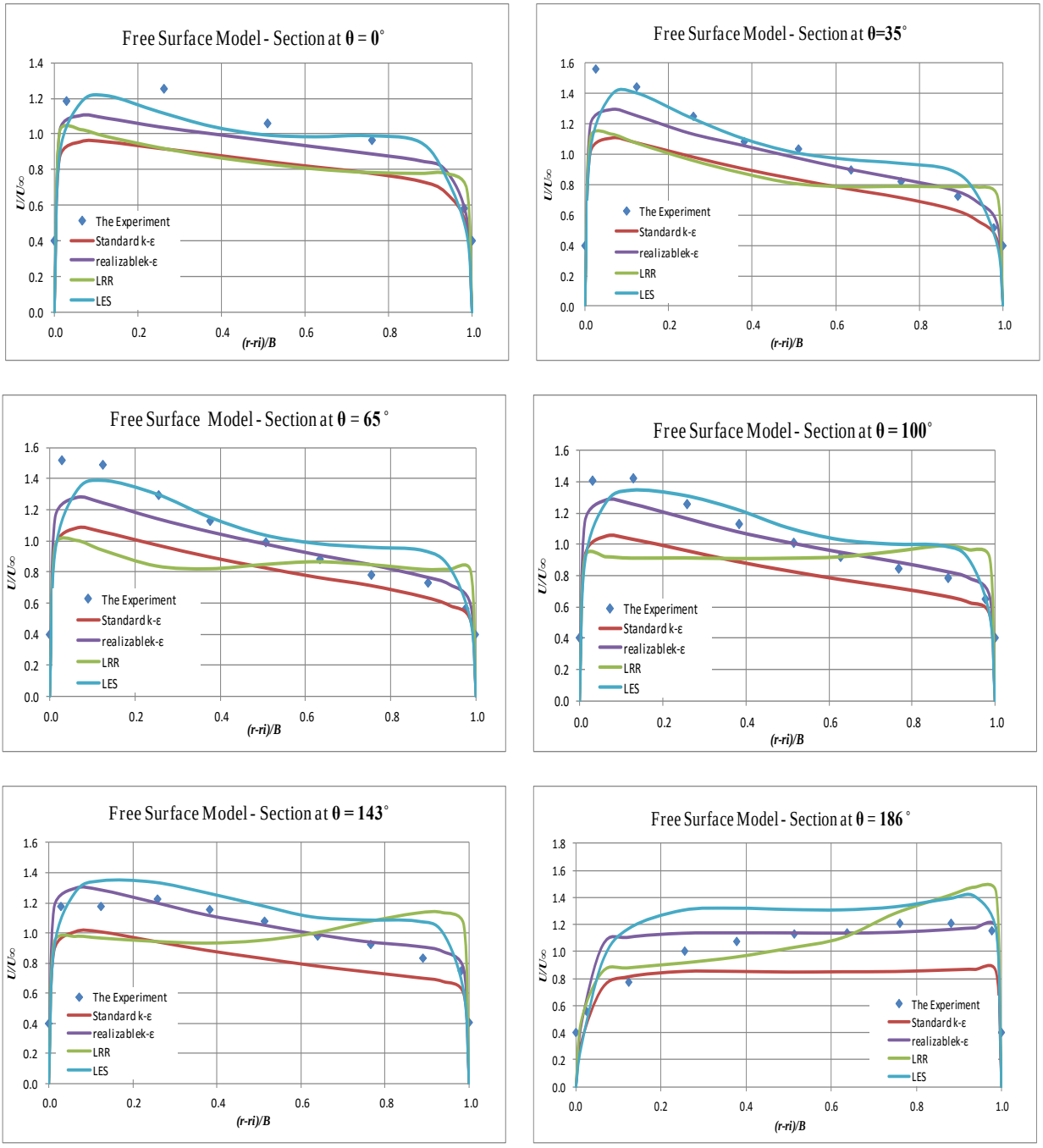

Figure 4.9: Depth averaged velocity along channel width for Free Surface Model.

- At the last section, 186˚ near the bend exit, the velocity decreases in the inner bank and increases towards the outer bank of the channel.
- There are some differences between the numerical models and the experimental data which could be attributed to some errors in the measurements of the flow, the secondary flow is underestimated in the numerical models, and the approximation might be used in the computation of the flow characteristics.
- The realizable *k*-*ε* and LES models have the best agreement with the experimental data for the velocity curve.

4.7.2. Rigid-Lid Model

Figure 4.10 shows the distribution of velocity at time zero and 100 seconds on the steady state for standard *k*-*ε*, realizable *k*-*ε*, and LRR models, respectively.

As the Free Surface Model, the Rigid Lid Model showed the same distribution of the velocity; the maximum velocity exists at the inner banks at the beginning of the bend and then turns gradually towards the outer banks near the bend exit.

The distribution of velocity of the flow at the sections mentioned earlier is shown in Figure 4.11.

For the case of Rigid-Lid Model, according to the figures above, the results of the four models showed the following:

- The flow velocity for the models approximately showed the same results which is increasing near the inner bank of the channel and decreasing towards the outer bank at sections (0˚, 35˚, 65˚, 100˚, 143˚) except for the LRR model which demonstrated a slight difference from other models at sections (0˚, 35˚, 65˚, 100˚, 143˚).
- Also, the velocity near the inner bank of the bend is underestimated specifically at the beginning of the bend and the reason behind that could be the sudden change in the channel from straight to curvature causing a changing in the water level.
- At the last section 186˚ near the bend exit, the velocity decreases in the inner bank and increases towards the outer bank of the channel.
- There are somewhat differences between the numerical models and the experimental data which attributed to the same reasons that mentioned previously in the Free

Surface Model.

- The best models that achieved a good agreement in the velocity curve with the experimental data are the standard *k*-*ε* and realizable *k*-*ε* models.

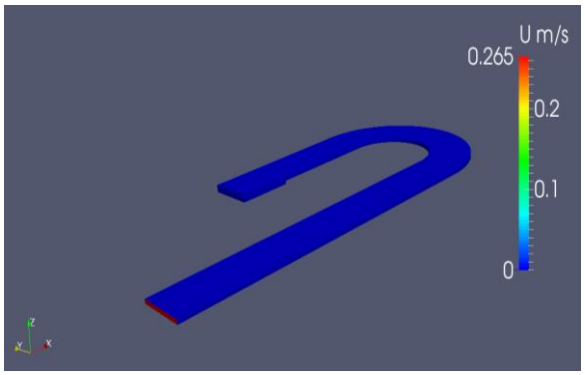

a- Velocity at time=0 sec and D=0.058 m.

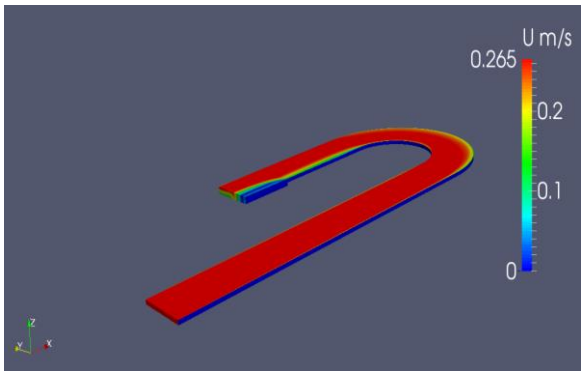

b- Velocity at time=100 sec and D=0.058 m.

Standard *k*-*ε* model.

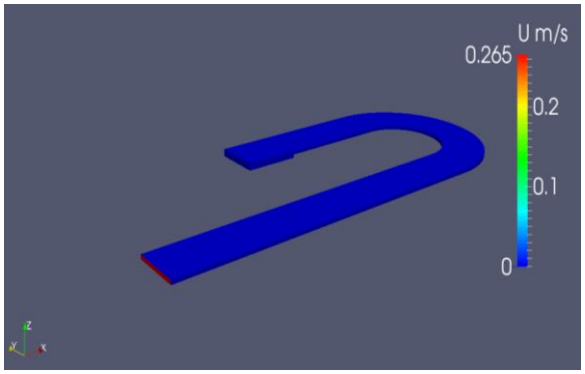

c- Velocity at time=0 sec and D=0.058 m.

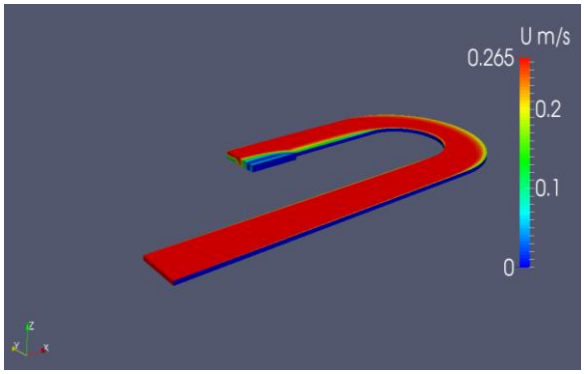

d- Velocity at time=100 sec and D=0.058 m.

Realizable *k*-*ε* model.

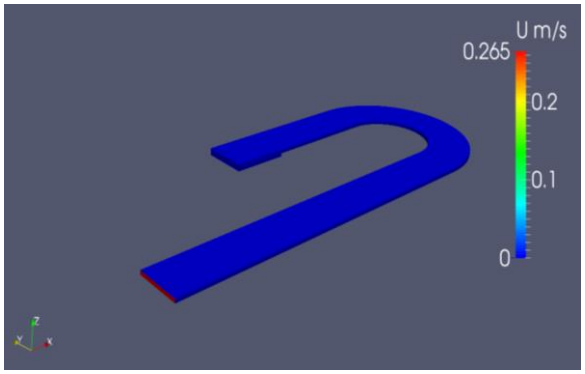

e- Velocity at time=0 sec and D=0.058 m.

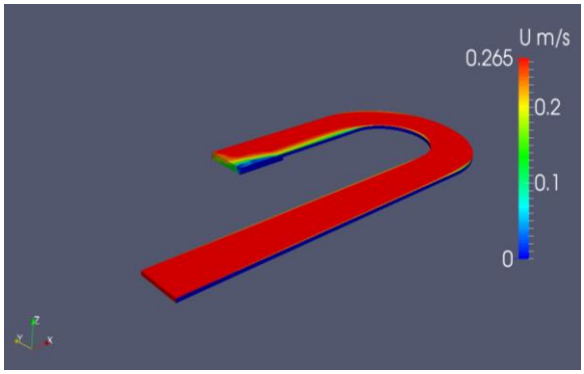

f- Velocity at time=100 sec and D=0.058 m.

LRR model.

Figure 4.10: Rigid Lid Models.

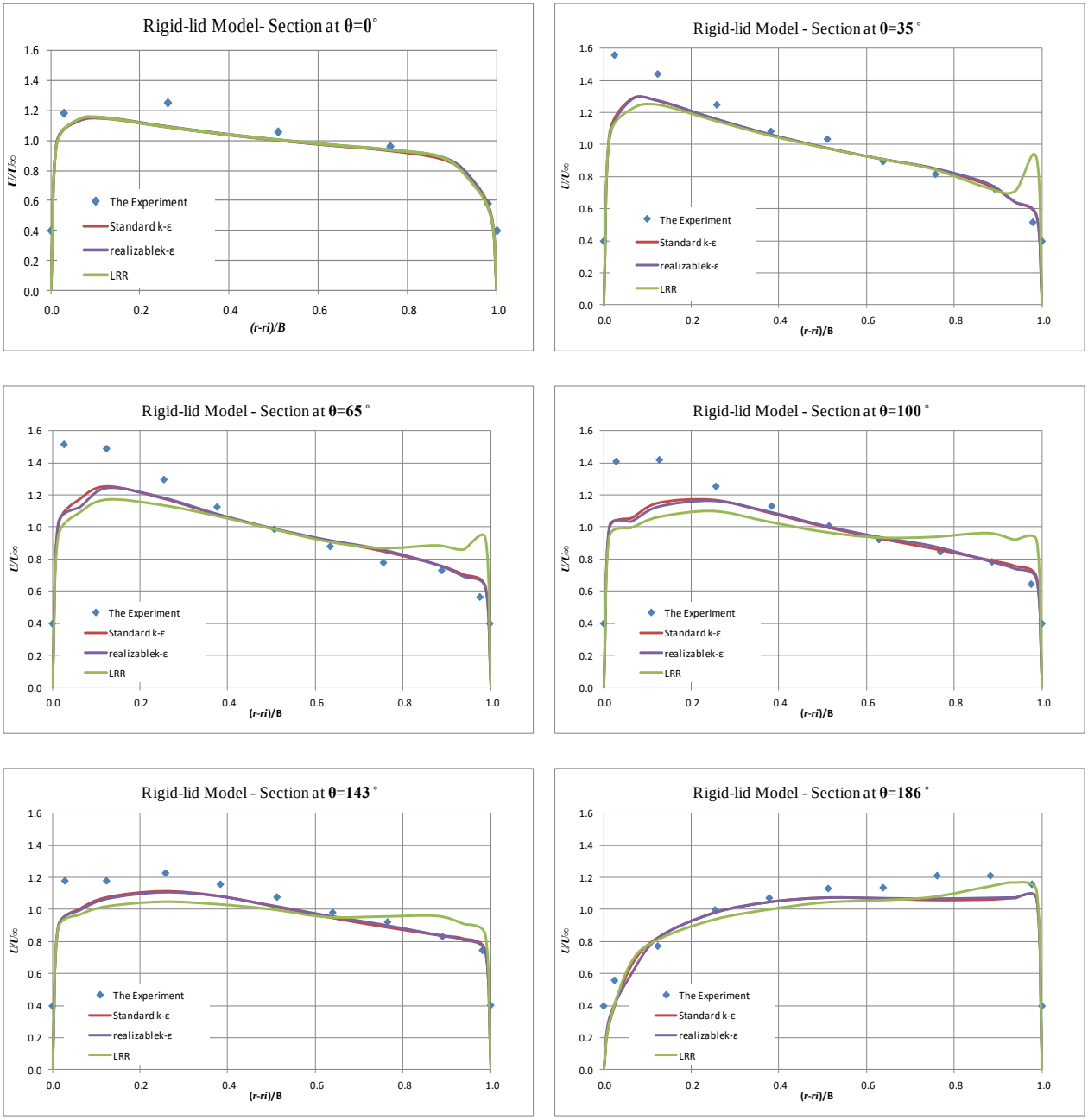

Figure 4.11: Depth averaged velocity along channel width for Rigid-Lid Model.

4.7.3. A Comparison with other Numerical Models

Some of the models that demonstrated a good agreement with the experimental data have been chosen here to make a comparison with other numerical models. The first model is realizable *k-ε* of the Free Surface Model and it is named in the figures below as realizable *k-ε* (FSM). The second model is LES model and it is named in the figures below as (LES). The last model

is realizable *k-ε* of the Rigid-Lid Model and it is named in the figures below as realizable *k-ε* (RLM). Four numerical models were selected to compare the new employed models with, they are Yeh and Kennedy (1993) numerical model, Lien et al. (1999) Numerical model (Lien et al., 1999), Johannesson (1988) numerical model, and Song et al. Numerical model (Song et al., 2012a). The results are shown in Figure 4.12.

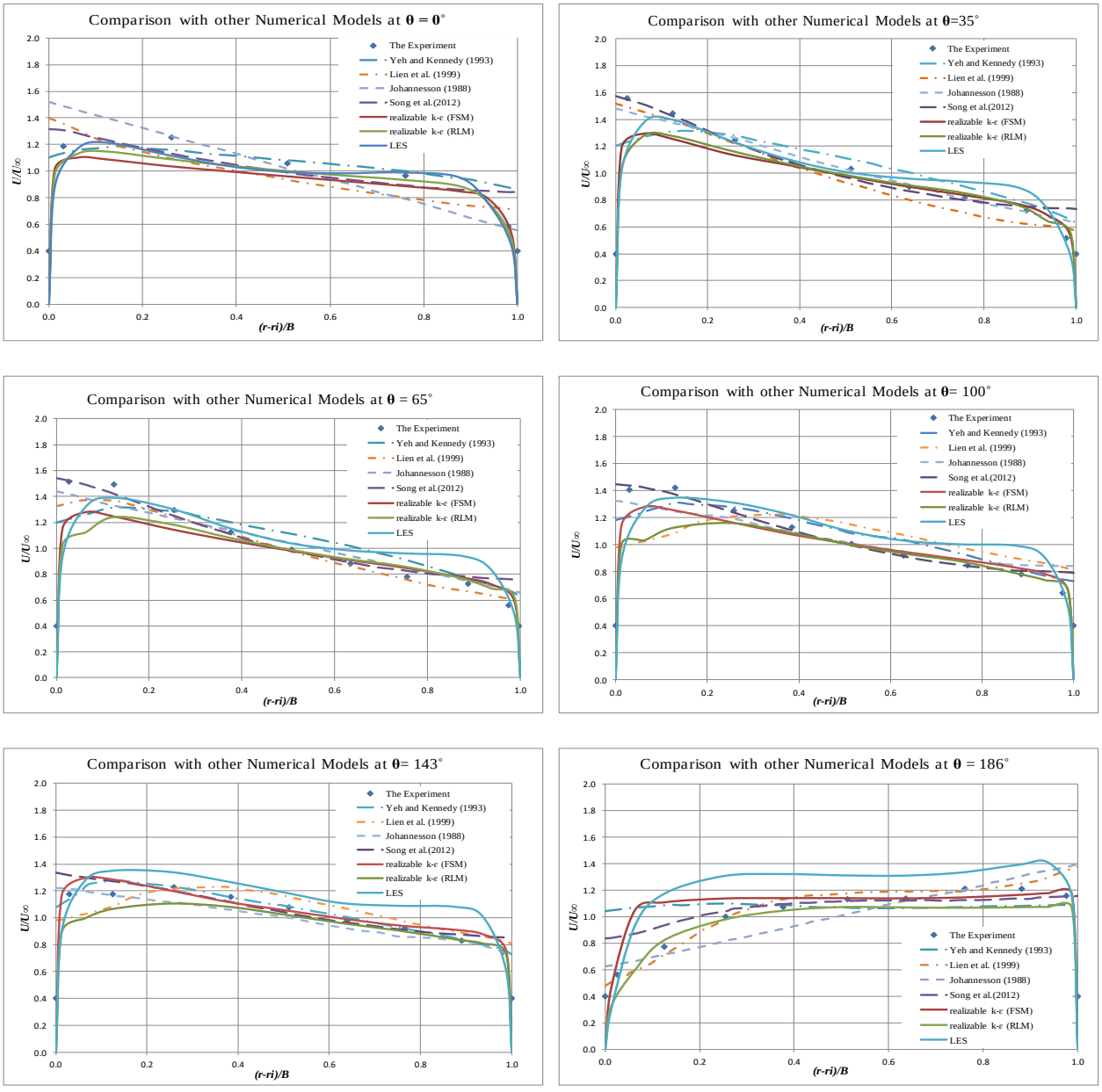

Figure 4.12: A comparison with other numerical models.

According to the comparison with the other numerical models, all the three employed models have shown a good compatibility with other numerical models with some slight variations particularly at the inner bank of the channel. However, the best employed model is realizable *k-ε* of the Free Surface Model for the sections (0˚, 35˚, 65˚, 100˚, 143˚), while for the last section (186˚) near the bend exit the employed model realizable *k-ε* of the Rigid-Lid Model was the best.

4.8. The Divergences in Velocity Distribution

The components of the velocity which include the longitudinal, vertical, and lateral velocities are affected by the secondary flows upon the entry of the flow to the bend. In order to examine the distribution of these velocities along the depth of the channel, sections have been taken at (0˚, 90˚, 180˚) from the channel bend. The model that was chosen to study these velocities for both of the Free Surface Model case and Rigid-Lid Model case is realizable *k-ε* model since it is the model that achieved the best agreement compared with the experimental data.

4.8.1. Longitudinal Velocity Distribution

The longitudinal velocity or streamwise velocity is the velocity in the direction of the flow which is (x- direction) of the domain in this case. Figure 4.13 illustrates the contour lines of the longitudinal velocity and the variation in the velocity at the beginning of the bend (section 0˚), the middle (section 90˚), and the bend exit (section 180˚). The axes that are shown in the figures represent the following:

X-Axis: The width of the channel in y- direction.

Y-Axis: The width of the channel in x- direction.

Z-Axis: The depth of the channel.

The distribution of the longitudinal velocity could be explained as follows:

- For the case of Free Surface Model, the maximum velocity moves towards the inner bank at the beginning of the bend, and this is mainly because of the longitudinal pressure gradients that exist close to the inner bank in sharp curve channel. The longitudinal pressure gradients appear due to the changing in the channel from straight to curved causing the same change in the flow. Thereafter, the longitudinal velocity reaches to the maximum value at the middle of the bend affected by the secondary

flow. Then, the longitudinal velocity decreases gradually towards the bend exit.

- For the case of Rigid-Lid Model, also the maximum longitudinal velocity occurs near the inner bank at the entrance of the bend, and then decreases gradually towards the bend exit. The maximum value of the longitudinal velocity in this case occurs at the beginning of the bend.
- For both of the two cases, the helical path of the secondary flow exists but it is not clear enough in the sections of the small water depth (0.058 m).

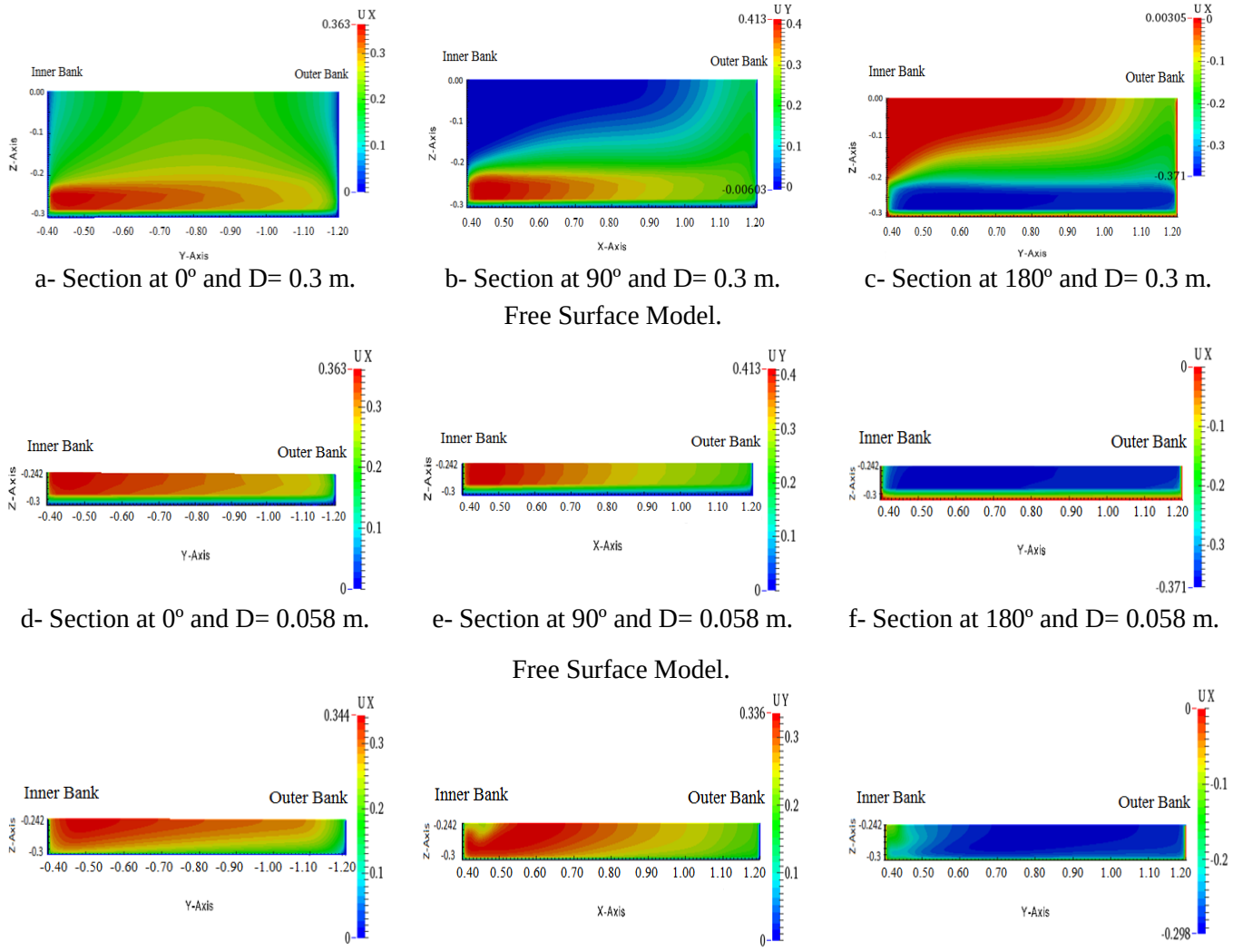

a- Section at 0º and D= 0.3 m. b- Section at 90º and D= 0.3 m. c- Section at 180º and D= 0.3 m.

Free Surface Model.

d- Section at 0º and D= 0.058 m. e- Section at 90º and D= 0.058 m. f- Section at 180º and D= 0.058 m.

Free Surface Model.

g- Section at 0º and D= 0.058 m. h- Section at 90º and D= 0.058 m. i- Section at 180º and D=0.058 m.

Rigid-Lid Model.

Figure 4.13: Longitudinal velocity distribution.

4.8.2. Vertical Velocity Distribution

The vertical velocity or cross-stream velocity is the velocity in the (y- direction) of the domain which is perpendicular to the flow in this case. Figure 4.14 below illustrate the contour lines of the vertical velocity at different sections starting from the entrance of the bend (section 0˚), the centre (section 90˚), and end of the bend (section 180˚). The axes that are shown in the figures are the same as those mentioned in section (4.8.1).

The changes in the vertical velocity distribution could be described as below:

- For the case of Free Surface Model, maximum velocity occurs near the centre of the channel at the beginning of the bend and then decreases towards the middle of the bend. At section 180-degree of the bend, the maximum velocity tends to be near the inner bank of the bend and it reaches its maximum value at this section. Also, there is a negative velocity close to the channel bed and positive velocities near the water surface which indicate the existence of the secondary flow.
- For the case of Rigid-Lid Model, the maximum velocity tends to be near the centre of the channel at the beginning of the bend and then turns towards the outer bank. Also, it is starting from the channel bed moving gradually towards the water surface near the bend exit. The maximum value of the vertical velocity in this case occurs at the bend exit as shown in the figure.
- At the middle of the bend and near the channel exit, the velocity is negative near the channel bed and positive near the water surface which indicates the existence of secondary flows.

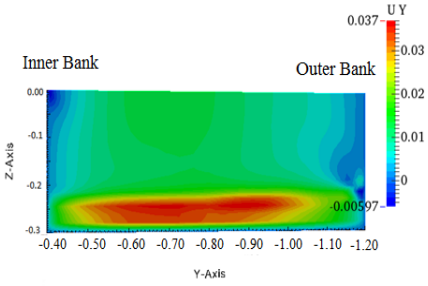

a- Section at 0º and D= 0.3 m.

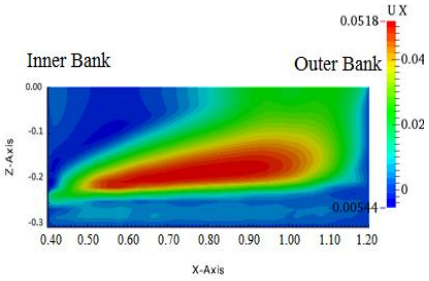

b- Section at 90º and D= 0.3 m.

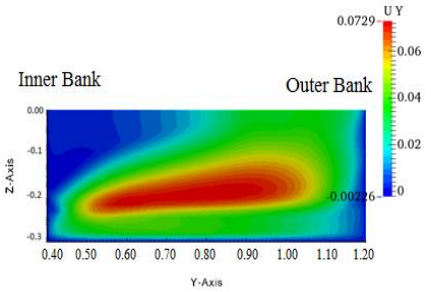

c- Section at 180º and D= 0.3 m.

Free Surface Model.

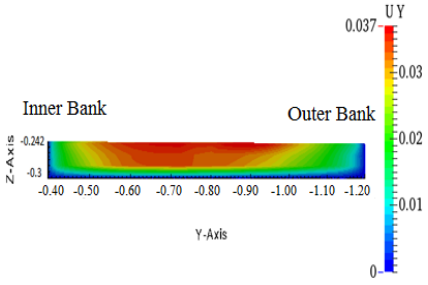

d- Section at 0º and D= 0.058 m.

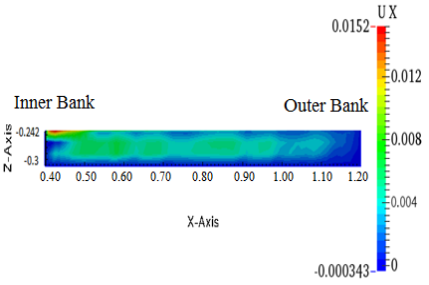

e- Section at 90º and D= 0.058 m.

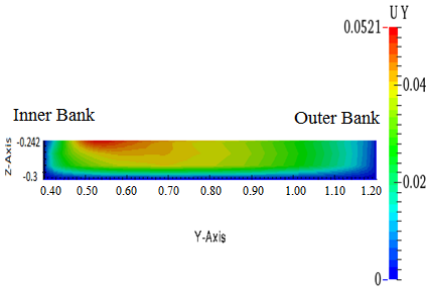

f- Section at 180º and D= 0.058m.

Free Surface Model.

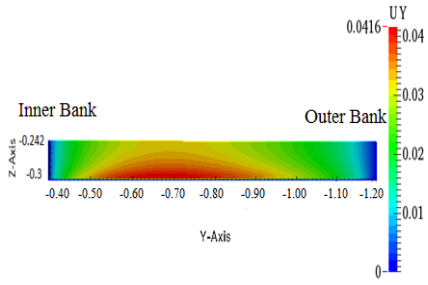

g- Section at 0º and D= 0.058 m.

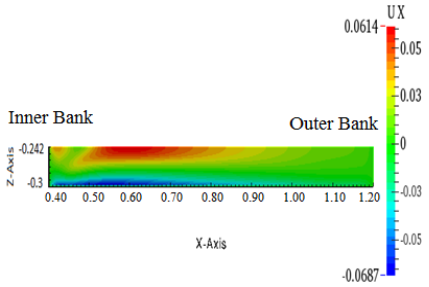

h- Section at 90º and D= 0.058 m.

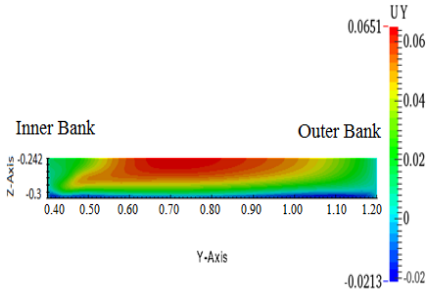

i- Section at 180º and D= 0.058 m.

Rigid-Lid Model.

Figure 4.14: Vertical velocity distribution.

4.8.3. Lateral Velocity Distribution

The lateral velocity or transversal velocity is the velocity in the (z- direction) of the domain in this case. The contour lines of the lateral velocity at different sections are shown in Figure 4.15, starting from the entrance of the bend (section 0˚), the centre (section 90˚), and end of the bend (section 180˚). The axes that are shown in the figures are the same as those mentioned in (4.8.1).

The lateral velocity distribution could be interpreted as follows:

- For the case of Free Surface Model, the value of lateral velocity at the beginning of

the bend is very small because of the strong longitudinal pressure gradients at this area. Then, the lateral velocity increases towards the middle of the bend and the bend exit as well. It reaches to the maximum value at the bend exit.

- For the case of Rigid-Lid Model, the maximum lateral velocity occurs near the inner bank at the beginning of the bend and increases to reach its maximum value at the bend centre, and then it decreases towards the bend exit.
- For both of the two cases, there are positive and negative velocities that indicate the secondary flow existence.

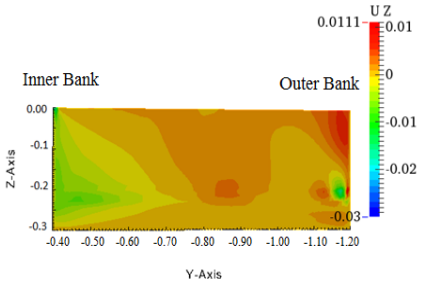

a- Section at 0º and D= 0.3 m.

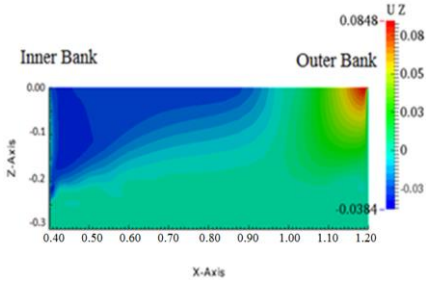

b- Section at 90º and D= 0.3 m. Free Surface Model.

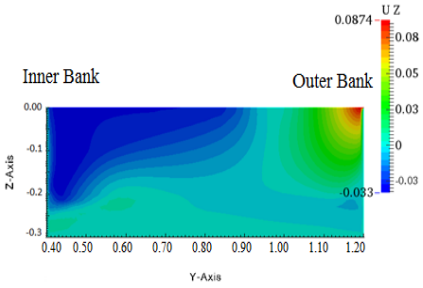

c- Section at 180º and D= 0.3 m.

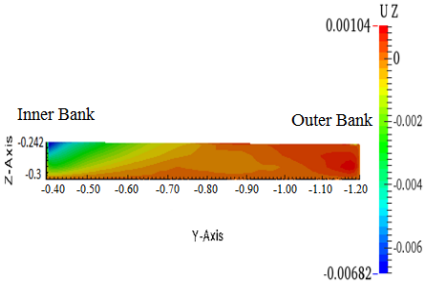

d- Section at 0º and D= 0.058 m.

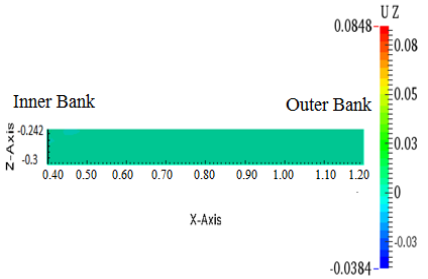

e- Section at 90º and D= 0.058 m. Free Surface Model.

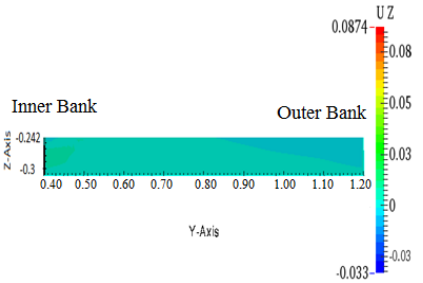

f- Section at 180º and D= 0.058 m.

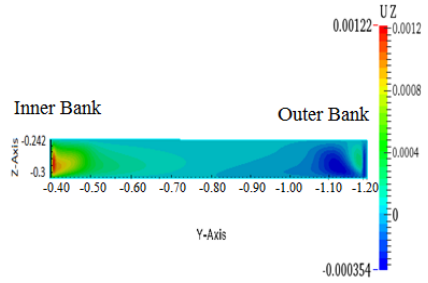

g- Section at 0º and D= 0.058 m.

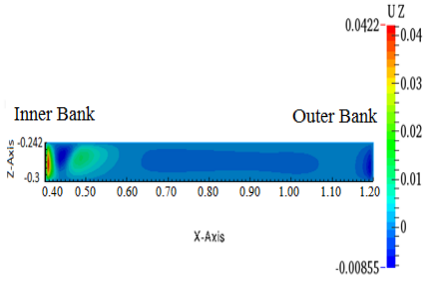

h- Section at 90º and D= 0.058 m. Rigid-Lid Model.

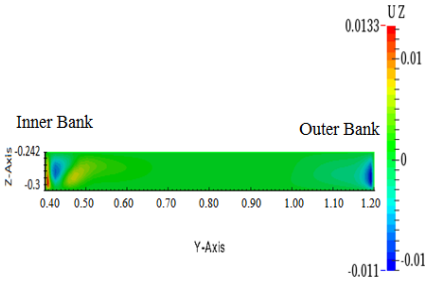

i- Section at 18 0º and D= 0.058 m.

Figure 4.15: Lateral velocity distribution.

4.8.4. The Distribution of Flow Velocity along the Bend

Figure 4.16 indicates the longitudinal and vertical velocity along the bend at sections near the water surface and for both of the two cases: Free Surface Model, and Rigid-Lid Model. The distribution of the velocity is discussed below:

- The longitudinal velocity for the two cases as shown in the figures is approximately the same in terms of the increasing at the beginning of the bend due to the high pressure gradients at this area, and decreasing near the bend exit. The difference between the two cases is the maximum value of the longitudinal velocity which is larger in the Free Surface Model case.

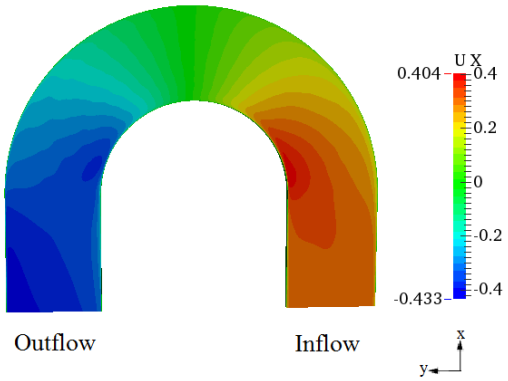

a- Longitudinal velocity for Free Surface Model.

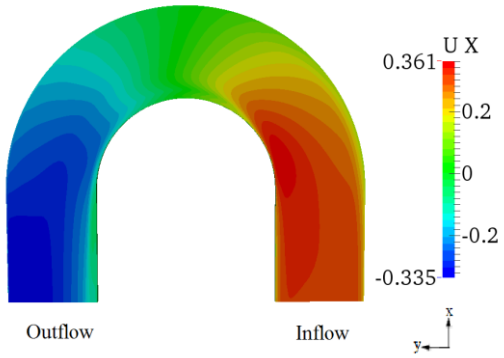

b- Longitudinal velocity for Rigid-Lid Model.

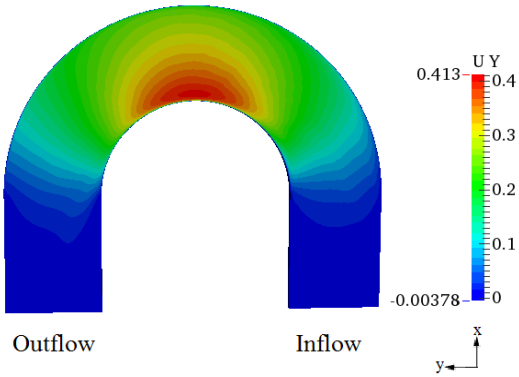

c- Vertical velocity for Free Surface Model.

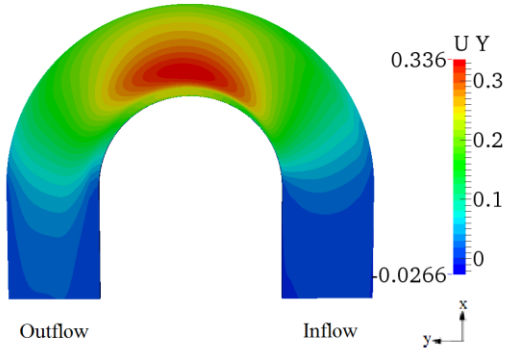

d- Vertical velocity for Rigid-Lid Model.

Figure 4.16: The distribution of flow velocity along the bend.

- The vertical velocity of the two cases is also approximately the same as clarified in the figures. It reaches its maximum value at the bend centre which indicates that the secondary flow reaches its maximum value also at this area. The difference between the two cases is the maximum value of the vertical velocity which is larger in the Free Surface Model case.

Part Two: Confluent Channel:

4.9. Experimental Setup

The open channel confluence flow experiment of Shumate (1998) was used to apply the model of the confluent channel. In this experiment, a branch channel conjugates with a main channel at 90° angle as shown in Figure 4.17. The velocities and water depth were measured in this experiment by using Acoustic Doppler velocimeter and a point gauge.

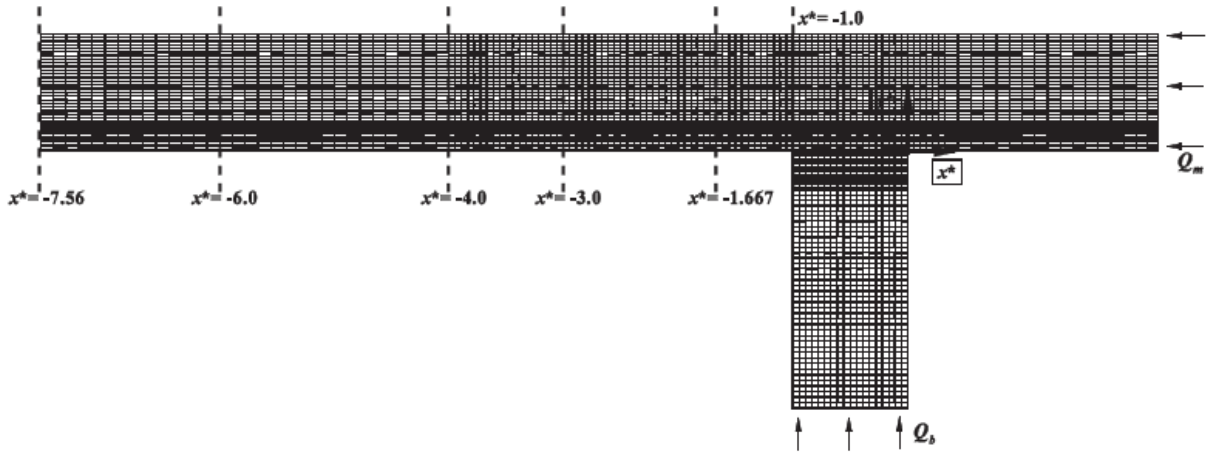

Figure 4.17: Shumate experimental data (Song et al., 2012).

The information of the channel and flow parameters are shown in Table 4-2.

Table 4-2 : The dimensions of confluent channel and flow conditions (developed from Shumate)

Variable	Symbol	Value
Main channel discharge	Q_m	0.043 m^3/s
Branch channel discharge	Q_b	0.127 m^3/s
Downstream water depth	h	0.296 m
Channel width	B	0.914 m
Che'zy factor	C	60
Mean velocity at downstream	U_∞	0.628 m/s
Tailwater Froude number	Fr_d	0.37

4.10. Computational Domain and Mesh Generation

The experimental data of Shumate was used to determine the computational domain dimensions. It includes a junction of two channels; the branch channel with a length of 3 m and denoted by (b), and the main channel with a length of about 10 m and denoted by (m). The width of the two channels is (0.914m) and the entire channel was set on a horizontal bed. Some changes were made on the computational domain. The length of the main channel was increased by (4 m) at the end. Also, a drop in (0.2m) depth was added at the end of the main channel in order to control the water depth in the channel. Two different channel depths were used; (0.4 m) in depth for the case of open channel flow (Free Surface Model), and (0.296 m) in depth for the case of closed channel flow (Rigid-Lid Model) as shown in Figure 4.18.

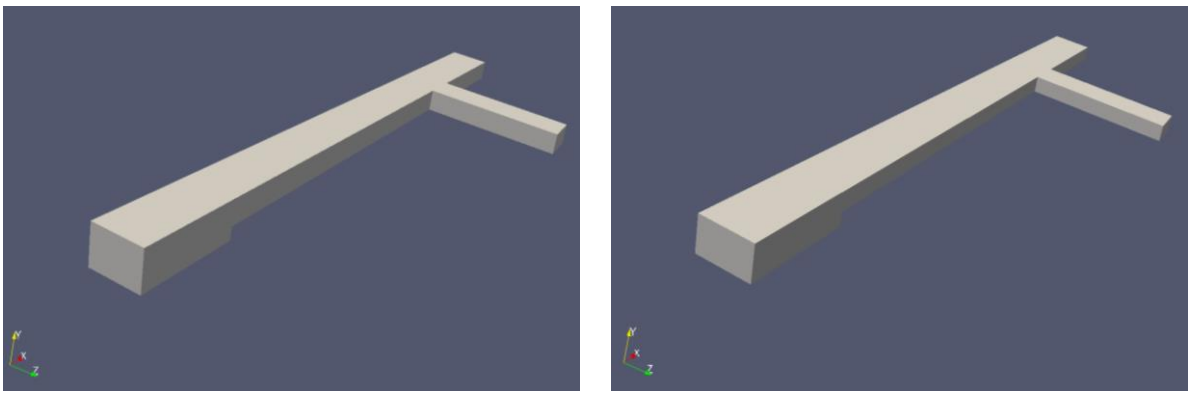

a- Free Surface Model. b- Rigid-Lid Model.

Figure 4.18 : The computational domain for confluent channel.

Generating the domain mesh is considered one of the important tasks in the computation of the numerical models in OpenFOAM. The grading of the mesh is desired to be optimal and appropriate in order to get more accurate results. In the case of confluent channel, a refined mesh is used for all simulations as shown in the Figure 4.19. The mesh at the area immediately after the junction is finer than the other areas of the channel since it is the main area of the study. Also, the mesh near the two banks of the channel is finer than that in the centre in order to get more accurate results from the two banks towards the centre of the channel. Finally, same mesh configuration was used for both cases of open channel flow and closed channel flow taking in consideration the changes in the domain.

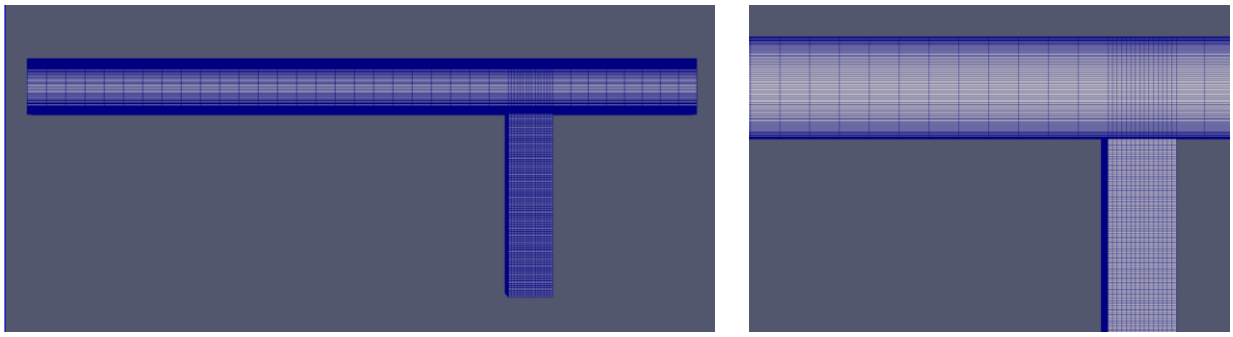

a- The mesh of the channel. b- The mesh of the junction.

Figure 4.19: The mesh of the confluent channel.

4.11. Turbulence Models

As mentioned previously in section (4.4) of curved channel in the above, four turbulence models were used in the case of confluent channel as below:

RAS turbulence models

- *kEpsilon*: Standard *k-ε* model
- *realizableKE*: Realizable *k-ε* model
- *LRR*: Launder-Reece-Rodi RSTM

LES turbulence model

- *oneEqEddy*: *k* -equation eddy-viscosity model

4.12. The Numerical Simulations

As mentioned in Section (4.5) of curved channel, OpenFOAM was used in the simulation of this study.

4.13. Initial and Boundary Conditions

The initial and boundary conditions used in the confluent channel are the same as those mentioned in Section (4.6), which was used in the curved channel.

4.14. Results and Discussions

Due to the complexity of flow features in river confluences and its importance in river engineering, several studies were reviewed to better understand these features. In this study, the velocity parameters were used to evaluate the models because of its capability on visualizing the flow characteristics. The results of the velocities across dimensional channel width that obtained from the different models were compared with Shumate experimental data (1998). Also, the components of the velocity in three dimensions were studied, and reasons behind the difference in each velocity were examined. Finally, the best model for each case was selected after evaluating the results of each model.

4.14.1. Free Surface Model

In this case of open channel flow, the flow features in the confluences were studied for the water flow separately without the effects of the air. To achieve that, a horizontal section was taken on depth of (0.104 m) from the top of the channel. Consequently, the total depth of the channel is ($D_t = 0.4$ m) and the depth of water after the steady state is ($D_f = 0.296$m), which are the same depths in Shumate experiment.

For all models (standard *k*-ε, LRR, realizable *k*-ε, and LES models), the depth of water at time zero was (0.096 m), and approximately (0.296 m) at the steady state as shown in figures 4-20 to 4-23. Noting that the calculated velocity considering the air and depth of water is shown in parts (c) and (d), while parts (e) and (f) consider the depth of water only. The latter case was adopted in this research.

The velocity distribution of the four models could be discussed as following:

- Standard ***k-ε*** model: the maximum velocity moves from the branch channel towards the outer bank of the main channel in the case of total depth of the channel ($D_t = 0.4\,m$), which means that the flow is affected by the air and the water. Then, it stabilizes gradually at the middle of the channel in the direction of the downstream. In the case of total depth of the channel considering only the water ($D_t = 0.296\,m$), the maximum velocity approximately moves in the same direction that mentioned in the above. However, the total area of maximum velocity along the width of the channel

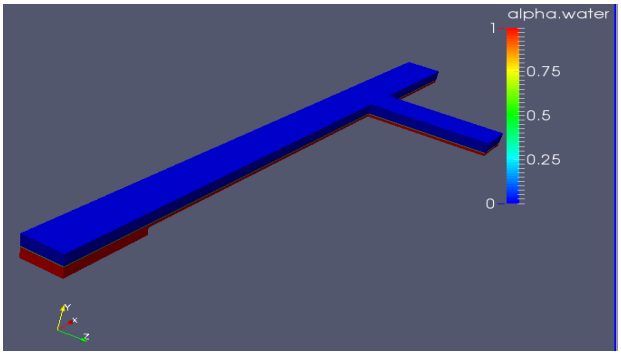

a- Alpha water at time=0 sec and D=0.4 m.

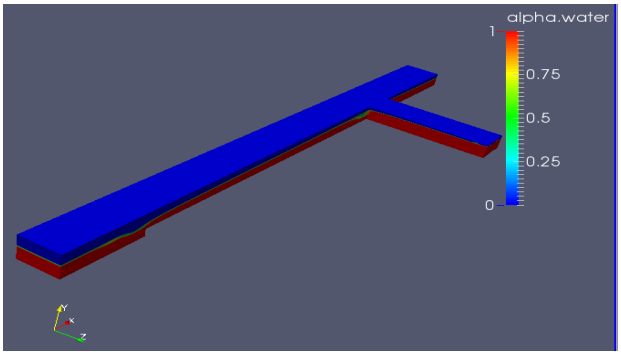

b- Alpha water at time=300 sec and D=0.4 m.

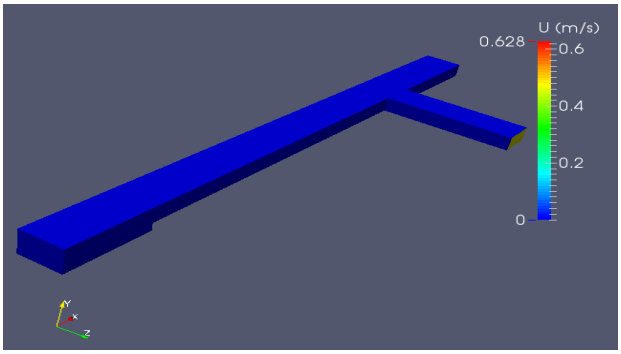

c- Velocity at time=0 sec and D=0.4 m.

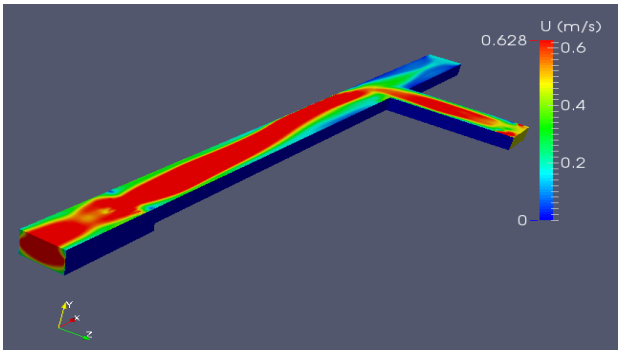

d- Velocity at time=300 sec and D=0.4 m.

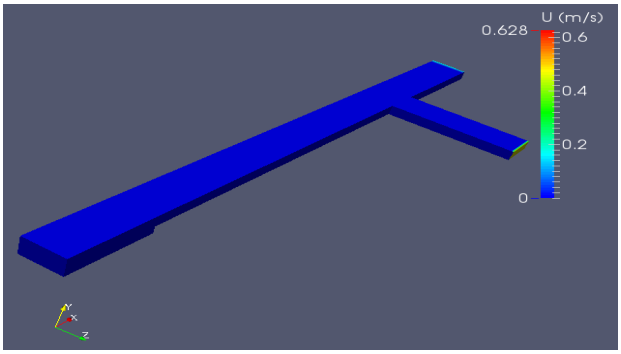

e- Velocity at time=0 sec and D=0.296 m.

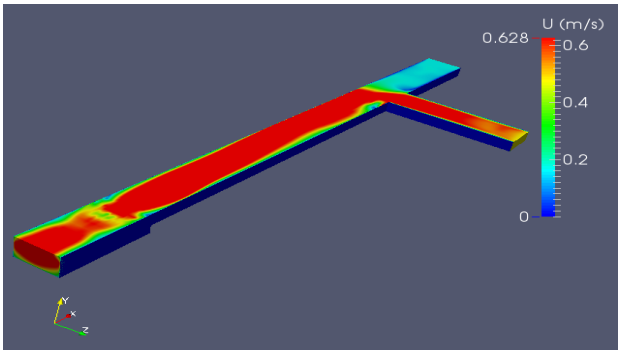

f- Velocity at time=300 sec and D=0.296 m.

Figure 4.20 : Standard *k-ε* model.

when considering only the water is larger than when considering the air and water together as shown in Figure 4.20.

- LRR model: the flow features in this model are difficult to capture. The maximum velocity for both cases (air and water and only water depth) is approximately spread along the entire width of the channel and almost there is no specific area for it as shown in Figure 4.21.

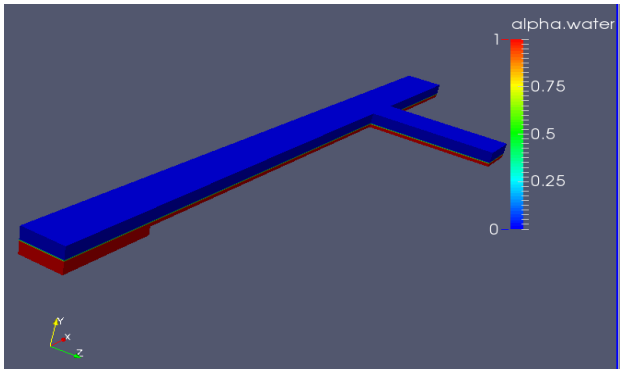

a- Alpha water at time=0 sec and D=0.4 m.

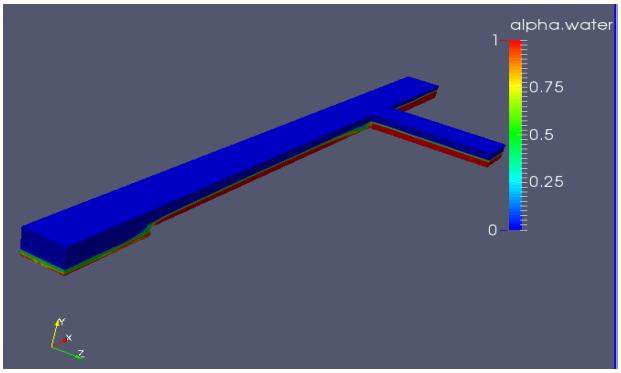

b- Alpha water at time=300 sec and D=0.4 m.

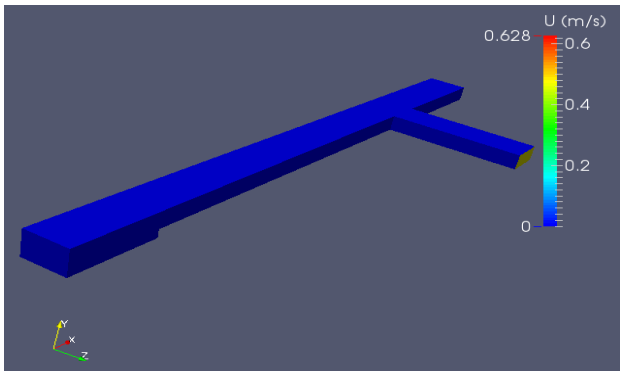

c- Velocity at time=0 sec and D=0.4 m.

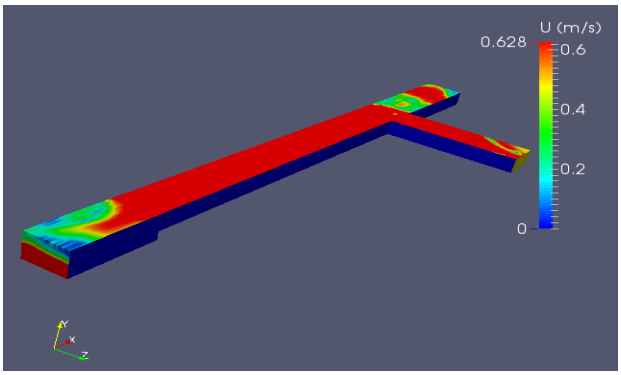

d- Velocity at time=300 sec and D=0.4 m.

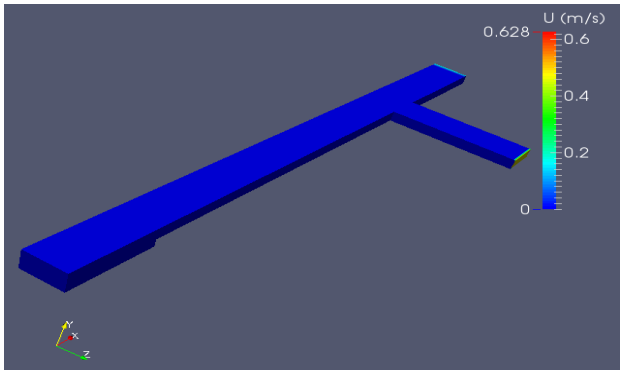

e- Velocity at time=0 sec and D=0.296 m.

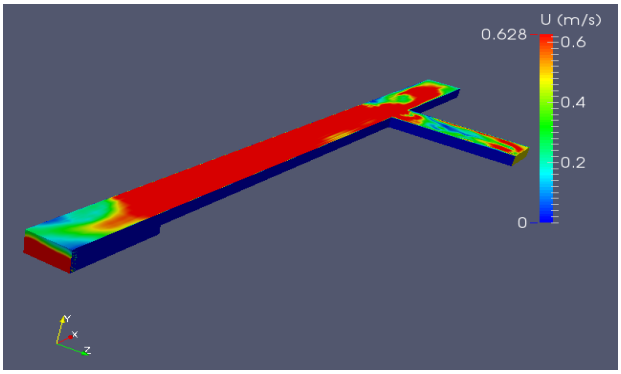

f- Velocity at time=300 sec and D=0.296 m.

Figure 4.21 : LRR model.

- Realizable ***k-ε*** model: the maximum velocity in this model moves approximately in the same direction that mentioned in standard *k-ε* model. It increases towards the outer bank of the main channel after departing the branch channel for both depth cases (air and water and only water depth) as shown in Figure 4.22.

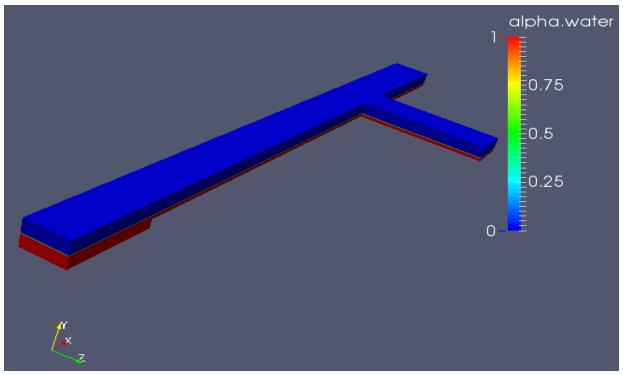

a- Alpha water at time=0 sec and D=0.4 m.

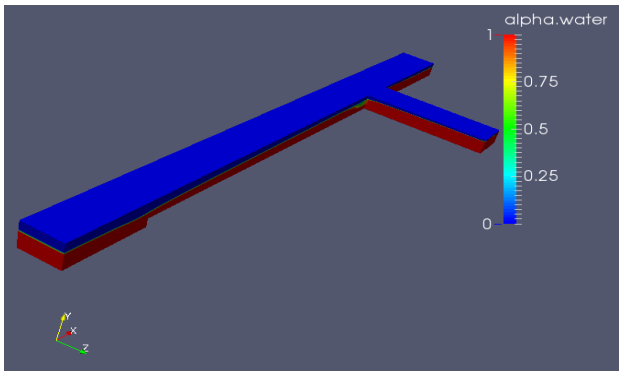

b- Alpha water at time=300 sec and D=0.4 m.

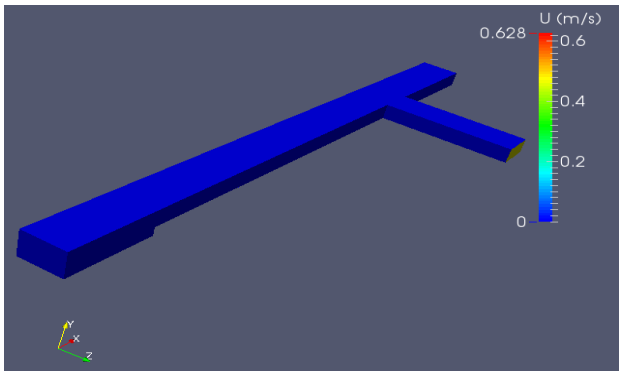

c- Velocity at time=0 sec and D=0.4 m.

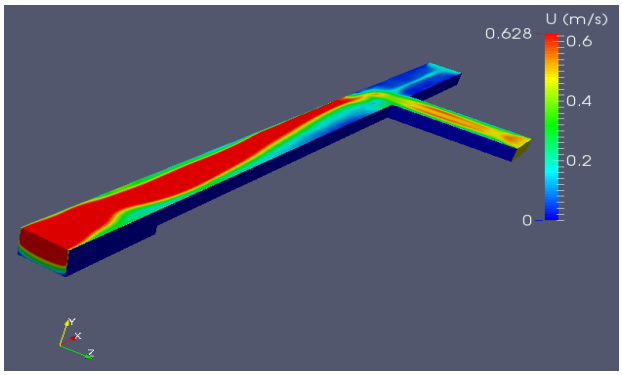

d- Velocity at time=300 sec and D=0.4 m.

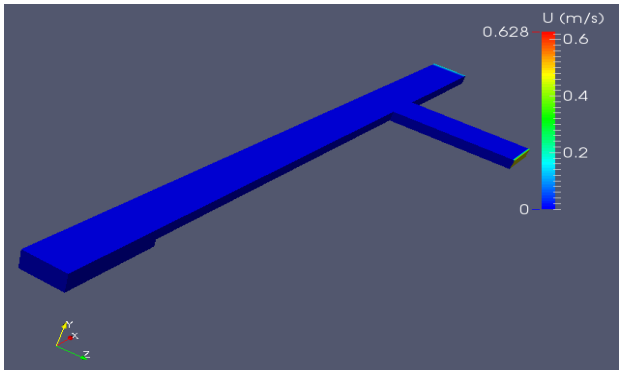

e- Velocity at time=0 sec and D=0.296 m.

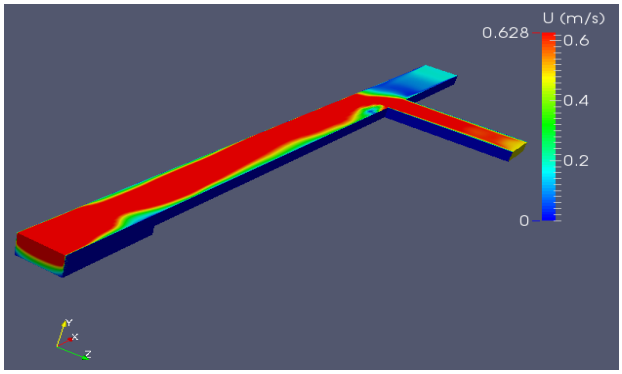

f- Velocity at time=300 sec and D=0.296 m.

Figure 4.22 : Realizable *k-ε* model.

- LES model: although the maximum velocity tends to follow irregular path, it almost occurs near the outer bank of the main channel as shown Figure 4.23.

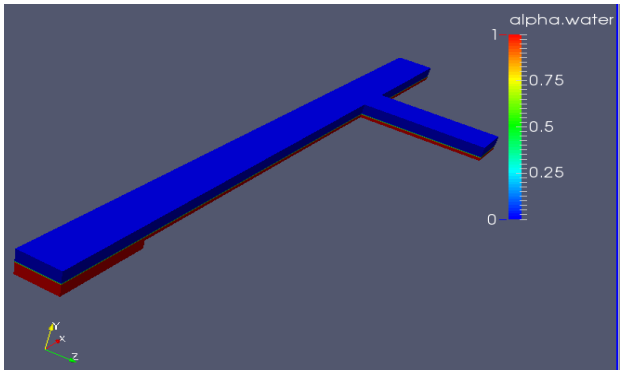

a- Alpha water at time=0 sec and D=0.4 m.

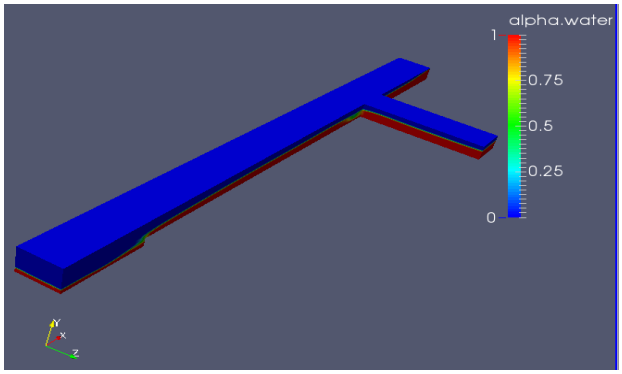

b- Alpha water at time=300 sec and D=0.4 m.

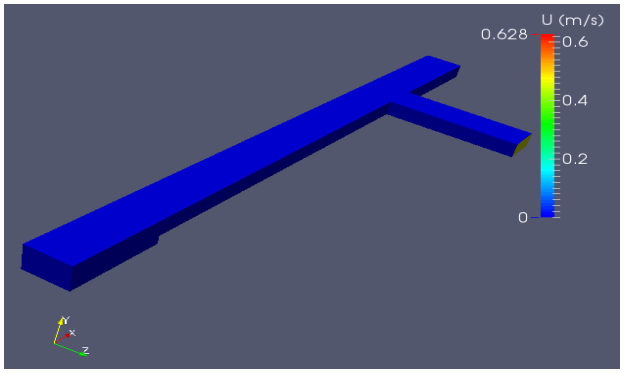

c- Velocity at time=0 sec and D=0.4 m.

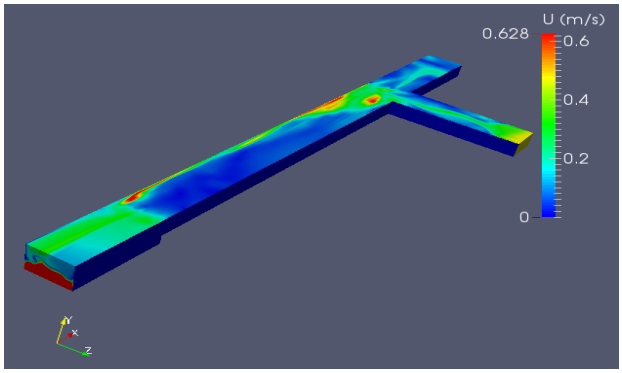

d- Velocity at time=300 sec and D=0.4 m.

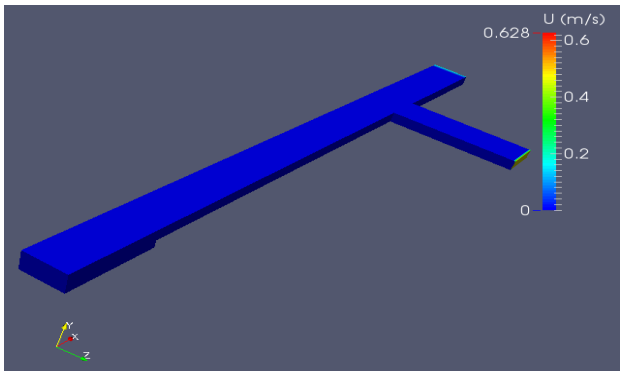

e- Velocity at time=0 sec and D=0.296 m.

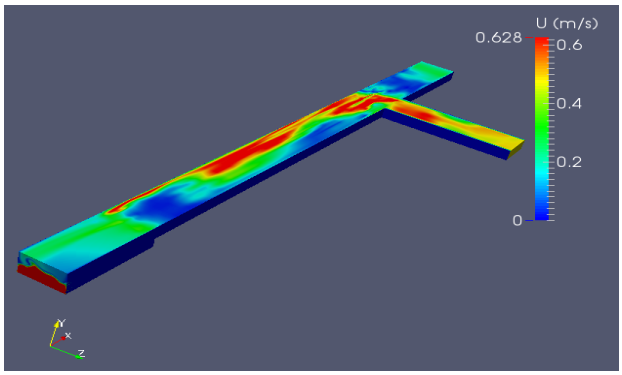

f- Velocity at time=300 sec and D=0.296 m.

Figure 4.23 : LES model.

Seeking to obtain more detailed insight for the performance of the velocity in each model, sections were taken at various places immediately after the junction. Thus, velocity curves for each section are developed to be compared with Shumate experimental data. These sections are illustrated in Figure 4.24.

The depth-averaged velocity across the width of the channel was calculated using Equation (4.1). The results are shown in Figure 4.25.

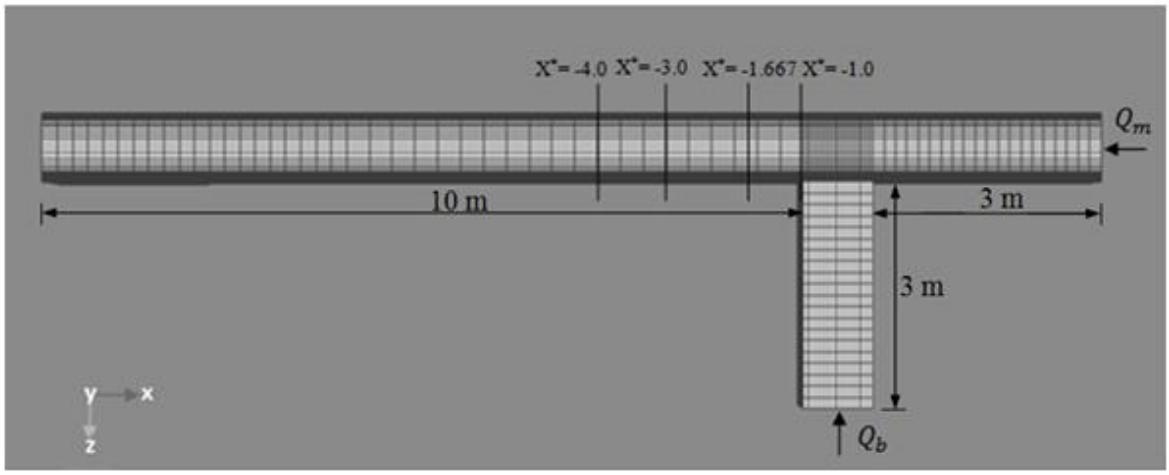

Figure 4.24: Sections of confluent channel.

$\boldsymbol{Q_m}$ = the main channel discharge; $\boldsymbol{Q_b}$ = the branch channel discharge; $\boldsymbol{x}^*$ = x/B, the coordinate x nondimensionalized with the channel width; $\boldsymbol{z}^*$= z/B, the coordinate y nondimensionalized with the channel width.

The results of the Free Surface Model showed the following:

- At section (x*= -1.0), which is exactly after the junction of the two channels, the velocity of the flow is increasing near the inner bank of the main channel and it is decreasing near the outer bank of the channel. All four models showed approximately the same results regarding the velocity. However, all of them overestimated the velocity values stated in the experiment. The model that showed a good agreement with the experiment in this section is standard *k*-*ε* model.
- At section (x*= -1.667), the velocity is decreasing near the inner bank of the main channel and is increasing towards the outer bank. All models are overestimated the experiment at the inner bank. However, all of them achieved a good agreement with the experiment except LES model. The standard *k*-*ε* model was having the best fit with the experiment data.
- At the last two sections, (x*= -3.0, and x*= -4.0), the velocity is also decreasing near the inner bank and increasing near the outer bank of the main channel. The models are overestimated the experiment at the inner bank and achieved better results near the

outer bank except LES model which also showed different results. The standard *k-ε* and LRR models at these sections were the best models.

- It can be observed that there are some discrepancies between numerical and experimental data. Several reasons might cause this situation. The velocity of water is affected by the velocity of air in this case of open channel flow. Also, the depth of water in the domain of the numerical models is different from the experimental water depth since it was difficult to obtain the same water depth exactly. In addition, the complexity of the flow features at this type of channels leads to numerical challenges in the simulation. Moreover, there are other reasons which were mentioned previously in section (4.7.1) that might cause the discrepancies between numerical and experimental data such as some errors in the measurements of the flow, the secondary flow is underestimated in the numerical models, and the approximation might be used in the computation of the flow characteristics.

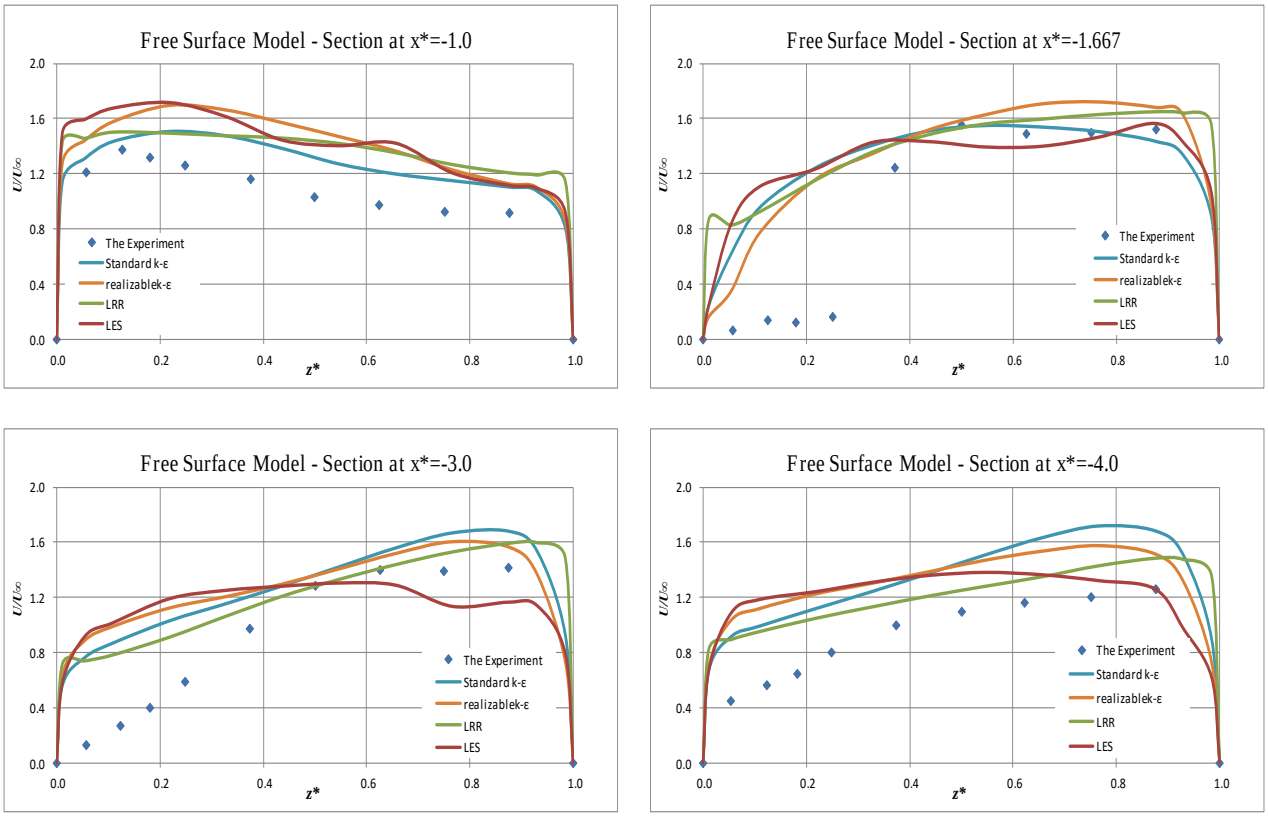

Figure 4.25: Velocity cross sections for Free Surface Model.

x^* = x/B, the coordinate x nondimensionalized with the channel width.

z^*= z/B, the coordinate z nondimensionalized with the channel width.

4.14.2. Rigid-Lid Model

This model is used usually with closed channel flow. In other words, this model takes into consideration only the effect of the flow without considering the air effect. In this case three numerical models, the standard *k-ε*, LRR, and realizable *k-ε* models, were studied and evaluated based on velocity parameter. Figure 4.26 shows velocity distribution at time zero

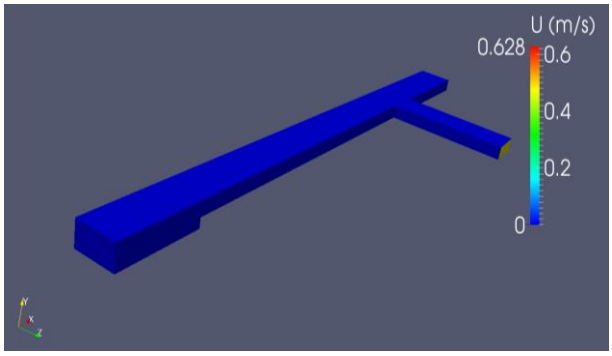

a- Velocity at time=0 sec

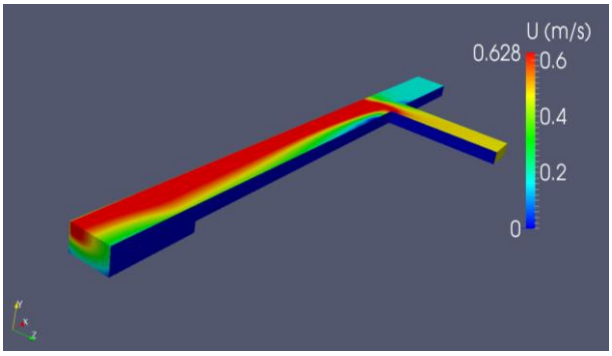

b- Velocity at time=100 sec.

Standard *k-ε* model

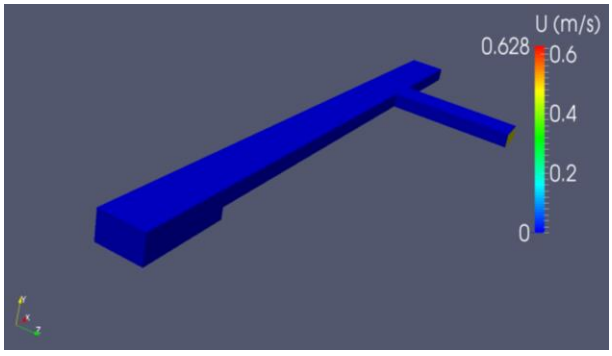

a- Velocity at time=0 sec.

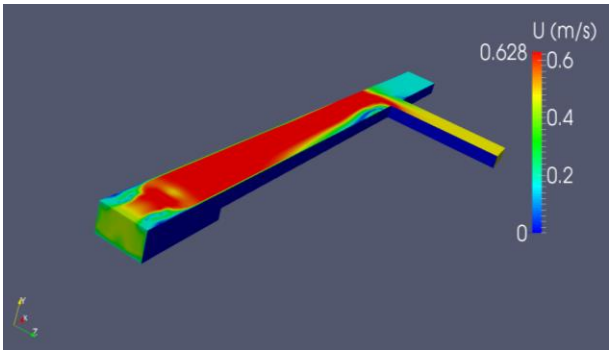

b- Velocity at time=100 sec.

LRR model

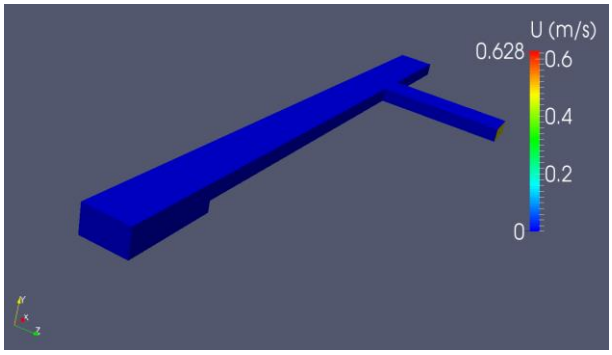

a- Velocity at time=0 sec.

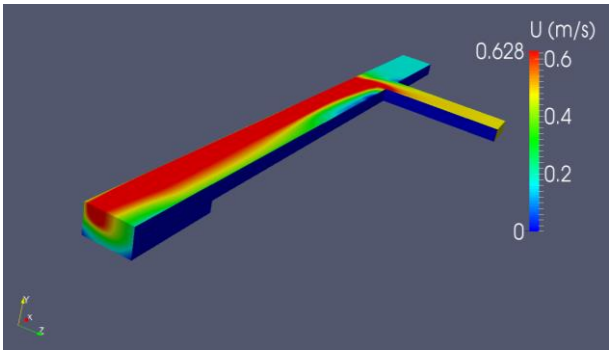

b- Velocity at time=100 sec.

Realizable *k-ε* model.

Figure 4.26: Rigid Lid Models.

and in the steady state at time 100 seconds for these three models. Note that the depth of the channel in this case equals to the water depth, which is (0.296 m).

All the three numerical models gave almost the same results for the distribution of the flow velocity. The maximum velocity moves from the branch channel towards the outer bank of the main channel. In order to explain that more, the same sections were taken, and the results are shown in Figure 4.27.

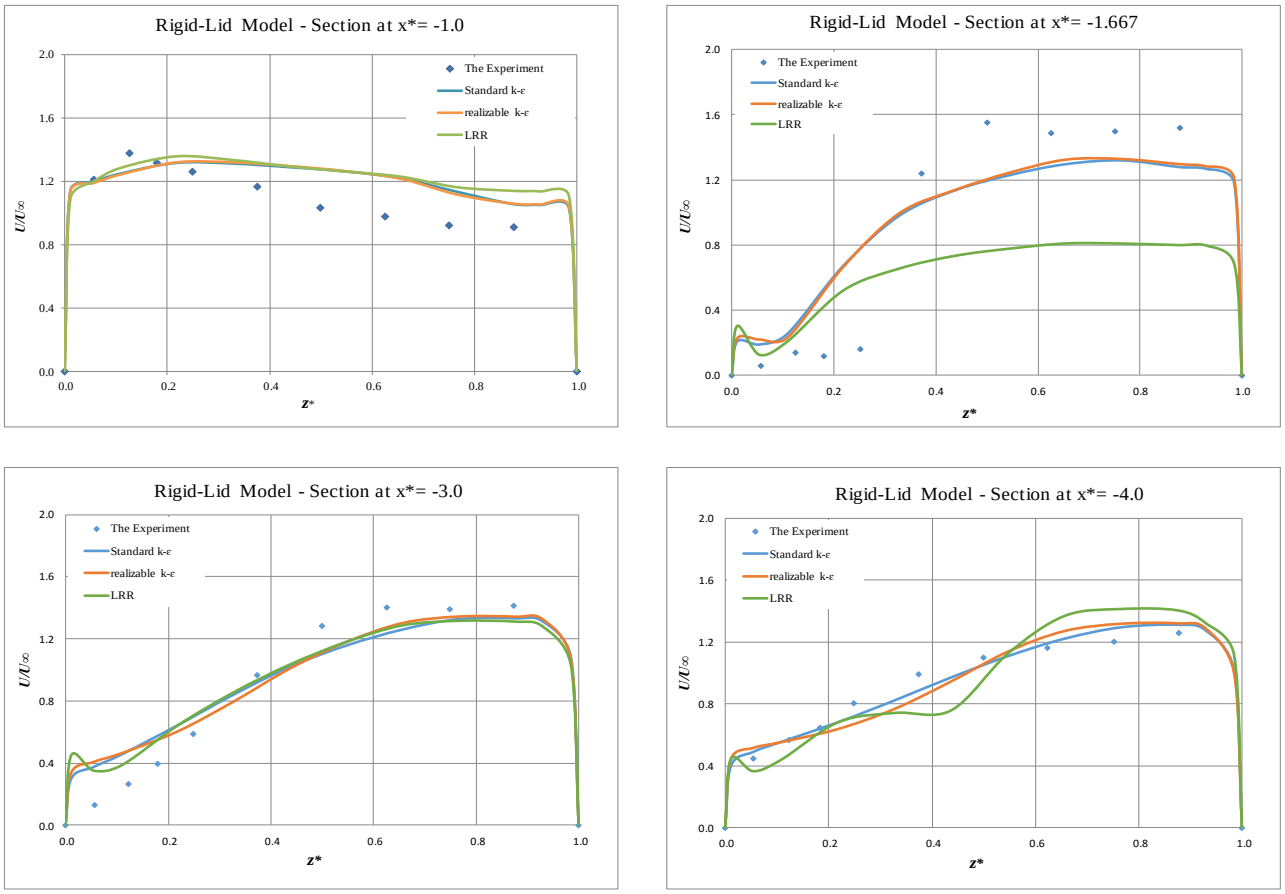

Figure 4.27: Velocity cross sections for Rigid Lid Model.

The results of the Rigid-Lid Model could be summarized as following:

- The distribution of the velocity is the same as mentioned previously at the case of Free Surface Model. It increases in the inner bank and decreases in the outer bank of the main channel at the first section (x*= -1.0), while it has an opposite trend for the rest sections (x*= -1.667, x*= -3.0, and x*= -4.0).

- All three numerical models gave almost the same results for velocity distribution except some differences in the LRR model especially at sections (x*=-1.667), and (x*=-4.0).
- Generally, the results are good and better than the Free Surface Model case, specifically, in the last two sections (x*= -3.0, and x*= -4.0), where the two models standard *k-ε* and realizable *k-ε* achieved a very good agreement with the experiment. However, for the first two sections the numerical models achieved the velocity features, and they gave good results, while they have not matched exactly the experiment and this is primarily happened because of the complexity of the flow features at this area.
- Accordingly, the best two numerical models in this case are standard *k-ε* and realizable *k-ε* models.

4.15. The Divergences in Velocity Distribution

The model standard *k-ε* in the case of Rigid-Lid Model was chosen to examine the variations in 3D velocity components since it is the model that achieved the best results compared with the experimental data in addition to realizable *k-ε* models from the same case. The same sections were adopted in this explanation for the velocity components which include (x*= -1.0, x*= -1.667, x*= -3.0, and x*= -4.0).

4.15.1. The Distribution of Longitudinal velocity

Longitudinal velocity is the velocity in the direction of the flow which is (x- direction) in this case. The upstream of x-direction is in the positive direction; therefore, the longitudinal velocity is negative almost in the entire channel. However, it is positive in the separation zone due to the reversed flow at this area. This component of velocity has a significant impact in the flow. In order to figure out the distribution of longitudinal velocity at the confluence of the two channels and after that, sections were taken in the main channel to elucidate this distribution. The contour lines of the longitudinal velocity are shown in these sections which are clarified in Figure 4.28. Note that the Y-axis and the Z-axis in the figures represent the depth and the width of the channel, respectively.

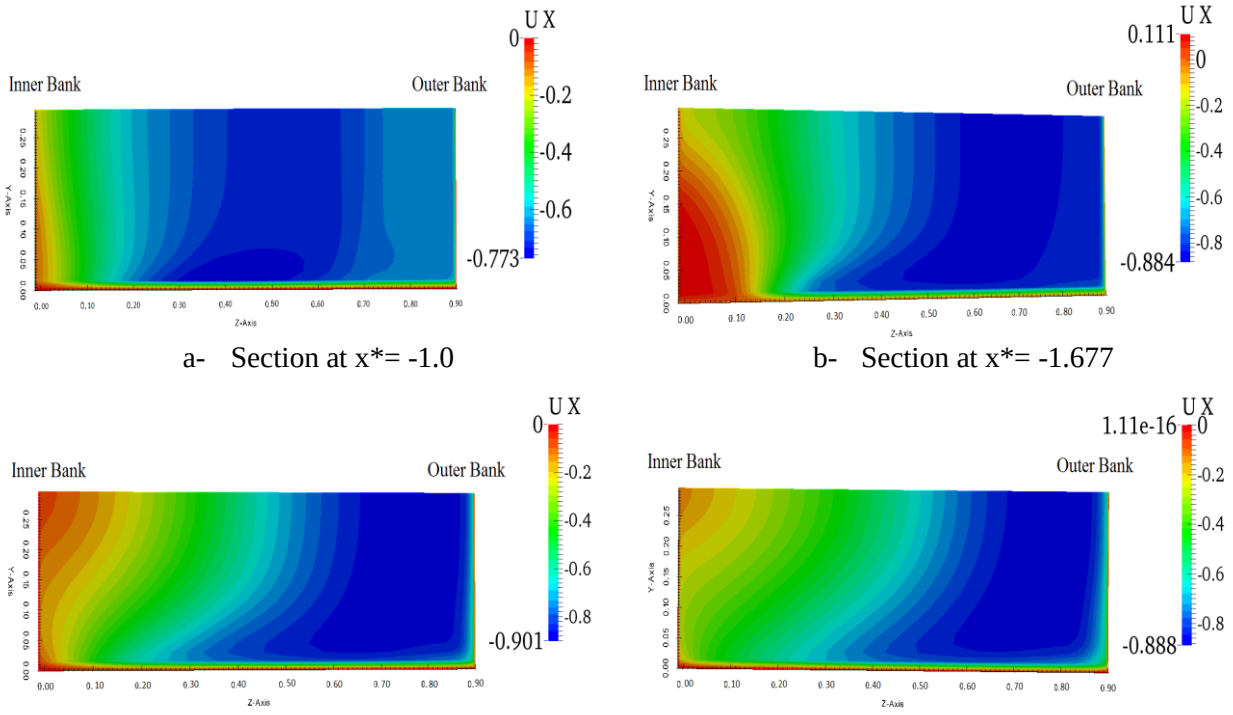

a- Section at x*= -1.0

b- Section at x*= -1.677

c- Section at x*= -3.0

d- Section at x*= -4.0

Figure 4.28: Longitudinal velocity sections.

The distribution of the longitudinal velocity can be explained as below:

- At the first section (x*= -1.0) which is immediately after the junction, all the velocities at this section are negative, the maximum velocity occurs near the inner bank and then decreases gradually towards the outer bank of the main channel which can be attributed to the longitudinal pressure gradients that exist near the inner bank in the channel bend and confluences.
- At the second section (x*= -1.677), the velocity is positive in the separation zone near the inner bank of the main channel and negative in the rest area of the section.
- At the last two sections (x*= -3.0), and (x*= -4.0), the separation zone is faded in these sections and all the velocities are negative.
- At all the sections, the longitudinal velocities are larger than those in the outer bank of the main channel.
- The higher longitudinal velocity occurs at the second section (x*= -1.677) due to the separation zone that occurs at this area.

4.15.2. The Distribution of Vertical velocity

It is the velocity in the vertical direction of the flow which is (z- direction) in this case. Figure 4.29 shows the vertical velocity distribution. The sections that were used to study the distribution of lateral velocity are the same ones that were used previously in longitudinal and vertical velocity. The axes of the channel are the same as well.

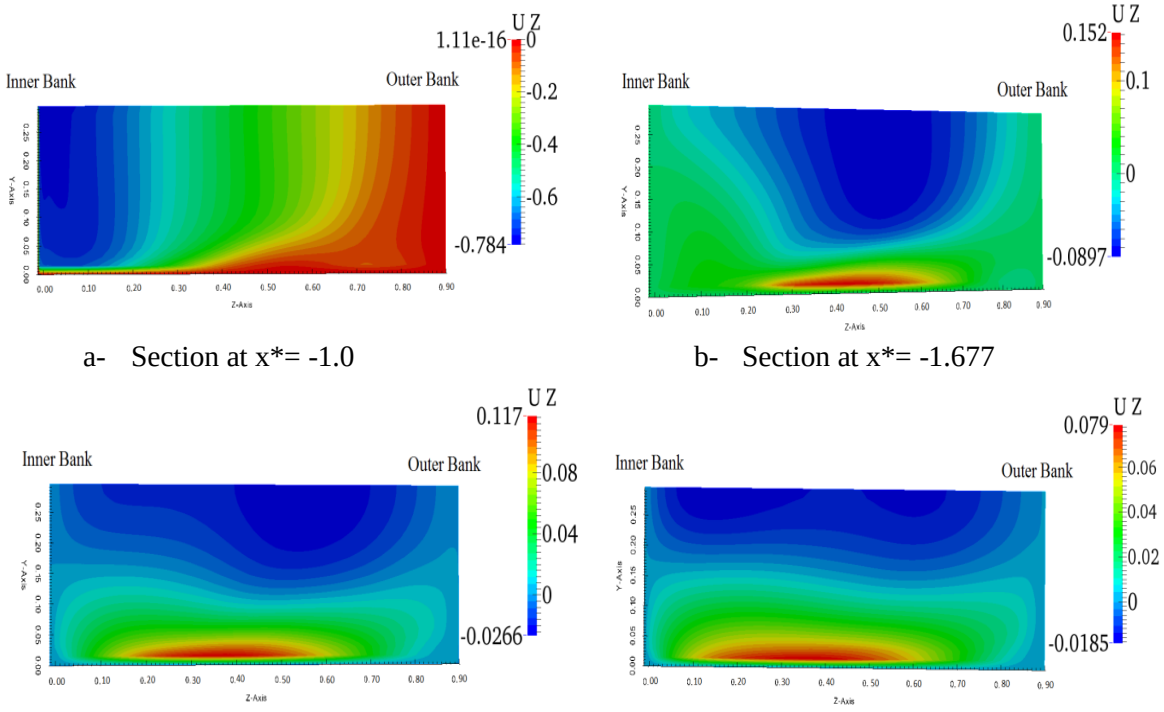

a- Section at x*= -1.0

b- Section at x*= -1.677

c- Section at x*= -3.0

d- Section at x*= -4.0

Figure 4.29: Vertical velocity sections.

The distribution of vertical velocity could be described as below:

- At the first section (x*= -1.0) directly after the junction, the maximum velocity occurs near the outer bank of the main channel.
- At the other three sections just shortly after the intersection, the maximum velocity tends to be in the middle of the channel bed towards the direction of the main channel.
- The velocities are positive near the channel bed and negative near the water surface at the last three sections, while at the first section the velocities are negative near the inner bank and positive near the outer bank of the main channel which indicates the existence of the secondary flows.

- The vertical velocity reaches its maximum at the second section at (x*= -1.667).

4.15.3. The Distribution of Lateral velocity

It is the velocity in the (y- direction) of the domain in this case. The distribution of the lateral velocity has been studied in the light of the same sections that mentioned previously as shown in Figure 4.30. Also, the two axes have been mentioned in above.

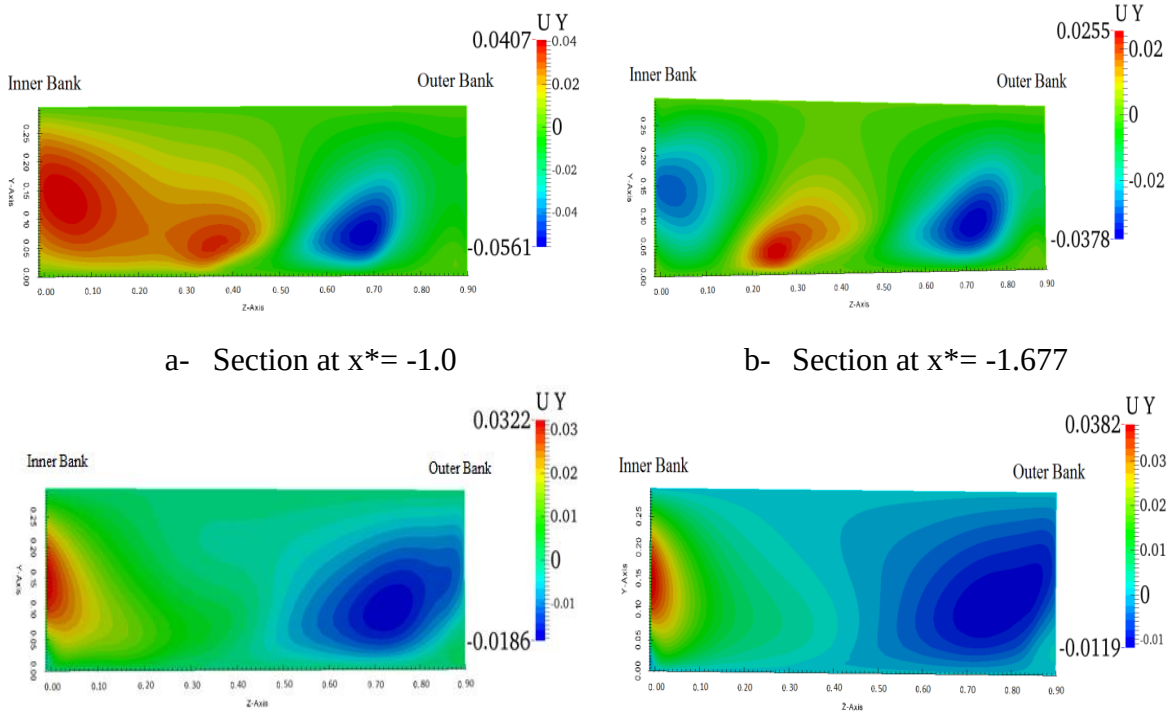

a- Section at x*= -1.0

b- Section at x*= -1.677

c- Section at x*= -3.0

d- Section at x*= -4.0

Figure 4.30: Lateral velocity sections.

The distribution of the vertical velocity could be summarized as following:

- At the first section (x*= -1.0) which is immediately after the junction, the recirculation zone or separation zone appears near the inner bank of the main channel. Also, there are two secondary flows at this section; the first one is the secondary flow of the branch channel which occurs near the inner bank of the main channel, and the second is the secondary flow of the main channel which occurs near the outer bank of the main channel.
- At the second section (x*= -1.677), the separation zone started to disappear.

- At the last two sections (x*= -3.0), and (x*= -4.0), the secondary flows of the two channels are clear in these sections. They rotate against each other, and they fade gradually in the direction of the main channel.
- The strength of the branch secondary flow is larger than that of the main channel.

4.15.4. The Distribution of Flow Longitudinal Velocity along the two channels

Figure 4.31 indicates the distribution of longitudinal velocity along the two channels. All the flow features that occurs in the channel confluences could be visualized by this figure. Immediately after the meeting of the two channels, the stagnation zone appears in the area of the confluence at the corner of the upstream. The velocity reduces at this region of the channel. Stagnation zone is followed by the deflection zone where the flow of the main channel deflects towards the outer bank of the same channel due to the new flow that coming from the branch channel. The separation zone occurs at the downstream of the junction near the inner bank of the main channel due to the changing in the direction of the branch channel from straight to curvature. The region of maximum velocity called the acceleration zone which appears near the external bank of the main channel. The zone of shear layers could be found in the area between the recirculation zone and acceleration zone. Finally, the recovery zone which occurs after the ending of the confluence hydrodynamics impact on the flow.

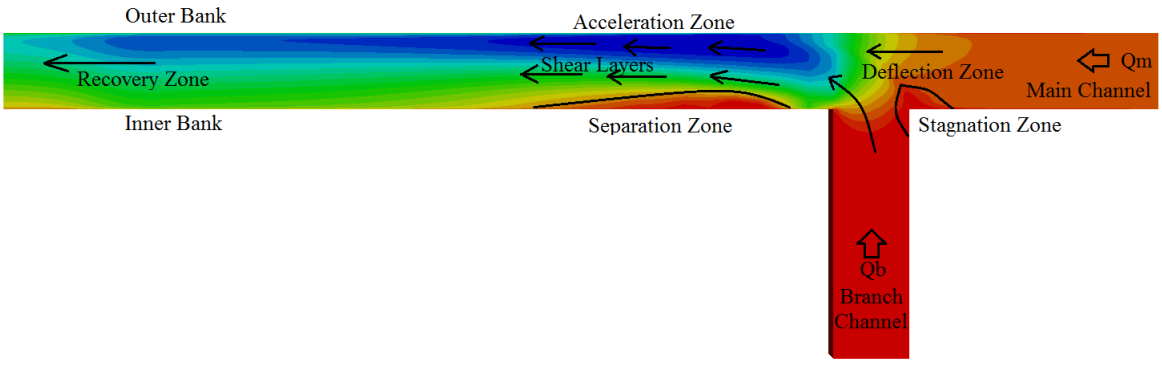

Figure 4.31: The longitudinal velocity along the confluent channel.

CHAPTER FIVE

CONCLUSIONS AND SUGGESTIONS FOR FUTURE WORK

5.1. Conclusions

Studying the characteristics of the flow in river bends and confluences could be considered one of the important tasks in river engineering due to the significant existence of curvature and confluences in rivers and their great impact on river engineering problems. However, examining the dynamic of the flow in river bends and confluences is a hard task because of the complexity of flow features at this area, which makes it difficult to be captured and determined. Secondary flow is one of the flow characteristics in curved and confluent rivers. In this study, secondary currents were studied by employing a 3D OpenFOAM numerical model. Basically, OpenFOAM depends on the finite volume method (FVM), which includes a lot of numerical schemes that are implemented both for time and space integration. Two sets of experimental data were used to validate the proposed model. Two solvers were used; the InterFoam solver which is used in open channel flow (Free Surface Model), and the PisoFoam solver which is used in closed channel flow (Rigid-Lid Model). Various turbulence models (standard k-ε, realizable k-ε, LRR, and LES) are applied in the numerical model of this study.

For the curved channel, there was a good agreement for the velocity parameter between the employed numerical models and the experimental and other numerical data. The following conclusions can be obtained from the outputs of the simulations:

- The flow velocity distribution in all the four models (standard k-ε, realizable k-ε, LRR, and LES) indicate that the maximum velocity tends to be near the inner bank at the beginning of the bend, and it turns gradually towards the outer bank near the bend exit.
- Both Free Surface and Rigid-Lid Models showed good agreements compared to the experimental and other numerical data.
- The best employed model is realizable k-ε of the Free Surface Model for the sections (0˚, 35˚, 65˚, 100˚, 143˚) in the bend. While the employed model of standard k-ε and realizable k-ε of the Rigid-Lid Model were the best fit for the section at 186˚ near the

bend exit.

- The secondary flows exist at the beginning of the bend and then they escalate to reach the peak value approximately at the centre of the bend and then they decrease gradually towards the bend exit.
- The vertical velocities are positive near the water surface and negative near the channel bed, which indicates the existence of the secondary flows.

For the confluent channel, the velocity parameter was used to study the flow features as well. A comparison between the employed numerical models and the experimental and other numerical data was conducted. Based on the results obtained, the following points can be concluded:

- The maximum velocity moves from the branch channel towards the outer bank of the main channel.
- The results of the Rigid-Lid Model were more accurate and better than those of Free Surface Model, specifically, at the area immediately after the junction.
- The best two numerical models in this case are standard k-ε and realizable k-ε models of the Rigid-Lid Model.
- There are two secondary flows which appear in the main channel; the secondary flow of the branch channel, which occurs near the inner bank of the main channel, and the secondary flow of the main channel, which occurs near the outer bank of the main channel.
- The secondary flows of the two channels rotate in opposite directions and fade gradually in the direction of the main channel.
- The strength of the branch secondary flow is larger than that of the main channel.
- The vertical velocities are positive near the channel bed and negative near the water surface of the main channel at the last three sections, which indicates the existence of the secondary flows.
- In the case of Rigid-Lid Model, there are some variation between the numerical models and the experimental data at the two sections directly after the junction. While at the other sections in the direction of the main channel, the numerical models achieved a good agreement with the experimental data. This could be attributed to the sudden

change in the channel from straight to curvature, which makes the flow features at this area difficult to be captured and determined.

5.2. Suggestions for further research

Based on the findings of this research, the following can be recommended:

- This study focused on implementing OpenFOAM to simulate the flow in channels with sharp curves. Therefore, it is recommended to consider other types of curved channel, such as moderate and mild curvature, for future studies. In addition, various degrees of curvature and cross flows should be considered to examine the effect of secondary flows and their impact on the design of river engineering works.
- The analysis conducted for confluent channel in this study was dedicated for asymmetrical confluent channel. Therefore, studying other types of confluent channels, such as symmetrical confluent channel or different degrees' confluent channels is highly recommended. Furthermore, additional field and experimental studies are needed to collect more accurate data for such cases.
- Since the main and secondary flow are affected by the shape of the cross section of the curved channel, it is important to conduct simulations for curved channels of different shape like trapezoidal and circular.
- Bed topography is an important factor in curved and confluent channel. It is necessary to examine the effect of deformed and sloped bed on the main flow and secondary flow and thereafter on the channel.
- OpenFOAM was used to simulate two cases considered herein using four turbulence models. However, more turbulence models could be implemented to increase the area of comparison between the models and field data. In addition, higher resolution, finer grid, parallel simulation, domain decomposition, and different wallFunctions could be used in the simulation to obtain results with higher level of accuracy.

REFERENCES

Ahmadi, M. et al. (2009) A 2D Numerical Depth-Averaged Model for Unsteady Flow in Open Channel Bends. Journal of Agricultural Science and Technology, 1: 457–68.

Akhtari, A.A., Abrishami, J. and Sharifi, M.B. (2009) Experimental Investigations Water Surface Charachteristics in Strongly Curved Open Channels. Journal of Applied Sciences, 9(20): 3699–3706.

Alessandra, C. (2008) Analysis and Modelling of River Meandering. PhD thesis, Technical University of Delft, South Holland, Netherlands.

Anderson J (1995) Computational Fluid Dynamics, the Basic with Applications. McGraw-Hill, US.

Baldwin, B., and Lomax, H. (1978) Thin-Layer Approximation and Algebraic Model for Separated Turbulent Flows. AIAA 78-257, Huntsville, AL.

Barbhuiya, A.K. and Talukdar, S. (2010) Scour and Three-Dimensional Turbulent Flow Fields Measured by ADV at a 90-Degree Horizontal Forced Bend in a Rectangular Channel. Flow Measurement and Instrumentation, 21(3): 312–321.

Barkdoll, B. (2003) Discussion of "Experiments on Flow at a 90-Degree Open-Channel Junction by Larry J. Weber, Eric D. Schumate, and Nicola Mawer, 129(2): 165-166.

Bergs, M.A. (1990) Flow Processes in a Curved Alluvial Channel. PhD thesis, Department of Civil and Environmental Engineering, University of Iowa, Iowa City, Iowa.

Best, J. (1987) Flow dynamics at River Confluences: Implications for Sediment Transport and Bed Morphology. The Society of Economic Paleontologists and Mineralogists (SEPM) Recent Developments in Fluvial Sedimentology, SP39: 27–35.

Biron, P., Best, J. and Roy, A., 1996. Effects of Bed Discordance on Flow Dynamics at Open Channel Confluences. Journal of Hydraulic Engineering, 122(12): 676–682.

Birjukova, O. et al. (2014) Three-Dimensional Flow Field at Confluent Fixed-Bed Open Channels. Proceedings of the 7th International Conference on Fluvial Hydraulics, RIVER FLOW 2014 (1944): 1007–1014.

Blanckaert, K. (2001) A Model for Flow in Strongly Curved Channel Bends. In Proceedings of. 29thIAHR Congress, Beijing, China: 42–50.

Blanckaert, K. (2011) Hydrodynamic Processes in Sharp Meander Bends and Their Morphological Implications. Journal of Geophysical Research: Earth Surface, 116(F1), March 2011.

Blanckaert, K. et al. (2009) Meandering: Field Experiments, Laboratory Experiments and Numerical Modelling. Presented at: River, Costal and Estuarine Morphodynamics (RCEM), September 21-25, Santa Fe, Argentina.

Blanckaert, K. and Graf, W. (2001) Experiments on Flow in a Strongly Curved Channel Bend. In Proceeding of 29th IAHR Congress, Beijing, China: 371–377.

Blanckaert, K. and Graf, W. (2004) Momentum Transport in Sharp Open-Channel Bends. Journal of Hydraulic Engineering, 130(3): 186–198.

Blanckaert, K. and De Vriend, H. (2010)A Nonlinear Model Without Curvature Restrictions For Flow in Open-Channel Bends. Journal of Geophysical Research: Earth Surface, 115 (F4).

Blanckaert, K. and De Vriend, H. (2003) Nonlinear Modelling of Mean Flow Redistribution in Curved Open Channels. Water Resources Research, December 2003, 39(12): 1375.

Blankaert, K. and De Vriend, H. (2004) Secondary Flow in Sharp Open-Channel Bends. Journal of Fluid Mechanics, 498: 353–380.

Blankaert, K. and De Vriend, H.J. (2005) Turbulence Structure in Sharp Open-Channel Bends. Journal of Fluid Mechanics, 563: 27–48.

Booij, R.(2003a) Measurements and Large Eddy Simulations of the Flows in Some Curved Flumes. Journal of Turbulence, 4(8): 1–17.

Booij, R.(2003b) Modelling the Flow in Curved Tidal Channels and Rivers. International Conference on Estuaries and Coasts, November 9-11, Hangzhou, China.

Bradbrook et al. (1998) Investigation of Controls on Secondary Circulation in a Simple Confluence Geometry Using a Three-Dimensional Numerical Model. Hydrological Processes, 12:1371-1396.

Bradbrook et al. (2001) Role of Bed Discordance at Asymmetrical River Confluences. Journal of Hydraulic Engineering, 127: 351-368.

Cable, Matt (2009) An Evaluation of Turbulence Models for the Numerical Study of Forced and Natural Convective Flow in Atria. Master's thesis, Department of Mechanical and Materials Engineering, Queen's University, Kingston, Ontario, Canada.

Caboussat, A. (2003) Analysis and Numerical Simulation of Free Surface Flows., PhD thesis, Faculty Science Base, Institute of Analysis and Scientific Computing, Division of Mathematics Polytechnic, Lausanne.

Cameron, H. and Bauer, B. (2014) River Bank Erosion Processes along the Lower Shuswap River. Final Project Report submitted to Regional District of North Okanagan, University of British Columbia Okanagan.

Camporeale, C. et al. (2007) Hierarchy of Models for Meandering Rivers and Related Morphodynamic Processes, Reviews of Geophysics, March 2007, Vol 45 (1): 1-28.

Cebeci, T., and Smith, A. (1974) Analysis of Turbulent Boundary Layers. Academic Press.

Dabaghi, F. et al. (2005) Numerical Modelling and Analysis of Water Free Surface Flows. Informatics for Environmental Protection - Networking Environmental Information: 563–567.

Davidson, L. (2015) An Introduction to Turbulence Models. Publication 97/2, January 14, Department of Thermo and Fluid Dynamics, Chalmers University of Technology G¨oteborg, Sweden.

Davis, W. (1903) The development of river meanders. The Geological Magazine, New Series, Decade IV, 10: 145–148.

De Serres, B. et al. (1999) Three-Dimensional Structure of Flow at a Confluence of River Channels with Discordant Beds. Geomorphology, 26: 313-335.

De Vriend, H. and Geldof, H. (1983) Main Flow Velocity in Short River Bends. Journal of Hydraulic Engineering, 109 (7): 991-1011.

De Vriend, H. (1980). Velocity Redistribution in Curved Rectangular Channels. Journal of Fluid Mechanics, 107: 423–439.

De Vriend, H. (1976) A Mathematical Model Of Steady Flow in Curved Shallow Channels. Journal of Hydraulic Research, 15 (1): 37-54.

Dey, S. (2014) Fluvial Hydrodynamics: Hydrodynamic and Sediment Transport Phenomena, Springer, Berlin.

Dietrich and Smith (1983) Influence of the Point Bar on Flow through Curved Channels. Water Resources Research, 19(5): 1173-1192.

Duan, J. (2004) Simulation of Flow and Mass Dispersion in Meandering Channels. Journal Of Hydraulic Engineering, ASCE, October: 964-976.

Duchêne, V. (2014) On the Rigid-Lid Approximation for Two Shallow Layers of Immiscible Fluids with Small Density Contrast. Journal of Nonlinear Science, 24(4): 579–632.

Engelund F. (1974) Flow and Bed Topography in Channel Bends. Journal of the Hydraulics Division of the American Society of Civil Engineers 100: 1631–1648.

Esfahani, F.S., (2009) Experimental Investigation of Erosion and Deposition in River Meanders. 5th National Congress on Civil Engineering, May 4-6, 2010, Ferdowsi University of Mashhad, Mashhad, Iran.

Esfahani, F.S. and Keshavarzi, A.R. (2009). An Experimental Study of Flow Structure in Fixed Bed Meandering River. 8thInternational Congress on Civil Engineering, May 11-13, Shiraz University, Shiraz, Iran.

Esfahani, F.S. and Keshavarzi, A.R. (2010) The Effect of Different Curvatures on Flow Structure Inside the River Meander. 5thNational Congress on Civil Engineering, May 4-6, Ferdowsi University of Mashhad, Mashhad, Iran.

Falcon, M. (1984) Secondary Flow in Curved Open Channels. Annual Reviews. Fluid Mechanics, 16(1): 179-193.

Faure, J. et al., (2004) 3D Modelling Of Unsteady Free-Surface Flow In Open Channel. Journal of Hydraulic Research, Vol 42(3): 263–272.

Flint, J. (1980) Tributary Arrangements in Fluvial Systems. American Journal of Science, January 1, 1980 (280): 26–45.

Flokstra, C. (1977) The Closure Problem for Depth-Averaged Two-Dimensional Flows. Proceedings of the 17th congress of In term Association for Hydraulic Resources (IAHR). 15-19 August, pp. 247–56, Baden-Baden.

Ghamry, H. and Steffler, P. (2005) Two-Dimensional Depth-Averaged Modelling of Flow in Curved Open Channels. Journal of Hydraulic Resources, 43(1): 44–55.

Gildeh, H. (2013) Numerical Modelling of Thermal / Saline Discharges in Coastal Waters. Masters of Applied Science in Civil Engineering. University of Ottawa, Ottawa, Canada.

Giri, S., Shimizu, Y. and Fujita, M. (2003) Flow Characteristics in a Mildly Meandering Channel With and Without River Training Structures. Annual Journal of Hydraulic Engineering, JSCE, Vol (47): 835-840.

Graf, W. and Blanckaert, K. (2002) Flow around Bends in Rivers. Proceedings of 2nd International Conference, New Trends in Water and Environmental Engineering for Safety and Life: Eco-compatible Solutions for Aquatic Environments, June 24-28, 2002, Capri, Italy.

Gurram, S., Karki, K. and Hager, W. (1997) Subcritical Junction Flow. J Hydraul Eng, 123(5): 447-455.

Guymer, I. (1998) Longitudinal Dispersion in Sinuous Channel with Changes in Shape. Journal of Hydraulic Engineering, Vol 124, January: 33-40.

Howard H. Chang (1988) Fluvial Processes in River Engineering. John Wiley & Sons, New York, NY.

Herreras, N. and Izarra, J. (2013) Two-Phase Pipe Flow Simulations with OpenFOAM. Master's thesis, Norwegian University of Science and Technology, Norway.

Hervouet, J.and Van Haren, L. (1996). Recent Advances in Numerical Methods for Fluid Flows. In: Anderson, Walling and Bates (eds.), Floodplain Processes, Chapter 6, Wiley & Sons.

Hickin, E. (1978) Mean Flow Structure in Meanders of the Squamish River, British Columbia. Can. J. Earth Sci., 15(11): 1833-1849.

Hickin, E. and Nanson, G. (1984) Lateral Migration Rates of River Bends. J. Hydraulic Engineering, 110(11): 1557-1567.

Hjertager, B. (2009) Lecture Notes in OpenFOAM - MSK 600. University of Stavanger.

Hodskinson, A. and Ferguson, R. (1998) Numerical Modelling of Separated Flow in River Bends: Model Testing and Experimental Investigation of Geometric Controls on the Extent of Flow Separation at the Concave Bank. Hydrological Processes, 12(8): 1323-1338.

Horizonte, B. (2014) Numerical Modelling of a 90° Open- Channel Confluence Flow using OpenFOAM. Masters of Applied Science in Environment and Water Resources, Federal University of Minas Gerais, Belo Horizonte, Brazil.

Huai W, et al. (2010) Numerical Simulation of Horizontal Buoyant Wall Jet, J Hydrody 22(1): 58-65.

Hsu, C., Lee, W. and Chang, C. (1998) Subcritical Open Channel Junction Flow. Journal of Hydraulic Engineering, 124(8): 847-855.

Ikeda, S., Yamasaka, M. and Kennedy, J. (1990) Three-Dimensional Fully Developed Shallow- Water Flow in Mildly Curved Bends. Fluid Dynamics Research, 6(3-4): 155-173.

Ippen, A.T. and Drinker, P.A. (1962) Boundary Shear Stresses in Curved Trapezoidal Channels. Journal of the Hydraulics Division, ASCE, 88: 143-179.

Jian, Y. and McCorquadale, J. (1998) Simulation of Curved Open Channel Flows by 3D Hydrodynamic Model. Journal of Hydraulic Engineering, ASCE, 124(7): 687-698.

Jin, Y. and Steffler, P. (1993) Predicting Flow in Curved Open Channels by Depth-Averaged Method. Journal of Hydraulic Engineering, 119(1): 109-124.

Johannesson, H (1988) Theory of River Meanders. PhD thesis, University of Minnesota.

Johannesson, H. and Parker, G. (1989) Secondary Flow in Mildly Sinuous Channel. Journal of Hydraulic Engineering, 115(3): 289-308.

Jung J. and Yoon, S. (2000) Flow and Bed Topography in a 180-Degree Curved Channel. 4th International Conference on Hydro-Science and Engineering, Korea Water Resources Association.

Kalkwijk, J., and Devriend, H. (1980) Computation of the Flow in Shallow River Bends. Journal of Hydraulic Resources, 18(4): 327-341.

Knighton, D. (1998) Fluvial Forms and Processes: A New Perspective. Routledge, Taylor and Francis Group, London and New York.

Lambert, R. (2012) Development of a Numerical Wave Tank using OpenFOAM. Masters of Applied Science in Energy Sustainable, University of Coimbra, Coimbra, Portugal.

Lane, S.et al.(1999). The Application of Computational Fluid Dynamics to Natural River Channels: Three-Dimensional Versus Two-Dimensional Approaches. Geomorphology 29: 1–20.

Leite, Ribeiro, M et al. (2012) Hydraulic Design of A-Type Piano Key Weirs. Journal Hydraulic Research, 50 (4): 400-408.

Leschziner, M. and Rodi, W. (1979) Calculation of Strongly Curved Open Channel Flow. Journal of the Hydraulics Division, 105(10): 1297-1314.

Liaghat, A., Mohammadi, K. and Rahmanshahi, M. (2014) 3D Investigation of Flow Hydraulic in U Shape Meander Bends with Constant, Decreasing and Increasing Width. Journal of River Engineering, 2(3): 12-23.

Lien, H.C., Hsieh, T.Y. and Yang, J.C. (1999) Bend-Flow Simulation Using 2D Depth-Averaged Model. Journal of Hydraulic Engineering, 125(10): 1097-1108.

Ludeña, G. (2015) Hydro-Morphodynamics of Open-Channel Confluences with Low Discharge Ratio and Dominant Tributary Sediment Supply. PhD thesis, Department of Civil Engineering, Architecture, and Georesources, University of Lisbon, Portugal.

Mangani, L. (2010) Development and Validation of an Object Oriented CFD Solver for Heat Transfer and Combustion Modelling in Turbomachinery Applications. PhD thesis, Department of Energy, University of Firenze, Florence, Italy.

Mockmore, C. (1944) Flow around Bends in Stable Channels. Transactions of the American Society of Civil Engineers, ASCE, 109: 593-618.

Mosley, M. (1976) An Experimental Study of Channel Confluences. Journal of Geology, 84(5): 535-562.

Naji Abhari, M., Ghodsian, M., Vaghefi, M. and Panahpur, N. (2010) Experimental and numerical simulation of flow in a 90-degree bend. Flow Measurement and Instrumentation, 21(3): 292–298.

Nayak, P. (2010) Meandering Effect for Evaluation of Roughness Coefficients and Boundary Shear Distribution in Open Channel Flow. Master of Technology in Civil Engineering, Department of Civil Engineering, National Institute of Technology, Rourkela, India.

Nouh, M. and Townsend, R. (1979) Shear-Stress Distribution in Stable Channel Bends. Journal of the Hydraulics Division, ASCE, 105(10): 1233–1245.

Odgaard, A. (1986) Meander Flow Model. I: Development. Journal of Hydraulic Engineering, ASCE, 112(12): 1117–1135.

Odgaard, A. and Bergs, M. (1988) Flow Processes in a Curved Alluvial Channel. Water Resource. Research, 24(1): 45–56.

Open Source CFD Toolbox. OpenFOAM - User Guide, December 2015. Version 3.0.1.

Ottevanger, W., Blanckaert, K. and Uijttewaal, W. (2011) A Parameter Study on Bank Shear Stresses in Curved Open Channel Flow by Means of Large-Eddy Simulation. In Proc., 7th IAHR Symposium on River, Coastal and Estuarine Morphodynamics, International Association for Hydro-Environment Engineering and Research, Madrid, Spain: 1917–1927.

Parsons, D. (2003) Discussion of “Three-Dimensional Numerical Study of Flows in Open Channel Junctions” by Huang J., Weber LJ, Lai WG. Journal of Hydraulic Engineering, 129: 822-823.

Parsons, D. et al. (2007) Form Roughness and the Absence of Secondary Flow in a Large Confluence-Diffluence Rio Parana Argentina. Earth Surface Processes and Landforms, 32: 155-162.

Poungkrajorn, T. (2015) Assuring Asset Integrity Through Improving the Accuracy of Leakage Source Identification of a Permanently Installed Subsea Leak Detection System using Artificial Neural Networks. Master's thesis, Faculty of Science and Technology, University of Stavanger, Stavanger, Norway.

Ramamurthy, A., Carballada, L. and Tran, D. (1988) Combining Open-Channel Flow at Right-Angled Junctions. Journal of Hydraulic Engineering, 114(12): 1449-1460.

Ramamurthy, A., Qu, J. and Vo, D. (2007) Numerical and Experimental Study of Dividing

Rhoads, B. and Kenworthy, S. (1995) Flow Structure at an Asymmetrical Stream Confluence. Geomorphology, 11: 273-293.

Rhoads, B. and Sukhodolov, A. (2001) Field Investigation of Three-Dimensional Flow Structure at Stream Confuluance:1 Thermal Mixing and Time-Averaged Velocities. Water Resources Research, 37: 2393-2410.

Riley, J. (2013) The Fluvial Dynamics of Confluent Meander Bends. PhD thesis, Graduate College, University of Illinois, Urbana-Champaign

Rozovskii, I. (1961) Flow of Water in Bends of Open Channels. The Israel Program for Scientific Transitions, Jerusalem.

Rust, B. (1978) A classification of alluvial channel systems. Fluvial Sedimentology, Memoir (5):187–198.

Seminara, G. (2006) Meanders. Journal of Fluid Mechanics, 554: 271–97.

Seminara, G. and Tubino, M. (1989) Alternate Bars and Meandering: Free, Forced and Mixed Interactions. In a Ikeda S, Parker G, (ed.), River Meandering, (12):267–320.

Seo, I. and Jung, Y. (2010) Velocity Equation of Secondary Flow in Meandering Channel. 36(b), p. 170.

Shakibainia, A., Tabatabai, M. and Zarrati, A. (2010) Three-Dimensional Numerical Study of Flow Structure in Channel Confluences. Can J Civil Eng, 37(5): 772-781.

Shams, M., Ahmadi, G. and Smith, D. (2002) Computational Modelling of Flow and Sediment Transport and Deposition in Meandering Rivers. Advances in Water Resources, 25(6): 689-699.

Shukry, A. (1950). Flow around Bends in an Open Flume. Journal Paper, 115(1): 751-779.

Shumate, E. (1998) Experimental description of flow at an open-channel junction. Master's thesis, University of Iowa, Iowa.

Song, C., Seo, I. and Kim, Y. (2012) Analysis of Secondary Current Effect in the Modelling of Shallow Flow in Open Channels. Advances in Water Resources, 41: 29-48.

Stoesser, T., Ruether, N. and Olsen, N.R.B. (2010) Calculation of Primary and Secondary Flow and Boundary Shear Stresses in a Meandering Channel. Advances in Water Resources, 33(2): 158-170.

Sui, J., Fang, D. and Karney, B. (2006) An Experimental Study into Local Scour in a Channel Caused by a 90 Bend. Civil, Canadian Journal of Engineering, 33(7): 902-911.

Tawekal, J. (2015) CFD Simulation of the Flow over a 2-Dimensional Pipe and Vortex Induced Vibration of the Pipe with 1 Degree of Freedom. Master's thesis, Faculty of Science and Technology, University of Stavanger, Norway.

Taylor, E. (1944) Flow Characteristics at Rectangular Open-Channel Junction. Journal of Hydraulic Engineering, ASCE, 10(6): 893-902.

Termini, D. and Piraino, M. (2011) Experimental Analysis of Cross-Sectional Flow Motion in A Large Amplitude Meandering Bend. Earth Surf Process Landforms, 36(2): 244-256.

Thanh, M. et al. (2010) Depth-averaged 2D Models with Effects of Secondary Currents for Computation of Flow at a Channel Confluence. Proceedings of the River Flow: September 08-10, Braunschweig, Germany: 137–44.

Thorne, C. et al. (1985) Direct Measurement of Secondary Currents in a Meandering Sand Bed River. Nature 315: 746 - 747

Thomson, J. (1876) On the Origin of Windings of Rivers in Alluvial Plains with Remarks on the Flow of Water Round Bends in Pipes. Proceedings of the Royal Society of London: 5-8.

Toombes, L. and Chanson, H. (2011) Numerical Limitations of Hydraulic Models. Proceedings of 10th Hydraulics Conference, 34th IAHR World Congress - Balance and Uncertainty, 33rd Hydrology and Water Resources Symposium, 26 June - 1 July, Brisbane, Australia.

Uddin, M. and Rahman, M. (2012) Flow and Erosion at a Bend in the Braided Jamuna River. International Journal of Sediment Research, 27(4): 498-509.

Vaghefi, M., Akbari, M. and Fiouz, A. (2015) Experimental Investigation of the Three-dimensional Flow Velocity Components in a 180-Degree Sharp Bend. World Applied Programming, 5(9): 125-131.

Vaghefi, M., Akbari, M. and Fiouz, A. (2014) Experimental Investigation on Bed Shear Stress Distribution in a 180-Degree Sharp Bend by using Depth- Averaged Method. International Journal of Scientific Engineering and Technology, 3(7): 962-965.

Versteeg, H. and Malalasekera, W. (2007) An Introduction to Computational Fluid Dynamics The Finite Volume Method. Pearson, UK.

Webber, N. and Greated, C.A. (1966) An Investigation of Flow Behaviour at the Junction of Rectangular Channels. Proc. Institute Civil Engineers, 34(3):321–334.

Weber, L., Schumate, E. and Mawer, N. (2001) Experiments on Flow at a 90-Degree Open-Channel Junction. Journal of Hydraulic Engineering, 127(5): 340-350.

Wim, V. (2010) Curved open-channel flow: A numerical Study. PhD thesis, Technical University of Delft, South Holland, Netherlands.

Wu, W., Rodi, W. and Wenka, T. (2000) 3D Numerical Modelling of Flow and Sediment Transport in Open Channels. Journal of Hydraulic Engineering, ASCE, 126(1): 4–15.

Yalin, M (1992) River Mechanics. Pergamon Press, London.

Yang, S. (2005) Interactions of Boundary Shear Stress, Secondary Currents and Velocity. Fluid Dynamics Research, 36(3): 121-136.

Yeh, K. and Kennedy, J. (1993) Moment Model of Nonuniform Channel-Bend Flow. I: Fixed beds. J Hydraul. Eng., 119(7): 776-795.

Zeng, J., Constantinescu, G. Blanckaert, K. and Weber, L. (2008) Flow and Bathymetry in Sharp Open-Channel Bends: Experiments and Predictions. Water Resources Research, 44(9): 1-22.

Zhu, D.J. (2011) Computational Simulations and Applications. InTech, Rijeka, Croatia.

Appendix A

Linear Eddy Viscosity Models (LEVMs)

- Standard ***k-ε*** Turbulence Model

In 1972, Launder and Spalding proposed this model, and it has been used commonly since that time. The transport equation of turbulent kinetic energy (k) for this model is derived from momentum equations, while the physical reasoning is used to obtain the transport equation for the turbulent energy dissipation (ε), taking in account that it should be similar to the mathematically derived transport equation of k (Gildeh, 2013). In this model, the following equations were used to obtain the turbulent kinetic energy and its rate of dissipation:

$$\frac{\partial k}{\partial t} + \frac{\partial k u_i}{\partial x_i} = \frac{\partial}{\partial x_i}\left(D k_{eff} \frac{\partial k}{\partial x_i}\right) + G_k - \varepsilon \tag{A1}$$

$$\frac{\partial \varepsilon}{\partial t} + \frac{\partial \varepsilon u_i}{\partial x_i} = \frac{\partial}{\partial x_i}\left(D \varepsilon_{eff} \frac{\partial \varepsilon}{\partial x_i}\right) + C_{1\varepsilon} \frac{\varepsilon}{k} G_k - C_{2\varepsilon} \frac{\varepsilon^2}{k} \tag{A2}$$

where Gk symbolized the generation of turbulent kinetic energy due to mean velocity gradients, $Dkeff$ and $D\varepsilon eff$ are the effective diffusivity for *k* and *ε*, respectively. They are calculated as shown below:

$$Dk_{eff} = v + v_t \tag{A3}$$

$$D\varepsilon_{eff} = v + \frac{v_t}{\sigma_\varepsilon} \tag{A4}$$

The equation of the turbulent kinematic viscosity at each point is:

$$v_t = C_\mu \frac{k^2}{\varepsilon} \tag{A5}$$

σ_ε is turbulent Prandtl number for ε, which has been determined according to the experiment and is assumed equal to 1.3.

Furthermore, the constants $C1\varepsilon$, $C2\varepsilon$ and $C\mu$ are also determined on the light of the experiment and they have been chosen to have the following values:

$C1\varepsilon = 1.44, C2\varepsilon = 1.92, C\mu = 0.09$

G_k is the production of turbulent kinetic energy which is common in most turbulence models and is defined as:

$$G_k = -u_i{}' u_j{}' \frac{\partial \mathrm{u}_j}{\partial \mathrm{x}_i} \tag{A6}$$

It also can be written as

$$G_k = 2v_t {S_{ij}}^2 \tag{A7}$$

$$S_{ij} = 0.5(\frac{\partial \mathrm{u}_j}{\partial \mathrm{x}_i} + \frac{\partial \mathrm{u}_i}{\partial \mathrm{x}_j}) \tag{A8}$$

where $u_i{}', u_j{}'$ and S_{ij} are the fluctuating parts of velocity and strain-rate tensor respectively.

- Realizable ***k-ε*** Turbulence Model

This model has been developed by Shih in 1995, and it is considered one of the most recently advanced turbulence models in $k-\varepsilon$ category (Gildeh, 2013). In this model, two major variances from the standard *k-ε* model have been displayed. These differences are represented in using (i) a new turbulent viscosity equation, and (ii) the transport of the mean-squared vorticity fluctuation equation was used to derive the dissipation rate transport equation. The eddy viscosity equations were based on the Realizability constraints, the positivity of normal Reynolds stresses, and Schwartz's inequality for turbulent shear stresses (Gildeh, 2013). Due to the unsatisfactory results of the standard *k-ε* model on this, the realizable *k-ε* model became more precise than other models in predicting flows such as discrete flows and flows with complicated secondary flow features.

The transport equations become as below:

$$\frac{\partial k}{\partial t} + \frac{\partial k u_i}{\partial x_i} = \frac{\partial}{\partial x_i}\left(D k_{eff} \frac{\partial k}{\partial x_i}\right) + G_k - \varepsilon \tag{A9}$$

$$\frac{\partial \varepsilon}{\partial t} + \frac{\partial \varepsilon u_i}{\partial x_i} = \frac{\partial}{\partial x_i}\left(D k_{eff} \frac{\partial \varepsilon}{\partial x_i}\right) + \sqrt{2} C_{1\varepsilon} S_{ij} \varepsilon - C_{2\varepsilon} \frac{\varepsilon^2}{k + \sqrt{\upsilon \varepsilon}} \tag{A10}$$

The equation of the turbulent viscosity is determined by

$$\upsilon_{\mathrm{t}} = C_{\mu}\frac{k^2}{\varepsilon} \tag{A11}$$

where, C_{μ} is computed by:

$$C_{\mu} = \frac{1}{A_0 + A_s\frac{kU^*}{\varepsilon}} \tag{A12}$$

$$U^* = \sqrt{S_{ij}S_{ij} + \tilde{\Omega}_{ij}\tilde{\Omega}_{ij}} \tag{A13}$$

$$\tilde{\Omega}_{ij} = \bar{\Omega}_{ij} - \varepsilon_{ijk}\omega_k - 2\varepsilon_{ijk}\omega_k \tag{A14}$$

where $\bar{\Omega}_{ij}$ the mean rate of rotation tensor, and ω_k is the angular velocity.

The constants A_0 and A_s are determined as below:

$$A_0=4,\ A_s = \sqrt{6}cos\varphi \tag{A15}$$

$$\varphi = \frac{1}{3}Arccos(\min(\max(\sqrt{6}W, -1), 1) \tag{A16}$$

$$W = \frac{S_{ij}S_{jk}S_{ki}}{\tilde{S}^2} \tag{A17}$$

The equation of $C_{1\varepsilon}$ is defined as below:

$$C_{1\varepsilon} = \max(\frac{\eta}{5+\eta}, 0.43) \tag{A18}$$

The constants C_2, σ_k and σ_{ε} were specified by Shih in 1995 and they are defined as below:

$C_2 = 1.9, \sigma_k = 1.0, and \sigma_{\varepsilon} = 1.2$

Reynolds Stress Models (RSMs)

- The Launder–Reece–Rodi model

This model was laid out by Launder, Reece and Rodi in 1975 (Zhu, 2011). It includes the proposal of two rapid pressure-strain rate models. Quasi-isotropic model (LRR-QI) is the first model. It includes the most common linear tensorial form that meet the required symmetry terms. The equation of the first model is shown below:

$$\emptyset_{ij}^{r} = -C_2\left(P_{ij} - \frac{2}{3}\delta_{ij}P_k\right) - C_3\left(D_{ij} - \frac{2}{3}\delta_{ij}P_k\right) - 2C_4 k S_{ij} \quad \text{(A19)}$$

where S_{ij} is the mean strain rate tensor, determined as:

$$S_{ij} = \frac{1}{2}\left(\frac{\partial U_i}{\partial x_j} + \frac{\partial U_j}{\partial x_i}\right) \quad \text{(A20)}$$

the values of the coefficients is shown below:

$$C_2 = 0.764, \qquad C_3 = 0.182, \qquad C_4 = 0.109$$

The isotropization of production (LRR-IP) is the second model. It is also considered as the 'Basic' model. In this model, the first term of QI model is kept, while the rest two terms are neglected. The equation is shown below:

$$\emptyset_{ij}^{r} = -C_2\left(P_{ij} - \frac{2}{3}\delta_{ij}P_k\right) \quad \text{(A21)}$$

the coefficient C2 in this equation set as 0.6. The model of Rotta return-to-isotropy has been used in both models for the term of slow pressure-strain rate,

$$\emptyset_{ij}^{s} = -C_1 \varepsilon a_{ij} \quad \text{(A22)}$$

the value of C1 coefficient is (1.5) in QI model, and (1.8) in the IP model. Many applications use the simpler GGDH in the original proposal turbulent diffusion. The models are written as below:

$$\frac{D\overline{u_\iota u_j}}{D_t} = P_{ij} - C_{1\varepsilon a_{ij}} + \emptyset_{ij}^{r} + \emptyset_{ij}^{s,w} + \emptyset_{ij}^{r,w} + \frac{\partial}{\partial x_l}\left(C_s \frac{\varepsilon}{k}\overline{u_l u_k}\frac{\partial \overline{u_\iota u_j}}{\partial x_k}\right) - \frac{2}{3}\delta_{ij}\varepsilon \quad \text{(A23)}$$

where $\emptyset_{ij}^{r}$ is changed on the light of the models, either the QI or IP model, $\emptyset_{ij}^{s,w}$, $\emptyset_{ij}^{r,w}$ are given in the equations below:

$$\emptyset_{ij}^{s,w} = C_1^w \frac{\varepsilon}{k}\left(\overline{u_k u_m} n_k n_m \delta_{ij} - \frac{3}{2}\overline{u_\iota u_k} n_k n_j - \frac{3}{2}\overline{u_j u_k} n_k n_i\right) f_w \quad \text{(A24)}$$

$$\emptyset_{ij}^{r,w} = C_2^w\left(\emptyset_{km}^{r} n_k n_m \delta_{ij} - \frac{3}{2}\emptyset_{ik}^{r} n_k n_j - \frac{3}{2}\emptyset_{jk}^{r} n_k n_i\right) f_w \quad \text{(A25)}$$

where $C_1^w = 0.5,\ C_2^w = 0.3, and\ f_w = 0.4k^{\frac{3}{2}}/(\varepsilon x_n)$ which is a damping function.

The term of an isotropic dissipation rate tensor was presumed instead of the viscous diffusion term which is neglected due to the high Re models intended by these models. At the end, the equation of the standard high-Re dissipation rate is shown below:

$$\frac{D_\varepsilon}{D_t} = C_{\varepsilon 1}\frac{\varepsilon}{k}P_k - C_{\varepsilon 2}\frac{\varepsilon^2}{k} + \frac{\partial}{\partial x_k}(C_\varepsilon \frac{k}{\varepsilon}\overline{u_k u_l}\frac{\partial x}{\partial x_l}) \quad \text{(A26)}$$

where

$$C_{\varepsilon 1} = 1.44, \qquad C_{\varepsilon 2} = 1.92, \qquad C_\varepsilon = 0.15$$

According to (Manceau, 2010; Davidson, 2011), the advantages of RSMs could be summarized as the following:

- The ability of RMS to respond effectively for any sudden change in the main strain.
- Modelling is not necessary required for the production terms, which are used to explain many phenomena.
- The transport equations, which contain the main physical mechanisms that derive the evolution of turbulence such as production, redistribution, turbulent transport, viscous diffusion, and dissipation, are solved without assuming any behaviour for Reynolds stresses.

However, implementing the RSMs is considered as a hard task due to their complexity and CPU consuming. In addition, the numerical analyses of RSMs are very sensitive because of the small stabilizing of the second order derivatives of the momentum equations.

- Large-Eddy Simulation Turbulence Model

Large Eddy Simulation (LES) is one of the turbulent models that used a different approach to simulate the turbulent flows. The idea of this model based on calculating the large eddies for each problem with a simulation depending on time(Horizonte, 2014).

The variable of flow during the decomposition could be described as the sum of:

- The function of filtered and the spatial variations ($\bar{u}$,$\bar{v}$, $\bar{w}$, $\bar{p}$ etc.). The LES computation can be used since spatial variation variables are bigger than the cutoff width, and

- The spatial variations (*u', v', w', p'* etc.). These cannot be solved when havinga length scale smaller than the filter cutoff width.

The equation in the general form is written as:

$$\emptyset(x,t) = \overline{\emptyset}(x,t) + \emptyset'(x,t) \quad \text{(A27)}$$

LES depend on using the spatial filtering operation that indicated by the overbar in order to separate between the large and small eddies, instead of time-averaging which uses in RANS turbulence models. The separation between the information of the large eddies (for resolving) and the small one (for rejecting and destroying) is done by the certain cutoff width, and that is considered as the initial procedures in addition to selecting the filtering function.
The equation of the filter function which is defined as $G(x,x',\Delta)$ is applied as shown below:

$$\overline{\emptyset}(x,t) = \int_{-\infty}^{\infty}\int_{-\infty}^{\infty}\int_{-\infty}^{\infty} G(x,x',\Delta)\emptyset(x',t)dx_1' dx_2' dx_3' \quad \text{(A28)}$$

where:
$\overline{\emptyset}(x,t)$= filtered function
$\emptyset(x,t)$= original (unfiltered) function
Δ = filter cutoff width
The main purpose of the cutoff width is to use it as an indicative measure of the large size eddies that are kept in the calculations and the small ones that are refused. The cutoff width is generally used to be from the same order as grid size, or $\Delta = \sqrt[3]{\Delta x.\Delta y.\Delta z}$

The LES continuity equation for incompressible flows is:

$$div(\overline{\boldsymbol{u}}) = 0 \text{(A7)}$$

The LES Navier-Stokes equations for an incompressible flow are:

$$\frac{\partial \bar{u}}{\partial t} + div(\bar{u}\overline{\boldsymbol{u}}) = -\frac{1}{\rho}\frac{\partial \bar{p}}{\partial x} + v\, div\big(grad(\bar{u})\big) - (div(\overline{u\boldsymbol{u}}) - div(\bar{u}\overline{\boldsymbol{u}}))$$

$$\frac{\partial \bar{v}}{\partial t} + div(\bar{v}\overline{\boldsymbol{u}}) = -\frac{1}{\rho}\frac{\partial \bar{p}}{\partial y} + v\, div\big(grad(\bar{v})\big) - (div(\overline{v\boldsymbol{u}}) - div(\bar{v}\,\overline{\boldsymbol{u}}))$$

$$\frac{\partial \overline{w}}{\partial t} + div(\overline{w}\overline{\boldsymbol{u}}) = -\frac{1}{\rho}\frac{\partial \overline{p}}{\partial z} + v\, div\big(grad(w)\big) - (div(\overline{w\boldsymbol{u}}) - div(\overline{w}\overline{\boldsymbol{u}}))$$

(I) (II) (III) (IV) (V) (A29)

These five terms of the equation have been named by Versteeg and Malalasekera (2007) (I) the rate of change of filtered x-, y- and z-momentum; (II) and (IV) the convective and diffusive fluxes of filtered x-, y- and z-momentum; (III) the gradients in the x-, y- and z-directions of the filtered pressure field; and (V) the extra terms caused by the filtering operation. The last term of the equation is (V) which could be considered as a divergence of a set of stressesτ_{ij}, and written as below:

$$(div(\rho\overline{u_\iota \boldsymbol{u}} - \rho\overline{u}_\iota\overline{\boldsymbol{u}}) = \frac{\partial(\rho\overline{u_\iota u} - \rho\overline{u}_\iota\overline{u})}{\partial x} + \frac{\partial(\rho\overline{u_\iota v} - \rho\overline{u}_\iota\overline{v})}{\partial y} + \frac{\partial(\rho\overline{u_\iota w} - \rho\overline{u}_\iota\overline{w})}{\partial z} = \frac{\partial \tau_{ij}}{\partial x_j} \quad \text{(A30)}$$

where:

$$\partial\tau_{ij} = \rho\overline{u_\iota \boldsymbol{u}} - \rho\overline{u}_\iota\overline{\boldsymbol{u}} = \rho\overline{u_\iota u} - \rho\overline{u}_\iota\overline{u} \quad \text{(A31)}$$

In general, these stresses named as the LES Sub-Grid-Scale (SGS) stresses. Applying the equation (3.79) into the equation (3.84), the SGS stresses equation is:

$$\tau_{ij} = \big(\rho\overline{\overline{u}_\iota\overline{u}_j} - \rho\overline{u}_\iota\overline{u}_j\big) + (\rho\overline{\overline{u}_\iota u'_j} - \rho u'_\iota\overline{u}_j) + \rho\overline{u'_\iota u'_j} \quad \text{(A32)}$$

(I) (II) (III)

There are three terms in the SGS stresses equation:

- Leonard stresses (I): This part exists due to the impacts on the resolved scale.
- The cross-stresses (II): the interactions between the SGS eddies and the resolved flow generates this part, and
- The LES Reynolds stresses (III): This part is caused by convective momentum transfer due to interactions of SGS eddies.

Comparing with the two equation turbulence models, LES is considered more expensive, especially with needed to solve unsteady equations. However, when comparing the cost with

the accuracy of LES model, its efficiency, and other features with regard to time the cost might be reasonable and worthy.

This type of turbulence model is considered as more problem dependent since it uses large eddies that are dictated by the geometries and boundary conditions of the flow involved. That is, it is more universal since it overcomes the issues associated with using small eddies, such as tending to be more isotropic and less dependent on geometry. However, it is more computationally expensive since it needs for finer grid densities for LES models than the RANS models. Although the large CPU costs for high-Re flows can be reduced by using a coarse near wall mesh coupled with wall functions, the discretization schemes should be carefully designed, since higher order of models should be used, in order to obtain results of higher level of accuracy (Cable, 2009).

- Wall Functions

In order to solve the sharp gradients prevailing in the wall boundaries, the best way is to get a sufficiently fine grid. The computing of complex three-dimensional flow usually requires a lot of computer resources. Instead of that, it could be assumed that the wall behaves like a fully developed turbulent boundary layer and prescribe boundary conditions employing wall functions. It is mostly not true at all that the presumption of the flow near the wall has the characteristics of the one in a boundary layer. However, it is preferable to use the wall functions that allow us to use fine grid in other regions where the gradients of the flow variables are large, especially in the case of a maximum number of nodes that can be afford to use in a computation.

In a fully turbulent boundary layer the production term and the dissipation term in the log-law region ($30 < y+ < 100$)are much larger than the other terms. Using the log-law, the term can be written as:

$$\frac{U}{u_*} = \frac{1}{k} ln\left(\frac{E u_* y}{v}\right) \quad , E = 9.0 \tag{A33}$$

In the log-layer we can write the modelled $k$equation as:

$$0 = \mu_t \left(\frac{\partial \bar{U}}{\partial y} \right)^2 - \rho\epsilon \tag{A34}$$

When using wall functions, k and ε are not solved at the nodes adjacent to the walls. Instead they are fixed according to the theory presented above. The turbulent kinetic energy is set as:

$$kp = c_\mu^{-1/2} u_*^2 \tag{A35}$$

The shear stress at the wall can be expressed as:

$$\tau_\omega = \mu_{t,P} \frac{\partial U}{\partial \eta} \approx \mu_{t,P} \frac{U_{\parallel.P}}{\eta} \tag{A36}$$

where $U_{\parallel.P}$= velocity parallel to the wall, and η = normal distance to the wall. Using the definition of the friction velocity u_*.

$$\tau_\omega = \rho u_*^2 \tag{A37}$$

We obtain:

$$\mu_{t,P} \frac{U_{\parallel.P}}{\eta} = \rho u_*^2 \rightarrow \mu_{t,P} = \frac{u_*}{U_{\parallel.P}} \rho u_* \eta \tag{A38}$$

Substituting $\frac{u_*}{U_{\parallel.P}}$ with the log-law finally can be written:

$$\mu_{t,P} = \frac{\rho u_* \eta k}{ln(E\eta^+)} \tag{A39}$$

where

$$\eta^+ = \frac{u_{*\eta}}{v}$$